VOL.107 NO.GT9. SEPT. 1981

JOURNAL OF THE GEOTECHNICAL ENGINEERING DIVISION

PROCEEDINGS OF
THE AMERICAN SOCIETY
OF CIVIL ENGINEERS

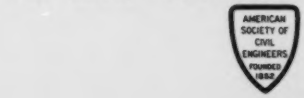

VOL.107 NO.GT9. SEPT. 1981

JOURNAL OF THE GEOTECHNICAL ENGINEERING DIVISION

PROCEEDINGS OF
THE AMERICAN SOCIETY
OF CIVIL ENGINEERS

Copyright© 1981 by
American Society
of Civil Engineers
All Rights Reserved
ISSN 0093-6405

William F. Marcuson III, Editor
U.S. Army Engineers

AMERICAN SOCIETY OF CIVIL ENGINEERS

BOARD OF DIRECTION

President
Irvan F. Mendenhall

Past President
Joseph S. Ward

President Elect
James R. Sims

Vice Presidents
Robert D. Bay
Francis J. Connell
Lyman R. Gillis
Albert A. Grant

Directors
Martin G. Abegg
Floyd A. Bishop
L. Gary Byrd
Larry J. Feeser
John A. Focht, Jr.
Sergio Gonzalez-Karg
James E. Humphrey, Jr.
Richard W. Karn
Leon D. Luck
Arthur R. McDaniel
Paul R. Munger
William R. Neuman
Leonard S. Oberman
John D. Parkhurst
Celestino R. Pennoni
Robert B. Rhode
S. Russell Stearns
William H. Taylor
Stafford E. Thornton
Robert E. Whiteside
Richard S. Woodruff

EXECUTIVE OFFICERS

Eugene Zwoyer, *Executive Director*
Julie E. Gibouleau, *Assistant to the Executive Director*
Louis L. Meier, *Washington Counsel/Assistant Secretary*
William H. Wisely, *Executive Director Emeritus*
Michael N. Salgo, *Treasurer*
Elmer B. Isaak, *Assistant Treasurer*

STAFF DIRECTORS

Donald A. Buzzell, *Managing Director for Education and Professional Affairs*
Robert A. Crist, Jr., *Managing Director for Publications and Technical Affairs*
Alexandra Bellow, *Director, Human Resources*
David Dresia, *Director, Publications Production and Marketing*
Barker D. Herr, *Director, Membership*
Richard A. Jeffers, *Controller*
Carl E. Nelson, *Director, Field Services*
Don P. Reynolds, *Director, Policy, Planning and Public Affairs*
Bruce Rickerson, *Director, Legislative Services*
Albert W. Turchick, *Director, Technical Services*
George K. Wadlin, *Director, Education Services*
R. Lawrence Whipple, *Director, Engineering Management Services*

COMMITTEE ON PUBLICATIONS

Stafford E. Thornton, *Chairman*
Martin G. Abegg
John A. Focht, Jr.
Richard W. Karn
Paul R. Munger
William R. Neuman

GEOTECHNICAL ENGINEERING DIVISION

Executive Committee
Robert Schuster, *Chairman*
Ernest T. Selig, *Vice Chairman*
William F. Swiger
Robert T. Darragh, Jr., *Secretary*
Roy E. Olson, *Management Group E Contact Member*
Harvey E. Wahls

Publications Committee
William F. Marcuson III, ***Chairman and Editor***
O. B. Andersland
John E. Anderson
Warren J. Baker
Don C. Banks
James M. Bell
Chandra S. Brahama
John T. Christian
G. W. Clough
Tuncer B. Edil
Herbert H. Einstein
Arley G. Franklin
D. H. Gray
Bobby Hardin
Cornelius J. Higgins
William H. Highter
Robert D. Holtz
Izzat M. Idriss
L. H. Irwin
Jey K. Jeyapalan
Reuben H. Karol
H. Y. Ko
William D. Kovacs
Leland M. Kraft
E. T. Selig, *Exec. Comm. Contact Member*
Raymond J. Krizek
Fred H. Kulhawy
C. C. Ladd
Poul V. Lade
Leonard J. Langfelder
Felipe A. Len-Rios
Gholamreza Mesri
Donald J. Murphy
S. V. Nathan
Thom L. Neff
Edward A. Nowatzki
Michael W. O'Neill
Jean H. Prevost
Adel Saada
Surendra K. Saxena
Robert L. Schiffman
Woodland G. Schockley
Marshall L. Silver
G. R. Thiers
D. D. Treadwell
Charles R. Ullrich
J. Lawrence Von Thun
R. N. Yong

PUBLICATION SERVICES DEPARTMENT

David Dresia, *Director, Publications Production and Marketing*

Technical and Professional Publications

Richard R. Torrens, *Manager*
Chuck Wahrhaftig, *Chief Copy Editor*
Corinne Bernstein, *Copy Editor*
Linda Ellington, *Copy Editor*
Walter Friedman, *Copy Editor*
Shiela Menaker, *Production Co-ordinator*
Richard C. Scheblein, *Draftsman*

Information Services

Elan Garonzik, *Editor*

PERMISSION TO PHOTOCOPY JOURNAL PAPERS

Permission to photocopy for personal or internal reference beyond the limits in Sections 107 and 108 of the U.S. Copyright Law is granted by the American Society of Civil Engineers for libraries and other users registered with the Copyright Clearance Center, 21 Congress Street, Salem, Mass. 01970, provided the appropriate fee is paid to the CCC for all articles bearing the CCC code. Requests for special permission or bulk copying should be addressed to the Manager of Technical and Professional Publications, American Society of Civil Engineers.

CONTENTS

Ground Movements Caused by Braced Excavations
by Thomas D. O'Rourke 1159

Laterally Loaded Pile Design
by Robert L. Sogge 1179

Nonlinear Seismic Response of Soft Clay Sites
by Ram D. Singh, Ricardo Dobry, Earl H. Doyle, and Izzat M. Idriss 1201

Anisotropic Strength of Cohesionless Sands
by Masanobu Oda 1219

Geotextile-Reinforced Unpaved Road Design
by Jean-Pierre Giroud and Laure Noiray 1233

The Journal of the Geotechnical Engineering Division (ISSN 0093-6405) is published monthly by the American Society of Civil Engineers. Publications office is at 345 East 47th Street, New York, N.Y. 10017. Address all ASCE correspondence to the Editorial and General Offices at 345 East 47th Street, New York, N.Y. 10017. Allow six weeks for change of address to become effective. Subscription price to members is $16.00. Nonmember subscriptions available; prices obtainable on request. Second-class postage paid at New York, N.Y. and at additional mailing offices. GT.

POSTMASTER: Send address changes to American Society of Civil Engineers, 345 East 47th Street, New York, NY 10017.

The Society is not responsible for any statement made or opinion expressed in its publications.

16511 GROUND MOVEMENTS CAUSED BY BRACED EXCAVATIONS

KEY WORDS: **Construction procedure;** Deformation; **Excavation; Foundations;** Lateral pressure; **Loads (forces);** Performance evaluation; Settlement control; **Soil-structure interaction**

ABSTRACT: The causes and patterns of ground movement associated with braced excavations are examined. Field measurements of displacements for braced cuts in sand and soft to medium clay show a relationship between the deflection of the excavation wall and the ratio of horizontal to vertical movement adjoining the cut. A review of various case histories indicates that soil displacement depends strongly on the construction process. Practices are recommended for promoting a stiff bracing system, excavating beneath the lowest braces, and using berms to restrain ground movement.

REFERENCE: O'Rourke, Thomas D. (Asst. Prof., School of Civ. and Environmental Engrg., Cornell Univ., Ithaca, N.Y. 14853), "Ground Movements Caused by Braced Excavations," *Journal of the Geotechnical Engineering Division,* ASCE, Vol. 107, No. GT9, **Proc. Paper 16511**, September, 1981, pp. 1159-1178

16510 LATERALLY LOADED PILE DESIGN

KEY WORDS: Analysis (mathematics); Coefficient of subgrade reaction; **Computer analysis; Computers; Earth pressure; Foundations;** Lateral forces; **Piles;** Piles (foundations); **Soil mechanics;** Soil-structure interaction

ABSTRACT: A beam-bar finite element formulation of a laterally loaded pile problem is developed. The approach taken utilizes the beam on elastic foundation coefficient of subgrade reaction method. The three loading conditions of a lateral load or applied moment on a free-end pile and a lateral load applied to a fixed-end pile are analyzed for a range of soil strength variations with depth. Curves are developed which present the maximum values as a function of the soil-structure stiffness ratio. A design procedure with an example is given to show the use of these curves in the design of any laterally loaded pile system.

REFERENCE: Sogge, Robert L. (Principal Consulting Geotechnical Engr., Desert Earth Engrg., Tuscon, Ariz. 85705), "Laterally Loaded Pile Design," *Journal of the Geotechnical Engineering Division,* ASCE, Vol. 107, No. GT9, **Proc. Paper 16510**, September, 1981, pp. 1179-1199

16493 SEISMIC RESPONSE OF SOFT CLAY SITES

KEY WORDS: Amplification; Clays; **Computer programs;** Cyclic loads; Damping; Degradation; Earthquakes; Mathematical models; San Francisco; **Seismic stability;** Shear modulus; **Site evaluation; Soft soils; Vibration response**

ABSTRACT: A nonlinear stress-strain model, utilizing Ramberg-Osgood idealization of backbone curve and allowing for its progressive degradation due to cyclic loading, is used to conduct site response studies at two soft clay sites. The sites selected are: (1) Southern Pacific Building, San Francisco, and (2) Station No. 119 Site, Tokyo, Japan. The subsurface conditions and the material properties used in analyses are presented. The computer program DCHARM used for nonlinear analysis allows for progressive degradation of the backbone curve. For comparison the results obtained from program SHAKE using equivalent linear idealization are also presented. The program DCHARM is shown to provide ground response results closer to the recorded data than SHAKE. The results obtained indicate that substantially higher accelerations and durations of earthquakes are needed to cause significant degradation of soft clay.

REFERENCE: Singh, Ram D. (Sr. Project Engr., Woodward-Clyde Consultants, 5120 Butler Pike, Plymouth Meeting, Pa. 19462), Debry, Ricardo, Doyle, Earl H., and Idriss, Izzat M., "Nonlinear Seismic Response of Soft Clay Sites," *Journal of the Geotechnical Engineering Division,* ASCE, Vol. 107, No. GT9, **Proc. Paper 16493**, September, 1981, pp. 1201-1218

16491 ANISOTROPIC STRENGTH OF COHESIONLESS SANDS

KEY WORDS: **Anisotropic soils; Anisotropy; Cohesionless soils; Fabrics;** Granular materials; **Sands;** Sandy soils; Shear strength; Soil mechanics; Soil strength

ABSTRACT: Natural soil deposits are generally anisotropic as well as heterogeneous. In order to provide a guideline for estimating a reasonable strength parameter applicable to such complex soils, plane strain tests on uniform-anisotropic, uniform-pseudoisotropic, layered-anisotropic, and layered-pseudoisotropic samples have been performed. Anisotropic strength response, caused by the anisotropic distribution of contact normals, should be expected even in a uniform mass of spheres. It is always necessary to assume that sand is generally anisotropic. Tests on samples prepared by the plunging-tapping method are advisable for obtaining a reasonable estimate of the mean strength for anisotropic sands.

REFERENCE: Oda, Masanobu (Visiting Scholar, Dept. of Civ. Engrg., Northwestern Univ., Evanston, Ill.; (Per, Address) Dept. of Foundation Engrg., Saitama Univ., Japan), "Anisotropic Strength of Cohesionless Sands," *Journal of the Geotechnical Engineering Division,* ASCE, Vol. 107, No. GT9, **Proc. Paper 16491**, September, 1981, pp. 1219-1231

16489 GEOTEXTILE-REINFORCED UNPAVED ROAD DESIGN

KEY WORDS: Aggregates; **Fabrics; Geotextiles; Reinforced roads;** Reinforcement; **Road design;** Soil stability; Surface treatment (roads); **Textiles; Unpaved roads**

ABSTRACT: By providing reinforcement, geotextiles improve the performance of unpaved roads, and for a given traffic, the thickness of the aggregate layer can be reduced. This paper explores the mechanism of geotextile reinforcement of roadways, and a method is developed which enables the engineer to calculate the required thickness of aggregate layer and make a proper selection of the geotextile to be used. Charts are presented to assist in the design of geotextile-reinforced unpaved roads and to evaluate the reduction of aggregate thickness resulting from the use of a geotextile. Practical examples and comparisons with full scale tests are presented.

REFERENCE: Giroud, Jean-Pierre(eWoodward-Clyde Consultants, Geotextiles and Geomembranes Group, Chicago, Ill. 60603), and Noiray, Laure, "Geotextile-Reinforced Unpaved Road Design," *Journal of the Geotechnical Engineering Division,* ASCE, Vol. 107, No. GT9, **Proc. Paper 16489**, September, 1981, pp. 1233-1254

GROUND MOVEMENTS CAUSED BY BRACED EXCAVATIONS

By Thomas D. O'Rourke,[1] A. M. ASCE

INTRODUCTION

The design of braced excavations is performed on the basis of two fundamental requirements: (1) The selection of excavation and support measures necessary for stability of the cut; and (2) the control of ground movements affecting adjacent property. Stability generally means preventing failure, i.e., designing the braced cut to remain open without danger to construction personnel or very large movements that jeopardize surrounding structures. Design measures for stability include the selection of earth pressures, determining of the potential for base soil failure, and the layout of a dewatering system to prevent piping and blowout along the walls and bottom of the cut. The control of ground movements generally is based on the types of buildings and public facilities near the excavation. Foremost among the measures necessary for control is the prediction of displacements at various distances from the cut. In addition, control measures include the protection of adjacent structures and the use of construction methods to restrict ground movements to levels consistent with the acceptable performance of surrounding facilities.

With regard to stability, apparent earth pressure envelopes are recommended for a variety of soil types (16,19,20) and methods are available for estimating the likelihood of plastic deformation and base failure for excavations in clay (5,16). In contrast, the patterns of settlement associated with braced cuts are summarized only in very general terms, and horizontal displacements are treated mostly on a case history basis. The wide range of performance resulting from different soil conditions and construction methods often complicates the decision-making process regarding both the potential for damage and protection of nearby structures.

This paper examines the ground movements caused by braced excavations with emphasis on the relationship between ground movements and various aspects of the construction process. Sources of lost ground are reviewed and deformation patterns at the excavation wall are related to displacement patterns at the ground

[1]Asst. Prof., School of Civ. and Environmental Engrg., Cornell Univ., Ithaca, N.Y. 14853.

Note.—Discussion open until February 1, 1982. To extend the closing date one month, a written request must be filed with the Manager of Technical and Professional Publications, ASCE. Manuscript was submitted for review for possible publication on October 31, 1980. This paper is part of the Journal of the Geotechnical Engineering Division, Proceedings of the American Society of Civil Engineers, ©ASCE, Vol. 107, No. GT9, September, 1981. ISSN 0093-6405/81/0009-1159/$01.00.

surface adjoining the excavation. Case histories of braced cuts in both sands and soft clays are summarized and recommendations for ground movement control are made on the basis of observational data.

Site Preparation

Braced cuts commonly are visualized as a step-wise process of excavation and support. Following each increment of excavation, inward deflections of

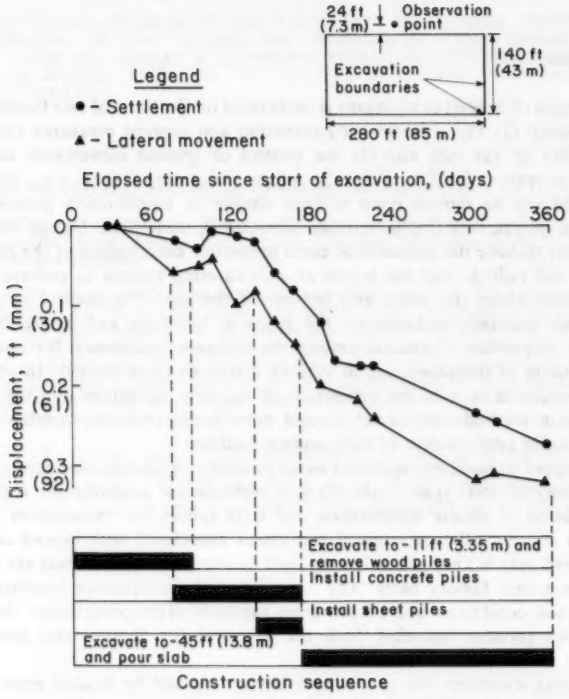

FIG. 1.—Ground Displacement Record for 45 ft (14 m) Deep Cut in Soft to Medium Clay

the walls occur. These deflections cause movements of the soil adjoining the cut that are transmitted to the ground surface as settlements and horizontal offsets. This process forms the conceptual basis for much of the analysis and finite element modeling of braced cut performance and has been helpful for understanding the ground response to actual excavation and bracing procedures. Nevertheless, deep excavations often are performed in combination with other activities that cause movement particularly during the preparatory stages of construction.

Site preparation may include: (1) Relocation and underpinning of utilities; (2) dewatering of aquifers above and below the base of excavation; (3) construction of the excavation wall; and (4) the installation of deep foundations. In some cases, the movements associated with site preparation will exceed those occurring as a result of the excavation and support process. The relocation of utilities, e.g., may have a locally severe impact of adjacent property, especially when trenching is carried close to other pipelines and communication conduits. Alternatively, dewatering may consolidate the soil over an area that exceeds substantially the area affected by excavation-induced movements. Wall construction may require predrilling for soldier piles, the use of vibratory hammers to install sheet piles, or the excavation of slurry panels for concrete diaphragm walls. Each of these can cause permanent movements, the magnitude and distribution of which will vary according to the soil conditions and details of the construction procedures.

Ground movements associated with site preparation are shown in the records of deep basement construction. As an example, Fig. 1 relates typical settlement and horizontal movements with the various construction activities performed for a 45 ft (14 m) deep braced cut at the Embarcadero III Project in San Francisco. The cut was excavated through approximately 22 ft (6.5 m) of granular fill and sands and 23 ft (7 m) of soft to medium silts and clays. The bottom of the cut was underlain by roughly 35 ft (11 m) of medium clay followed by a deposit of interbedded dense sand and stiff clay. The general construction procedure at this site is described by Drossel (7). The soil conditions and temporary bracing system were similar to those associated with braced cut construction at the Levi Strauss Building, which is considered by Tait and Taylor (18).

The ground movements were strongly influenced by construction activities related to site preparation for deep excavation and pile driving. Over 800 timber piles were removed from the site and a similar number of prestressed concrete piles were driven. Sheet piles were installed along the perimeter of the cut with a vibratory hammer. Between Day 90 and Day 170, approximately 30% of the total ground movements occurred even though the excavation was maintained at a constant 11 ft (3.4 m) depth. In some cases, there was a clear relationship between movement and construction activity, e.g., when timber piles were removed near the property line, horizontal movements were induced that cracked the street surface for a distance of 15 ft–25 ft (4.5 m–7.6 m) from the excavation's edge.

In a similar manner, the construction of drilled shafts in Chicago has led to large settlements. Fig. 2 summarizes the settlements adjacent to three braced cuts where large movements were caused, principally as the result of ground loss during drilled shaft, or caisson, construction. The cases are selected to show extreme conditions of ground loss and are not necessarily typical of general construction practices. The settlements and distances are plotted in dimensionless form as fractions of the maximum excavation depth. Zones of settlement, delineated by Peck (18) for various soil types and excavation conditions, are shown for comparison.

Chicago practice for drilled shaft construction has been considered in detail by Baker and Khan (1) and ground movements associated with the construction method have been described by Lukas and Baker (10). Therefore, only a brief description is given here. In general, oversized shafts were drilled to depths

ranging from 20 ft–35 ft (6 m–10.5 m) below the construction surface. After temporary steel linings were set, the shafts were further extended by augering and advancing a steel casing, which was left in place as part of the permanent foundation. All drilled shafts were carried to the limestone bedrock, approximately 110 ft (34 m) below street level.

Much of the settlement associated with case 1 resulted from dewatering difficulties in a deposit of sand, silt, and gravel directly overlying bedrock. Pumping was required to prepare the drilled shaft bottoms for concrete and, in the process, sand and silt were pumped out with the water. Large portions of the settlements for Case 2 and Case 3 were caused by clay squeezing into

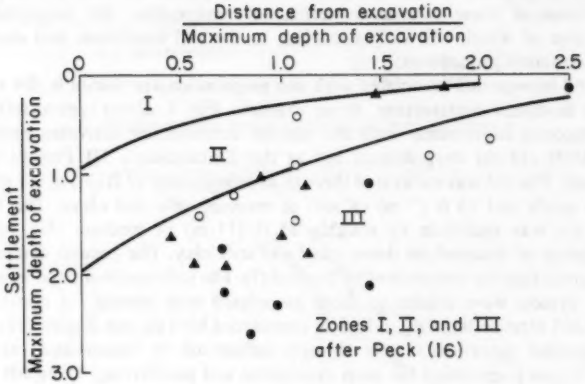

Case	Symbol	Max. depth ft (m)	Support	Special problems
1	▲	45 (14)	Slurry wall; 3 levels of rakers	Pumped fines from base of caissons
2	●	28 (8.5)	Soldier piles & lagging; 1 level of rakers	Soil squeeze during caisson construction
3	○	26 (8)	Slurry wall; 1 level of struts	Soil squeeze during caisson construction

FIG. 2.—Settlements Adjacent to Braced Cuts with Caisson Construction Difficulties

the shafts during excavation and into annular voids around the shafts after steel linings had been installed. In all cases, the movements associated with drilled shaft construction were between 50% and 70% of the total settlements shown in Fig. 2.

General Patterns of Ground Movement

Braced excavations generally are performed in three prominent stages. During each stage, excavation and support methods contribute to the ground displacement

in a characteristic way. These stages include: (1) Initial excavation before bracing; (2) excavation to subgrade after the upper braces are installed; and (3) removal of the braces.

Fig. 3 traces the development of lateral soil movement as a function of the construction history for a cut-and-cover excavation in Washington, D.C. The excavation was 60 ft (18 m) deep and was supported by soldier pile and lagging walls with five levels of cross-lot struts. The soldier piles (W 24 × 130) were 75 ft (23 m) long and were located on 7.5 ft (2.3 m) centers. Field observations of this excavation and details of the instrumentation have been reported by the writer (12).

The figure shows the horizontal wall movements and cumulative horizontal strains in the soil for each of the construction stages. The horizontal strains

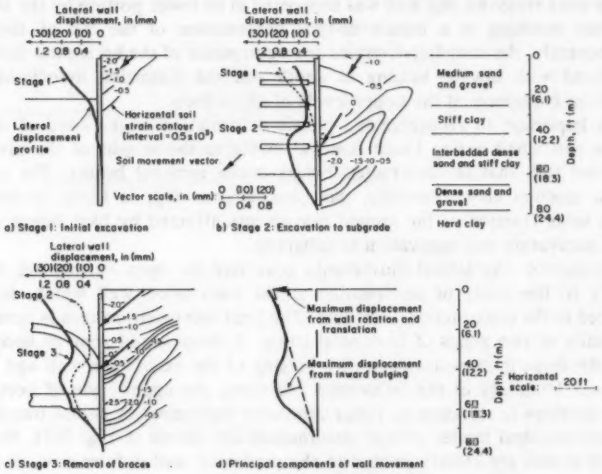

FIG. 3.—Horizontal Strains Associated with Various Stages of Braced Cut Construction

have been estimated from inclinometer measurements by dividing the differential lateral displacement between two points at a given elevation by the distance separating them and plotting the strain at the midpoint between the two measurements. In addition, vectors of cumulative ground movement are shown at various locations. Each vector was determined from the vertical and horizontal movement at a common point. The horizontal movements were measured with inclinometers, and the vertical movements were measured either by optical leveling at the street surface or vertical extensometers at depth. The contour interval for horizontal strain is 0.5×10^{-3}, which is equivalent to the tensile strain at which cracking is induced in masonry structures (2). Strain magnitudes prefixed with a minus sign indicate tension. The construction sequence and lateral movements are described under the following headings.

Initial Excavation before Bracing.—The excavation was deepened 20 ft–25 ft (6 m–7.5 m) before braces were installed. Thus, deformation of the wall occurred primarily as a cantilever-type movement. The horizontal strains reflect this mode of deformation in a triangular pattern of contours that decrease in magnitude with depth and distance from the wall.

Excavation to Subgrade after Upper Braces Installed.—As braces were installed, the upper portion of the wall was restrained from further lateral movement. In fact, preloading the upper level struts decreased the horizontal movement at the top of the cut, resulting in a slight recompression of the soil. In the deeper portion of the cut, inward bulging of the wall caused tensile strains, the contours for which were inclined at approximately 45° from the vertical.

Removal of Braces.—As the bottom braces were removed to build the underground structure, further inward bulging of the wall occurred. When the upper braces were removed, the wall was supported in its lower portion by the subway structure resulting in a cantilever-type deformation of the top of the wall. Consequently, the cumulative strains are a composite of the horizontal distortion associated with inward bulging at depth and the distortion associated with cantilever movement at the upper levels of excavation.

It is important to recognize the plastic deformation at the base of the cut will be restrained during brace removal owing to the weight of the invert or basement slab that is constructed before brace removal begins. For cuts in soft to medium clay, therefore, this construction stage is likely to result in only a small fraction of the ground movements affected by base heave during initial excavation and excavation to subgrade.

In summary, the lateral movements generated by open cutting are related directly to the mode of deformation at the excavation wall which, in turn, is related to the construction procedure. The final movement pattern is composed essentially of two zones of horizontal strain. A deep-seated zone of horizontal strain develops in response to inward bulging of the excavation wall and forms the lower boundary of the influenced soil mass. An upper zone of horizontal strain develops in response to either cantilever movement or lateral translation. The two principal modes of wall deformation are shown in Fig. 3(*d*). Because the soil strains are closely related to the modes of wall deformation, it would be useful to develop a quantitative relationship between the displacement pattern at the wall and movement of the ground surface adjacent to the cut. This relationship is explored in the following section.

Wall Deformation and Ground Surface Movement

The measured displacements associated with several braced cuts were studied by comparing the deformations of the excavation walls with the ratios of horizontal movement to settlement at the ground surfaces adjoining the cuts. Fig. 4 summarizes the observed movements for two braced cuts in Chicago that are typical of the trend shown by all the excavations studied. Inclinometer measurements of wall displacement and optical surveys of settlement and lateral movements were used to develop the comparisons. In all cases, the field data pertain to maximum displacements measured after the excavations had been taken to subgrade and a significant portion of the braces removed. The data relate to movements measured at distances of 0.35–1.0 times the maximum

excavation depths from the cuts. Within these distances, the ratios of horizontal movement to settlement were found to be relatively constant, showing little variation as a function of distance from the excavation.

All data were screened in accordance with two guidelines: (1) Each ratio of lateral to vertical displacement derives from the combined measurement of lateral movement and settlement at the same observation point; and (2) measurements equal to or less than 1/4 in. (6 mm) were neglected to minimize the influence of survey error on the computed ratio. Furthermore, the computed

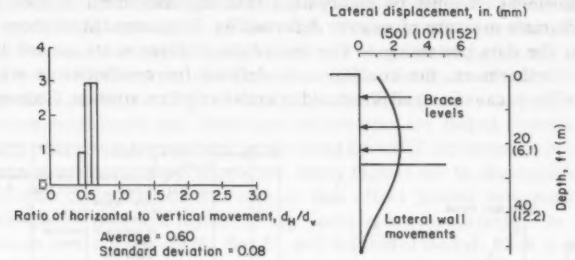

FIG. 4.—Ratios of Measured Horizontal Movements to Settlements at Ground Surface Adjoining Braced Cuts

ratios were analyzed statistically by assuming both normal and log normal distributions of the data. The assumed distributions gave similar values of the mean. The values in Fig. 4 are for normal distributions which gave slightly higher, more conservative ratios of horizontal to vertical movement.

There are marked differences in the ratios that depend on the pattern of wall movement. Fig. 4(*a*) shows the wall deflection for an excavation that was supported with stiff braces at an early stage of construction. The wall movement occurred principally as deep inward bulging. The average value of horizontal

to vertical movement adjoining the cut was 0.60. In contrast, Fig. 4(*b*) shows the wall deflection for an excavation where substantial cantilever movements occurred owing to a lack of early support and braces without adequate stiffness. The average value of horizontal to vertical movement adjoining the cut was 1.32.

To illustrate the influence of wall distortion on soil movements, a coefficient of the deformation, C_D, is defined in Fig. 5. The numerator of the expression is a measure of the cantilever movement, S_w, of the wall. The denominator represents the combined cantilever, S_w, and inward bulging, S'_w, components of displacement. It must be emphasized that the coefficient is used only as an approximate measure of relative deformation. It is intended to show general trends in the data pertaining to the immediate displacements caused by open cutting. Furthermore, the coefficient is defined for conditions in which the bottom of the excavation wall is secured in a relatively firm stratum. Consequently,

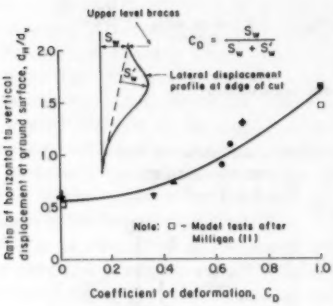

Case	Symbol	Max. depth ft (m)	Support	Soil	Location
1	●	60 (18)	Soldier piles & lagging, 5 strut levels	Sand and stiff clay	Washington, D.C.
2	▲	44 (13)	Soldier piles & lagging, 3 levels of struts and rakers	Soft to medium clay	Chicago, Ill.
3	▼	27 (8)	Sheet pile, 3 raker levels	Soft to medium clay	Chicago, Ill.
4	■	44 (13)	Slurry wall, 2 levels of tiebacks and rakers	Soft to medium clay	Chicago, Ill.
5	◆	30 (9)	Soldier piles & lagging, 2 raker levels	Soft to medium clay	Chicago, Ill.
6	●	26 (8)	Sheet pile 2 raker levels	Soft to medium clay	Chicago, Ill.
7	▲	45 (14)	Sheet pile, 3 levels of struts and rakers	Soft to medium clay	San Francisco, Calif.

FIG. 5.—Ratio of Horizontal to Vertical Ground Movement as Function of Coefficient of Deformation for Fixed-End Walls

the data summarized in Fig. 5 pertain to excavations where the walls were driven to a stiff soil layer, and thus, were not affected by significant movement of the wall bottoms.

Fig. 5 shows the ratio of horizontal displacement to settlement at the ground surface adjoining the cut as a function of the coefficient of deformation. Average values of the ratio are plotted. Field observations analyzed in terms of the coefficient were chosen for cases where there was little influence on movements from either site preparation or consolidation. The table in the figure summarizes information about the braced cuts. Data were derived from a total of seven braced cuts, ranging in depth from 25 ft–60 ft (8 m–18 m).

The field data show limits for the ratio of horizontal to vertical movement equal to approximately 0.6 and 1.6 for wall deformation caused solely by inward bulging and solely by cantilever movement, respectively. These bounds compare favorably with the limits determined from model tests, performed by Milligan (11), which also are plotted in Fig. 5. In the model tests, soil strains and

displacements in medium dense sand were measured in response to wall movements caused by incremental excavation. The combined field and model test data show that as cantilever-type movements are allowed to dominate during construction, the relative magnitude of horizontal ground movement increases significantly. Conversely, if the wall is firmly braced at an early stage of excavation, inward deflection of the wall will lead to horizontal movements that are significantly less than settlements.

The data summarized in Fig 5 can be used to estimate horizontal movements, either directly from settlement surveys or on a planning basis prior to construction. Most excavation and bracing schemes will generate both cantilever displacement and deep inward movement of the wall. Consequently, a value of one will provide a reasonable, preliminary estimate of the ratio of horizontal movement to settlement. Settlements can be estimated on the basis of local experience or from field measurements summarized in the literature.

Because settlements and horizontal movements are linked directly with the wall movement, it is important to understand how wall deformation is influenced by the excavation and support process. Many factors can be distinguished among the methods of excavation and support that affect ground movements. Three, in particular, deserve attention. They include brace stiffness, the depth of excavation beneath the lowest braces, and the use of berms. Each is considered in the following sections and examples are taken from field observations to show ground movement response to typical construction procedures.

Brace Stiffness

At the level of brace contact, wall movements are caused by compression at the interfaces among members of the support system, horizontal bending

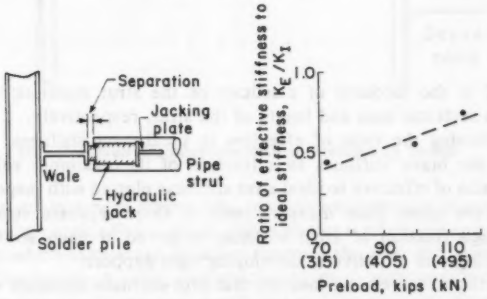

FIG. 6.—Preloading Set-Up and Measured Braced Stiffnesses

of the wale, and elastic deformation of the brace. Accordingly, the effective stiffness of the brace may be substantially less than its ideal elastic stiffness. Palmer and Kenney (15) report that the effective brace stiffness determined from field measurements during open cutting on the Oslo Subway was as low

as 1/50 of the idea elastic stiffness. Studies of braced cut behavior by Jaworski (9) and Scott (17) show that significant horizontal displacements occur when braces lack tight connections with the wall or compressible materials are used to shim separations between the support members.

Commonly, braces are preloaded to a percentage of their design load to induce rigid contacts among members of the support sytem. O'Rourke and Cording (13) have considered preloading practices during construction of the Washington, D.C. Metro. It is useful to examine these practices to emphasize some important characteristics of the preloading operation.

As shown in Fig. 6(*a*), preloading was performed by inserting a hydraulic jack on each side of an individual pipe strut between the wale and a special jacking plate welded to the strut. Hydraulic pressure was applied until the strut was stressed to approximately half its design load after which the separation between the strut and wale was shimmed with 1/8 in. (3 mm) thick steel plates.

Increased in separation between the struts and wales were measured during preloading. In addition, lateral displacements of the soldier piles at the level of preloading were measured on opposite sides of the excavation with inclinometers attached to the soldier piles. The soldier pile displacements were subtracted from the measured increases in separation to obtain the apparent deformation of each strut. The effective stiffness, K_E, of a strut in a given level of support is

$$K_E = \frac{P}{\Delta S} \quad \ldots\ldots\ldots\ldots\ldots\ldots\ldots\ldots\ldots\ldots\ldots\ldots\ldots\ldots\ldots\ldots\ldots\ldots\ldots\ldots\ldots\ldots (1)$$

in which P = the average preload; and ΔS = the average apparent deformation of each strut level.

The ideal elastic stiffness, K_I, of an individual strut is

$$K_I = \frac{EA}{L} \quad \ldots\ldots\ldots\ldots\ldots\ldots\ldots\ldots\ldots\ldots\ldots\ldots\ldots\ldots\ldots\ldots\ldots\ldots\ldots\ldots\ldots\ldots (2)$$

in which E = the modulus of elasticity of the strut material; and A and L = the cross-sectional area and length of the strut, respectively.

By determining the ratio of effective to ideal strut stiffness, it is possible to express the brace stiffness as a fraction of its maximum value. Fig. 6(*b*) shows the ratio of effective to ideal strut stiffness plotted with respect to preload. The data were taken from measurements at three separate strut levels. The relatively high fraction of ideal stiffness achieved at each strut level shows that preloading was effective in developing rigid support.

Although the measurements indicate that strut stiffness increases with increased load, very high preloads are not necessarily advantageous. In some instances, individual struts were preloaded higher than adjacent braces as a consequence of variations in the preloading technique. As the excavation continued, not only did the loads in these braces remain higher than those in adjacent members but, in some instances, increased at a faster rate. Very high preloads create locally stiff sections of the excavation wall that may attract relatively high pressures as additional excavation occurs.

Fig. 7 shows soldier pile displacements (shaded area) caused by preloading a level of cross-lot struts. The measurements are accurate to about 0.01 in.

(0.25 mm) at the level of preloading. The outward movement of the soldier piles shows that preloading was effective in closing separations within the bracing system. Movement at the level of the preloaded struts was a maximum 0.1 in. (2.5 mm) at each side of the excavation, and was distributed primarily within 10 ft (3 m) of the elevation of the jacking and wedging operation.

Under these conditions, preloads are not likely to regain previous soil movements because they have only a localized effect on wall displacement. As preloads are increased above the magnitude needed to develop a stiff bracing system, their contribution to the restraint of movement becomes increasingly less effective. Very high preloads may lead to strut loads that exceed design values and may cause high bending moments in the wall.

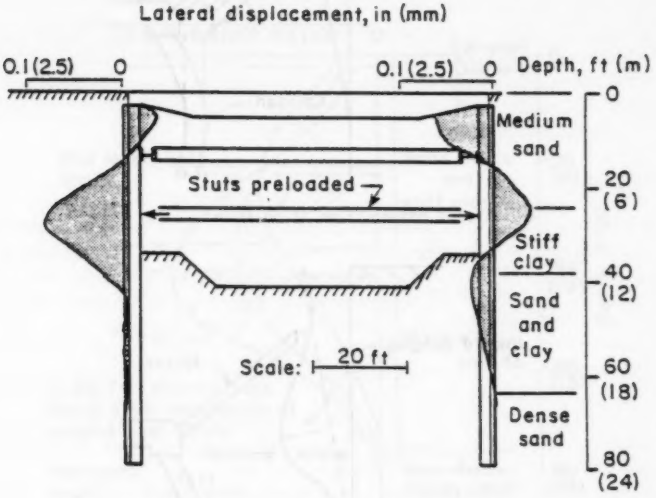

FIG. 7.—Wall Displacements from Preloading Struts

There are some instances where substantial movements can occur at the brace level even though preloading is used. Fig. 8 shows a relatively common bracing procedure in which rakers are installed between the wall and a portion of the completed foundation. A raker transmitting loads to only one or two caissons may lack the restraint to prevent significant wall movement. Elastic analyses, such as those outlined by Davisson and Gill (6), show that the lateral movements of a simple raker and caisson bracing system can be as high as 3 in. (76 mm) for braced cut loads typical of construction conditions in Chicago. Displacements of this nature lead to cantilever deformation of the wall.

Fig. 8(*a*) shows an idealized view of wall deformation associated with horizontal loading of a caisson. As grade beams are joined to several caissons and foundation slabs are poured, the restraint transmitted through the raker becomes increasingly more efficient. Fig. 8(*b*) shows additional wall movement after caisson deflections

have ceased and the excavation has been completed. Although the volumes of incremental displacement shown in Figs. 8(*a*) and 8(*b*) are approximately equal, the influence of wall movement on the pattern of soil displacement is substantially different. In Fig. 8(*a*) the cantilever deformation of the wall may

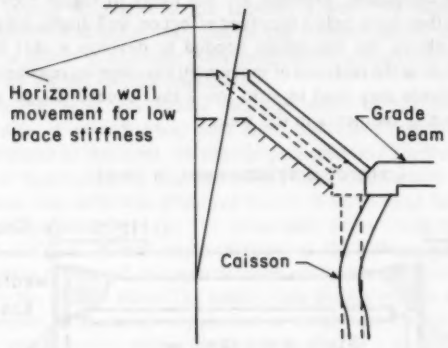

a) Lateral deformation of caisson

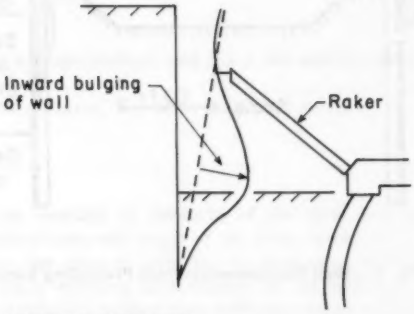

b) Caisson stabilized

FIG. 8.—Wall Deflections Associated with Raker and Caisson Bracing

induce horizontal ground movements that are nearly three times as large as those generated by the inward bulging shown in Fig. 8(*b*).

Excavation Depth Beneath Lowest Braces

Fig. 9 shows the lateral wall movements for a concrete diaphragm wall that was used during construction of part of the Washington, D.C. Metro. The 70 ft (21 m) wide excavation was extended through approximately 45 ft (14 m) of dense sands and stiff clay and 15 ft (4.5 m) of hard fissured clay. The

water table was located at approximately 35 ft (10.5 m) below the ground surface. The wall was 82 ft (25 m) deep and 33 in. (0.85 m) wide and was reinforced with steel piles (W 30 × 124) on 7 ft (2 m) centers. All braces were preloaded to approximately 75% of their design loads.

The figure shows lateral wall displacements corresponding to three successive levels of excavation beneath the second level struts. All movements and excavation depths are referenced to the time when the second level struts were installed and preloaded (Day 0). As is common for cut-and-cover construction, the excavation was carried to its deepest level at the center of the cut, leaving elevated sections of soil against the wall. As the central portion of the cut

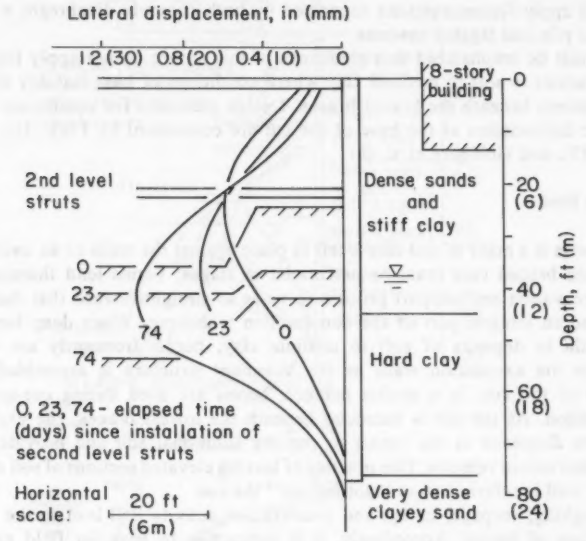

FIG. 9.—Observed Lateral Displacements of Concrete Diaphragm Wall

was deepened from 35 ft–55 ft (10.5 m–17 m), the inward movement increased by a maximum 0.7 in. (18 mm) and the volume of displacement nearly doubled.

The movements shown in Fig. 9 emphasize the importance of excavation depth beneath the lowest braces for controlling ground loss during open cutting. The section stiffness of the concrete diaphragm wall, which is the product of the wall's elastic modulus and moment of inertia, was approximately 10 times that of soldier pile and lagging walls used elsewhere during construction of the Washington, D.C. Metro. Nevertheless, the inward movements of the diaphragm wall are comparable to those reported for the other cuts (12,14). The deflections of excavation walls under distributed earth loads depends not only on the section stiffness, but on approximately the fourth power of the unsupported depth. Thus, an excavation carried 27 ft (8 m) as opposed to 15

ft (4.5 m) beneath the lowest braces will offset the benefit derived from a tenfold increase in wall section stiffness.

When concrete diaphragm walls are used as an alternative to underpinning adjacent structures and dewatering, they must support foundation and hydro-static pressures that exceed the earth pressures generally imposed on soldier pile and lagging systems. Under these conditions, it is unlikely that the deflection of a concrete diaphragm wall will be substantially less than that of a soldier pile and lagging wall subject only to earth pressure. For good control of ground movements, experience in Washington, D.C. suggests that excavation depths be limited to a maximum 18 ft (5.5 m) beneath the lowest braces for deep cuts in medium to dense sands and interbedded sands and stiff clay. This limit should apply for excavations supported by both concrete diaphragm walls and soldier pile and lagging systems.

It must be emphasized that guidelines of this nature do not apply for braced excavations in soft to medium clay where conditions of base stability influence movements beneath the lowest braces. Design measures for conditions of large plastic deformation at the base of the cut are considered by Peck (16), Clough et al. (5), and Goldberg et al. (8).

Use of Berms

A berm is a mass of soil that is left in place against the walls of an excavation. Because braced cuts must be performed in stages, berms lend themselves to the excavation and support process in ways to straightforward that they often become an integral part of the construction technique. When deep basements are built in deposits of soft to medium clay, berms frequently are used to restrain the excavation walls as the basement structure is assembled at the center of the cut. In a similar manner, berms are used during cut-and-cover excavation. As the cut is extended beneath the lowest braces, the excavation may be deepened at the center to remove additional soil and provide a path for construction vehicles. This practice of leaving elevated sections of soil adjacent to the wall is referred to as "slotting out" the cut.

Sloughing, seepage, creep, and construction activity will lead to the gradual distortion of berms. Accordingly, it is instructive to look for field examples that show how progressive deformations of berms have affected braced cut performance.

Fig. 10 shows the inward wall movements for an 82 ft (25 m) deep braced excavation in sands and interbedded stiff clay. The braced cut was part of the construction of Gallery Place Station on the Washington, D.C. Metro. Details of the construction and field instrumentation are described elsewhere (12). The excavation walls were composed of 90 ft (27.5 m) long soldier piles (W 24 × 130) on 7.5 ft (2.3 m) centers with timber lagging. The struts were prestressed to half their design loads. Wall displacements and levels of excavation are referenced to the time at which the fourth level struts were installed and preloaded (Day 0).

The displacements show the progressive wall movement as soil was excavated from a depth of 58 ft–82 ft (18 m–25 m). The total incremental volume of movement per unit length is given by the area between the lateral displacement profiles for Day 0 and Day 160. By Day 44, approximately half the total incremental

movement had occurred in response to excavation at the center of the cut. From Day 44 to Day 147, a berm was left in place against the wall of the cut. The approximate dimensions of the berm are shown in the cut. The approximate dimensions of the berm are shown in the figure. Owing to a general labor strike, no additional excavation was performed during this time interval. The wall movements increased from Day 44 to Day 147, until 80% of the total incremental displacement had taken place.

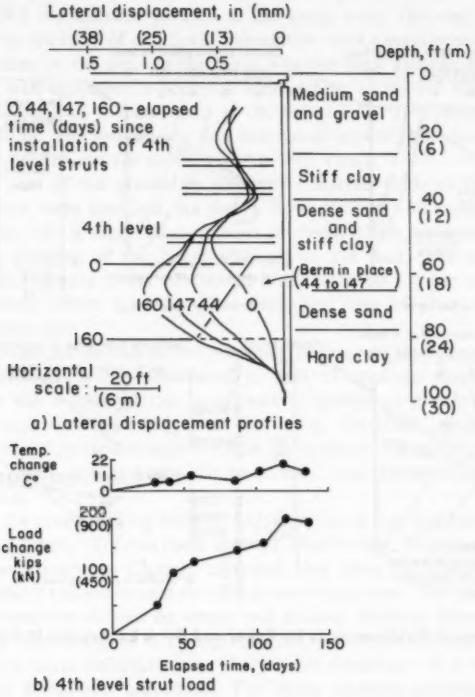

FIG. 10.—Observed Lateral Displacements and Strut Loads Associated with Berm Performance

Fig. 10 shows the change in average load for the fourth level struts as a function of time since their installation and preloading. The load increased steadily as the central portion of excavation was deepened with the berm in place. The average load increased approximately 180 kips (800 kN) from an initial preload of 90 kips (400 kN). Although increased temperature affected the load, the influence of temperature was small relative to that of the excavation and deformation of the berm.

The close relationship between deformation and load emphasizes the important effects that berms may have on the earth pressure distributed to the lowest braces. Although the magnitude of increased displacement caused by berm deformation was small, the load imposed on the bottom struts was very high.

When berms are used during excavation in soft to medium clays, the magnitude and time dependency of movements will increase substantially in comparison to those which will occur for excavation in sand. As an example, Fig. 11 summarizes the displacements measured during the excavation of a deep basement in Chicago.

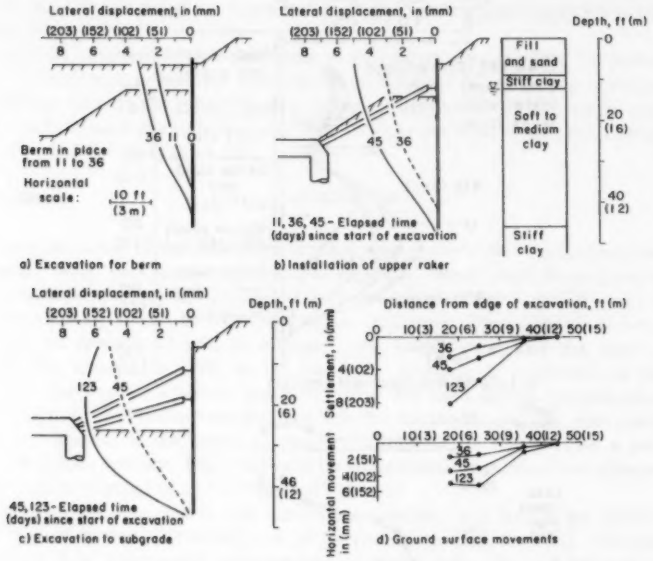

FIG. 11.—Observed Displacements for Raker and Berm Excavation in Soft to Medium Clay

The 26 ft (8 m) deep excavation was extended through approximately 13 ft (4 m) of sand and stiff clay and 13 ft (4 m) of soft clay. The bottom of the cut was underlain by 20 ft (6 m) of soft to medium clay. The excavation wall was composed of steel sheet piles (MZ-38) driven to a stratum of stiff clay approximately 46 ft (14 m) below the ground surface. Measurements are summarized for three distinct stages of excavation and support. As shown in the figure, these stages include: (1) Excavation at the center of the cut with a berm adjacent to the wall (2) partial excavation of the berm and installation of the upper rakers; and (3) continued excavation of the berm and installation of the bottom rakers. All displacements and levels of excavation are referenced to the start of open cutting (Day 0).

As shown in Fig. 11, the initial excavation was performed in conjunction with a berm, 15 ft (4.5 m) wide at its top and inclined at a grade of IV:1.5H from 15 ft–26 ft (4.5 m–8 m) below the ground surface. From Day 11 to Day 26, the volume of inward wall movement doubled in response to gradual deformation of the berm even though no additional excavation was performed. On Day 45, when the upper level rakers were installed, the berm had been cut back to about 70% of its initial volume. The rakers were not preloaded. During this time, wall movements were influenced by the driving of sheet piles for an elevator pit. The piles were driven 16 ft (5 m) inside the excavation for a 35 ft (19.5 m) distance parallel to the north wall. The wall deformation was primarily in the form of cantilever movement, with a maximum displacement of 5 in. (127 mm) at the top. As the berm was cut back and the bottom rakers installed, the wall movements occurred increasingly as inward bulging. In Fig. 11, the maximum wall displacement is shown as 7 in. (178 mm) at the base of the excavation. The settlements and horizontal movements measured on the street adjacent to the cut are summarized in Fig. 11(*d*).

The major part of the ground movements occurred prior to Day 45, when the upper rakers were installed. As shown by increased wall deformation from Day 11 to Day 36, a significant portion of these displacements was caused by a gradual yielding of the berm adjacent to the wall. The measurements at this site corroborate those of Clough and Davidson (3) for an excavation in San Francisco where a similar time-dependent loss of ground was caused by berm deformation.

These observations emphasize the potential for large displacements when berm and raker excavations are performed in soft to medium clays. Successive reductions in the weight of the berm lead to increased plastic heave at the base of the excavation. Cutting back the berm, therefore, results in loss of both horizontal and vertical restraint. Under these circumstances, it seems prudent to use large berms and to brace the excavation wall firmly at an early stage of construction.

Guidelines for proportioning berms in soft to medium clay have been developed by Clough and Denby (4) from finite element simulations. Experience with berm and raker construction in Chicago indicates that these guidelines can provide a good estimate of soil movement as a function of berm size. The time dependency of berm deformation caused by creep and gradual attrition from construction activities will contribute to soil displacement. Furthermore, the displacement associated with berm deformation is likely to be composed of a relatively large component of horizontal movement. For these reasons, guidelines and rules of thumb should be used carefully and linked with construction procedures that minimize the time lag between excavation at the center of the cut and the installation of stiff braces.

Conclusions

Because braced excavations often call for the integration of several distinct activities within the general construction plan, ground losses from each activity should be evaluated when estimating displacements. During site preparation, ground movements may be caused by: (1) Relocating and underpinning utilities;

(2) dewatering; (3) construction of the excavation wall; and (4) installation of deep foundations.

Field observations and model test data show a direct relationship between wall deformation and the ratio of horizontal movement of settlement adjacent to the cut. As cantilever-type movements are allowed to dominate during construction, the proportion of horizontal to vertical movement increases and, in the limit, approaches a value of approximately 1.6. Conversely, if the wall is braced firmly at an early stage of excavation, inward deflection of the wall will lead to horizontal movements that are significantly less than settlements. Under these conditions, the ratio of horizontal movement to settlement may be as low as 0.6. The ratio will decrease further if consolidation occurs.

Preloading is essential to promote a stiff bracing system and thereby restrict wall movement. Nevertheless, practices that call for very high preloads are likely to cause local concentrations of earth pressure that may exceed the pressures assumed during design. In most cases cross-lot struts prestressed to 50% of their design load will be sufficiently rigid to restrict further movement at the level of support and sufficiently low in load to avoid being overstressed as additional excavation occurs.

Limiting the excavation depth beneath the lowest braces is important for preventing ground loss during open cutting. For close control of ground movements experience in Washington, D.C. implies that excavation depths should be limited to a maximum 18 ft (5.5 m) beneath the lowest braces for deep cuts in medium to dense sands and interbedded sands and stiff clay.

Sloughing, seepage, creep, and construction activity will lead to the gradual distortion of berms. Time-dependent deformations contribute to ground loss, particulary when berms are used for excavations in soft to medium clays. Experience in Chicago indicates that guidelines developed by Clough and Denby (4) for proportioning berms can provide a good estimate of soil movement as a function of berm size. To control ground movements, the time lag between excavation at the center of the cut and the installation of stiff braces should be minimal.

Acknowledgments

Special recognition is extended to T. R. Maynard of the Bureau of Engineering of the City of Chicago for helping to obtain records of braced cut displacements and sharing his insights on excavation behavior. Thanks is extended to E. J. Cording and M. D. Boscardin of the University of Illinois at Urbana for their assistance in acquiring and analyzing portions of the data. W. R. Sawbridge and T. M. Foote drafted the figures and typed the manuscript, respectively.

Appendix I.—References

1. Baker, C. N., Jr., and Khan, F., "Caisson Construction Problems and Correction in Chicago," *Journal of the Soil Mechanics and Foundations Engineering Division*, ASCE, Vol. 97, No. SM2, Proc. Paper 7934, Feb., 1971, pp. 417–440.
2. Burland, J. B., and Wroth, C. P., "Settlement of Buildings and Associated Damage," *Proceedings of the Conference on Settlement of Structures*, Pentach Press, London, England, 1975, pp. 611–654.
3. Clough, G. W., and Dividson, R. R., "Effects of Construction on Geotechnical

Performance," *Proceeings of Specialty Session III,* Ninth International Conference on Soil Mechanics and Foundation Engineering, Tokyo, Japan, 1977, pp. 15–53.
4. Clough, G. W., and Denby, G. M., "Stabilizing Berm Design for Temporary Walls in Clay," *Journal of the Geotechnical Engineering Division,* ASCE, Vol. 103, No. GT2, Proc. Paper 12745, Feb., 1977, pp. 75–90.
5. Clough, G. W., Hansen, L. A., and Mana, A. I., "Prediction of Supported Excavation Movements Under Marginal Stability Conditions in Clay," *Proceedings of the Third International Conference on Numerical Methods in Geomechanics,* A. A. Balkema, Rotterdam, Netherlands, 1979, pp. 1485–1502.
6. Davisson, M. T., and Gill, H. J., "Laterally Loaded Piles in a Layered Soil System," *Journal of the Soil Mechanics and Foundations Engineering Division,* ASCE, Vol. 89, No. SM3, Proc. Paper 3509, May, 1963, pp. 63–94.
7. Drossel, M. G., "Braced Sheet Piling Shores High-Rise Building Excavation in Poor Soil," *Construction Methods and Equipment,* Vol. 57, No. 8, pp. 38–40.
8. Goldberg, D. T., Jaworski, W. E., and Gordon, M. D., "Lateral Support Systems and Underpinning," *Report No. FHWA-RD-75-128,* Vol. 1, Federal Highway Administration, Apr., 1976.
9. Jaworski, W. E., "An Evaluation of the Performance of a Braced Excavation," thesis presented to the Massachusetts Institute of Technology, in Cambridge, Mass., in 1973, in partial fulfillment of the requirements for the degree of Doctor of Philosophy.
10. Lukas, R. G., and Baker, C. N., Jr., "Ground Movement Associated with Drilled Pier Installations," Presented at the April, 1978, ASCE Spring Convention, held at Pittsburgh, Pa. (Preprint 3266).
11. Milligan, G. W. E., "The Behavior of Rigid and Flexible Retaining Walls in Sand," thesis presented to the University of Cambridge, in Cambridge, England, in July, 1974, in partial fulfillment of the requirements for the degree of Doctor of Philosophy.
12. O'Rourke, T. D., "A Study of Two Braced Excavations in Sands and Interbedded Stiff Clay," thesis presented to the University of Illinois, at Urbana, Ill., in 1975, in partial fulfillment of the requirements for the degree of Doctor of Philosophy.
13. O'Rourke, T. D., and Cording, E. J., "Observed Loads and Displacements for a Deep Subway Excavation," *Proceedings of the Rapid Excavation and Tunnelling Conference,* Vol. 2, San Francisco, Calif., pp. 1305–1326.
14. O'Rourke, T. D., Cording, E. J., and Boscardin, M., "The Ground Movements Related to Braced Excavations and Their Influence on Adjacent Buildings," *Report No. DOT-TST-76T-23,* U.S. Department of Transportation, Aug., 1976.
15. Palmer, J. H. L., and Kenney, T. C., "Analytical Study of a Braced Excavation in Weak Clay," *Canadian Geotechnical Journal,* Vol. 9, 1972, pp. 145–164.
16. Peck, R. B., "Deep Excavations and Tunneling in Soft Ground," *Proceedings of the Seventh International Conference on Soil Mechanics and Foundations Engineering, State-of-the-Art Volume,* 1969, pp. 225–290.
17. Scott, J. D., Wilson, N. E., and Bauer, G. E., "Analysis and Performance of a Braced Cut in Sand with Large Deformations," *Canadian Geotechnical Journal,* Vol. 9, No. 4, 1972, pp. 384–406.
18. Tait, R. G., and Taylor, H. T., "Rigid and Flexible Bracing Systems on Adjacent Sites," *Journal of the Construction Division,* ASCE, Vol. 101, No. CO2, Proc. Paper 11376, June, 1975, pp. 365–375.
19. Terzaghi, K., and Peck, R. B., *Soil Mechanics in Engineering Practice,* 2nd ed., John Wiley and Sons, Inc., New York, N.Y., 1968.
20. Tschebotarioff, G. P., *Foundations, Retaining and Earth Structures,* 2nd ed., McGraw-Hill Book Co., Inc., New York, N.Y., 1973.

Appendix II.—Notation

The following symbols are used in this paper:

A = cross-sectional area of brace;
C_D = coefficient of deformation;
d_H = horizontal ground surface displacement;

d_v = ground surface settlement;
E = elastic modulus of brace material;
K_E = effective strut stiffness;
K_I = ideal elastic strut stiffness;
L = length of brace;
P = average preload;
S_W = cantilever wall movement;
S'_W = inward bulging of wall; and
ΔS = average apparent strut deformation.

LATERALLY LOADED PILE DESIGN

By Robert L. Sogge,[1] M. ASCE

INTRODUCTION

Essentially three approaches (based on two different characterizations of soil strength) have been taken in the past to analyze laterally loaded piles. One of the most common methods formulates and solves the differential equation for deflection of the pile using a beam on elastic foundation approach (4). The soil strength is characterized using coefficients of subgrade reaction. A closed form solution of the governing differential equation is possible when the soil modulus is constant with depth. Otherwise, nondimensional solutions obtained using a difference equation formulation must be used.

An elasticity approach taken by Spillers and Stahl (8) and Poulos (5) describes the soil and structure as an elastic continuum. Such a formulation poses increased difficulty when the soil modulus varies with depth. The analysis is simplified by neglecting the horizontal shear stresses between the soil and the sides of the pile. The Poulos solution is limited by its assumption that the soil modulus is constant with depth.

The finite element method can be used to obtain solutions comparable to the differential equation and elasticity solutions. If the soil strength is defined using coefficients of subgrade reaction, then the difference equation solution is obtained (2). If instead, the soil is modeled as an elastic continuum, the elasticity solution is approximated (1).

The beam-on-elastic-foundation-coefficient-of-subgrade-reaction method gives comparable results to a solution which idealizes the soil as an elastic continuum. In a comparison between elastic and subgrade reactions solutions, Poulos (5) showed that generally, for all pile flexibilities, the subgrade reaction method slightly overestimates the moments, displacements, and rotations. Elastic moduli are most often obtained from triaxial compression tests performed in the laboratory. Coefficients of subgrade reaction are determined in the field by horizontal plate loading tests. In both, the actual stress path loading should be simulated. The uncertainties in predicting the elastic modulus and the coefficient of subgrade reaction are similar.

[1]Principal Consulting Geotechnical Engineer, Desert Earth Engineering, 524 N. 6th Ave., Tucson, Ariz. 85705.

Note.—Discussion open until February 1, 1982. To extend the closing date one month, a written request must be filed with the Manager of Technical and Professional Publications, ASCE. Manuscript was submitted for review for possible publication on May 27, 1980. This paper is part of the Journal of the Geotechnical Engineering Division, Proceedings of the American Society of Civil Engineers, ©ASCE, Vol. 107, No. GT9, September, 1981. ISSN 0093-6405/81/0009-1179/$01.00.

In this study a finite element approach with a subgrade reaction soil characterization is used to develop curves which eliminate the complex presentations which so often are associated with other methods. By expressing the behavior of laterally loaded piles in a common soil-structure interaction approach, clarification of the solution to a fashion useful to engineers results.

Formulation of Problem

Finite Element Model.—In certain mechanics problems the configuration of the system and its loading is such that the soil strength can be defined from coefficient of subgrade reaction relations between load and deformation for similar small-scale systems. A laterally loaded pile represents such a situation. Thus coefficients of subgrade reaction relating stress to displacement rather than to strain by an elastic modulus can be used. By this approach a simplified one-dimensional bar (spring) soil resistance representation (Fig. 1) can be used to obtain the same results achieved by more complex models which represent the soil as an elastic continuum.

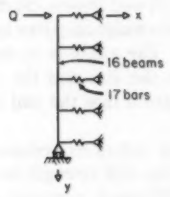

FIG. 1.—Beam-Bar Finite Element Model

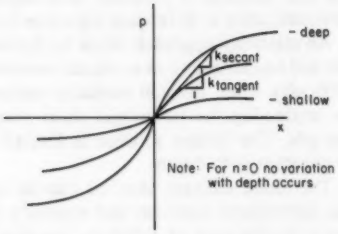

FIG. 2.—Net Soil Resistance

A laterally loaded pile can be handled using the finite element method by modeling the pile structure with beam elements and using bars to represent the uniaxial soil resistance. This approach in effect assumes independent or Winkler-type action for the springs. Any standard beam or beam-bar finite element program can be used to design laterally loaded pile systems. A bar can be represented using a beam element by either setting its moment of inertia, I, equal to 0 and supporting all three degrees of freedom on its free end or by setting I equal to a very small number and supporting the translational degrees of freedom. The equilibrium, stress-strain, and geometric compatibility relations for the beam elements are combined to form the stiffness relations relating the applied loads, P, to the displacements, x, for each element (6). The stiffness relations for bar elements are similarly developed.

For equilibrium of a bar element, the internal element forces, F, are related to the bar (soil) stresses, p, by

$$F = A\,p \quad \ldots \quad (1)$$

in which A = the contributory contact area of the soil. Stress-strain, p-ϵ, relations for the bar are

$$p = E\epsilon \quad \ldots \quad (2)$$

in which E = an elastic modulus. Geometric compatibility is given by

$$\epsilon = \frac{x}{L} \quad \ldots \quad (3)$$

in which L = the bar element length. The relation between pressure and displacement on the system level is given by

$$p = k\,x \quad \ldots \quad (4)$$

in which k = the coefficient of subgrade reaction. If the length of the bar is taken as unity in Eq. 3, then Eqs. 2 and 4 show that E can be replaced by k. The stiffness relation for a bar becomes

$$F = (Ak)\,x \quad \ldots \quad (5)$$

The constitutive equations for this model consist of coefficients formed by the addition of the beam element stiffnesses and bar element stiffnesses. For

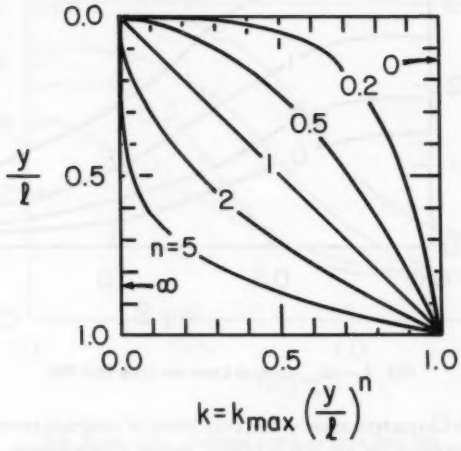

FIG. 3.—Subgrade Reaction Variation with Depth

these Winkler type spring resistances, the bar element stiffnesses form a diagonal stiffness array. When added to the beam element stiffnesses they form the following relation between the applied external nodal loads, P and the nodal displacements

$$\{P\} = [K]\{x\} \quad \ldots \quad (6)$$

The example finite element formulation for a two-beam and three-bar element system is presented in Appendix I.

The finite element model of the system is presented in Fig. 1. The 17-bar and 16-beam elements provide an adequate division of piles of any length in

order that the solution corresponds exactly to the closed form differential equation solution for a constant coefficient of subgrade reaction. The model does not consider the vertical shear stresses which may exist at the pile-soil interface nor those in the horizontal direction on the sides of the pile. A uniform stress distribution across the pile width is inherent in the method.

The magnitude and shape distribution of the moment along the pile is essentially identical throughout the pile for the three bottom tip support conditions of: (1) Pinned; (2) fixed against rotation and vertical movement; and (3) free except for vertical movement. The latter condition has been used in this study. For cases studied in this paper, elastic modulus, E, and moment of inertia, I, are constant along the pile length. The finite element model can also be readily used to develop soil-structure relations for the step-tapered piles so often used in offshore construction, and for those embedded in nonhomogeneous soils.

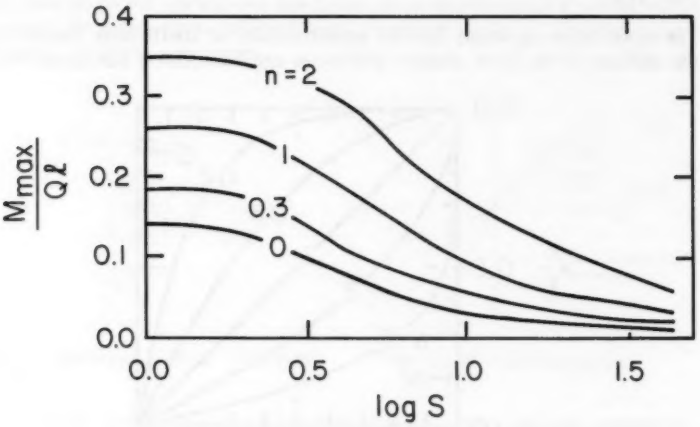

FIG. 4.—M_{max}-Lateral Load on Free-End Pile

Soil Strength Characterization.—The coefficient of subgrade reaction represents the relation between the net soil pressure, p, and displacement, x, for the soil surrounding the pile. This net resistance is the resisting, passive type stress, minus the imposing, active type stress existing on opposite sides of the pile. It is symmetrical about both the p and x axis as shown in Fig. 2 for various depths below the surface. The soil stress on each side of the pile can be determined by multiplying the displacement times coefficients of subgrade reaction which describe the passive or active type contribution to the net resistance. These values would be greater and less, respectively, than the coefficient describing the net resistance. The computed changes in stress on each side of the pile would be additions or deletions from the initial at-rest stress on each side of the pile which exists before the lateral load is applied.

The coefficient of horizontal subgrade reaction, k, can be related to a constant of subgrade reaction, k_1, and the pile width, B, by the equation

$$k = \frac{k_1 y^n}{B} \quad \ldots\ldots\ldots\

$$k_{max} = \frac{35 \text{ to } 300}{B}, \quad \text{in kips per cubic foot;}$$

$$\left(B, \text{ in feet, } 1 \text{ kcf} = \frac{159 \text{ kN}}{\text{cubic meters}}\right) \quad \ldots\ldots\ldots\ldots\ldots\ldots\ldots\ldots \quad (11)$$

in which q_u = the undrained compressive strength, in kips per square foot. The lower values are associated with soft clays, the higher values with stiff clays.

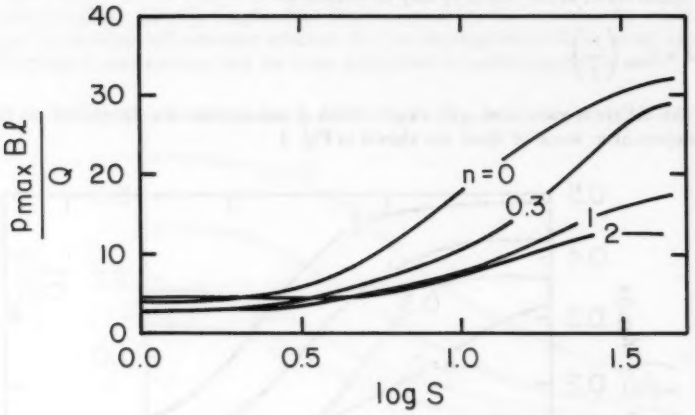

FIG. 6.—p_{max}-Lateral Load on Free-End Pile

Sands usually display a linear increase in stiffness with depth, i.e., $n = 1$. The values of k_{max} are in the range of

$$k_{max} = (2 \text{ to } 30)\frac{l}{B}, \quad \text{in kips per cubic foot;}$$

$$\left(B, \text{ in feet, } 1 \text{ kcf} = \frac{159 \text{ kN}}{\text{cubic meters}}\right) \quad \ldots\ldots\ldots\ldots\ldots\ldots\ldots\ldots \quad (12)$$

The maximum value of 30 limits the coefficient to approximately 100 times the passive earth pressure at any depth y. Such a limitation is valid at shallow pile depths. At deeper pile depths a better upper limit would be (50 l/B–100 l/B) kips/cu ft.

Values of the parameters k_{max} and n are dependent on the soil type, ground water table elevation, drainage conditions, time dependency, and nonlinearity present. There is a large range of variation on these values since they cannot be uniquely related to these specific conditions. In general, submerged soils will have values of k_{max} which are less than those for unsubmerged soils. The situation of a dry soil residing over a submerged soil can be represented by values of n which are greater than one. As the loading on the soils, either

due to the time rate of loading or to the drainage conditions, approaches an undrained case, values of k_{max} are closer to those given by Eq. 11. Soils for which the strength rapidly increases with confining pressure have values of n less than one.

Soil-Structure Interaction

Solutions for the three loading conditions of a free-end pile subject to a lateral load or moment and a fixed-end pile subject to a lateral load can best be presented in a form common to soil-structure interaction problems. By this form the response parameters, moment, shear, and deflection used to describe the behavior of the pile and the soil pressure are given as a function of the

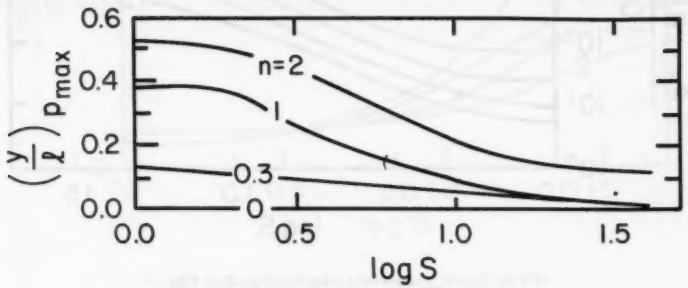

FIG. 7.—$(y/l)_{p_{max}}$-Lateral Load on Free-End Pile

ratio, S, of the stiffness of the soil to that of the structure. For a pile-soil system

$$\text{soil stiffness} \propto \sqrt[4]{B\,k_{max}} \quad \ldots \quad (13)$$

$$\text{and} \quad \text{structural stiffness} \propto \sqrt[4]{\frac{4EI}{l^4}} \quad \ldots \quad (14)$$

$$S = \sqrt[4]{\frac{B\,K_{max}\,l^4}{4EI}} \quad \ldots \quad (15)$$

The parameter S is the ratio of soil stiffness to structural stiffness and is identical to the nondimensional constant obtained in the solution to the governing differential equation for a beam on an elastic foundation by Hetenyi (3). In this expression since the soil stiffness is given for the entire structural section so should the moment of inertia be for the section of width B.

Maximum values of moment (M_{max}), shear (V_{max}), pressure (p_{max}), rotation (θ_{max}), and deflection (x_{max}) can be plotted for various values of S. Rowe (7) presented moment results for anchored sheetpiles in a similar manner. Limiting values for these response parameters can easily be calculated for the extreme condition of a rigid pile in a weak soil. For such a case the calculation of

these parameters is a determinate problem since the deflection pattern is known. Appendix II presents these results.

For the three loading conditions with piles of general flexibilities, interaction curves for M_{max}, V_{max}, P_{max}, θ_{max}, and x_{max}, as well as their locations have been developed using the finite element model described previously. These curves

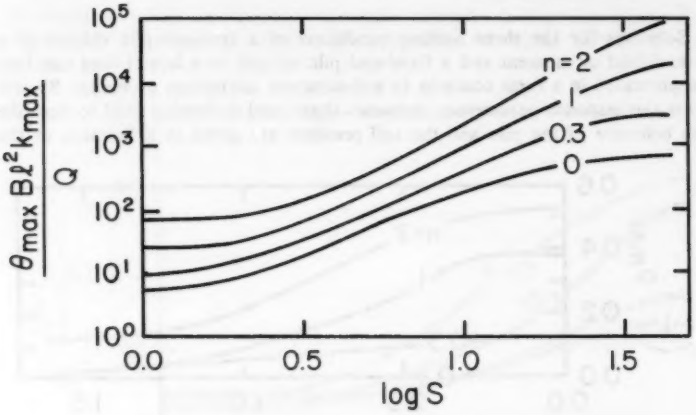

FIG. 8.—θ_{max}-Lateral Load on Free-End Pile

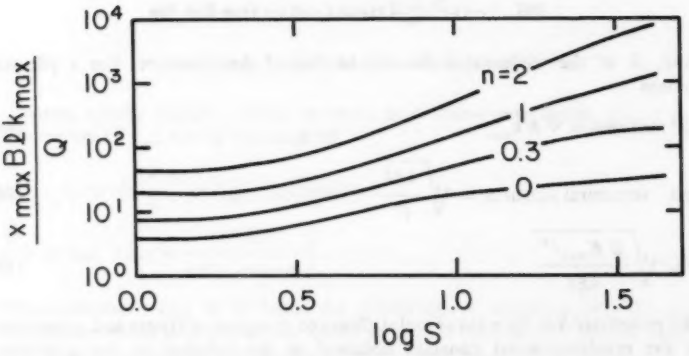

FIG. 9.—x_{max}-Lateral Load on Free-End Pile

are presented in Figs. 4–9 for the loading condition of a free-end pile subject to a lateral load, Figs. 10–15 for a free-end pile subject to an applied moment, and Figs. 16–19 for a fixed-end pile subject to a lateral load. The curves are restricted to working loads for which the soil strength can be characterized by a linear relation. Such working loads are generally in the range of 1/3–1/2

of the ultimate values. The curves are developed for a soil modulus variation with depth described by a shape exponent, n, equal to 0, 0.3, 1, and 2 in Eq. 9.

This development was conducted by using a specific value of lateral load or moment on piles, or both, idealized as in Fig. 1, and having different lengths,

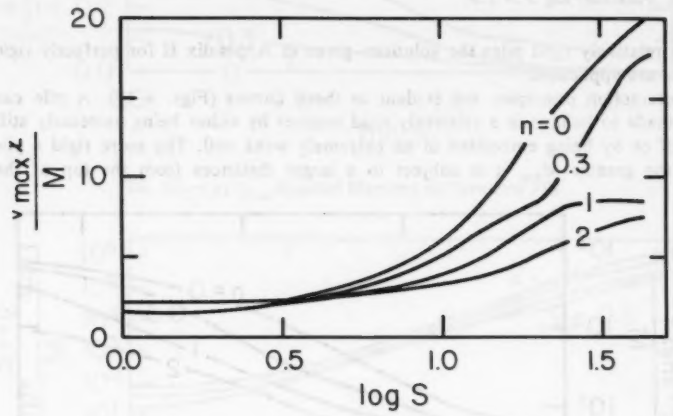

FIG. 10.—V_{max}-Applied Moment on Free-End Pile

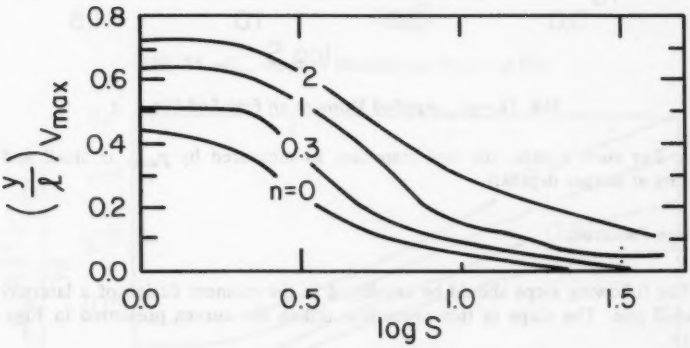

FIG. 11.—$(y/l)_{V_{max}}$-Applied Moment on Free-End Pile

section properties, and strengths, and embedded in soils having different stiffnesses as indicated by various values of coefficients of subgrade reaction. A nondimensional presentation permits a simpler development in which not all the variables need be changed. The nondimensional output parameters have values which are reduced or increased from those for a rigid pile. The behavior

of piles can be classified according to their relative stiffness ratio into the following approximate groupings:

1. Rigid: $\log S < 0.3$.
2. Intermediate: $0.3 < \log S < 1.3$.
3. Flexible: $\log S > 1.3$.

For relatively rigid piles the solutions given in Appendix II for perfectly rigid piles are applicable.

Interaction principles are evident in these curves (Figs. 4–19). A pile can be made to behave in a relatively rigid manner by either being extremely stiff itself or by being embedded in an extremely weak soil. The more rigid a pile is, the greater M_{max} it is subject to a larger distances from the top of the

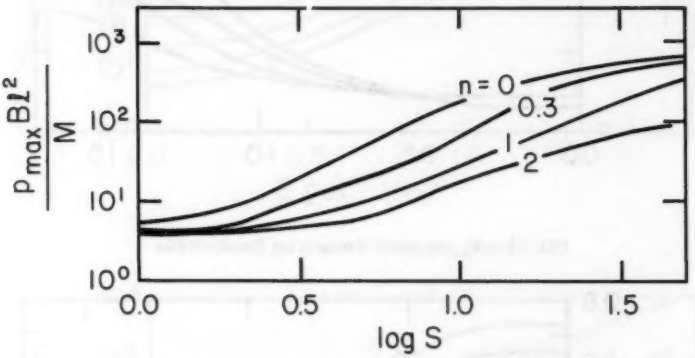

FIG. 12.—p_{max}-Applied Moment on Free-End Pile

pile. For such a case, the soil response, as measured by p_{max}, is small and occurs at deeper depths.

Design Procedure

The following steps should be employed in the moment design of a laterally loaded pile. The steps in this procedure utilize the curves presented in Figs. 4–19.

1. Choose a trial design pile having a specific length, l, elastic modulus, E, and allowable stress, σ_a.
2. Determine the maximum value of the coefficient of subgrade reaction, k_{max}, and its variation with depth, n. For overconsolidated clays, n may be zero and k_{max} is given by Eqs. 10 and 11. For sands, n is approximately one and k_{max} is given by Eq. 12. Any selection of these parameters for pure clay or sand soils as well as for mixtures of each will have some degree of uncertainty.

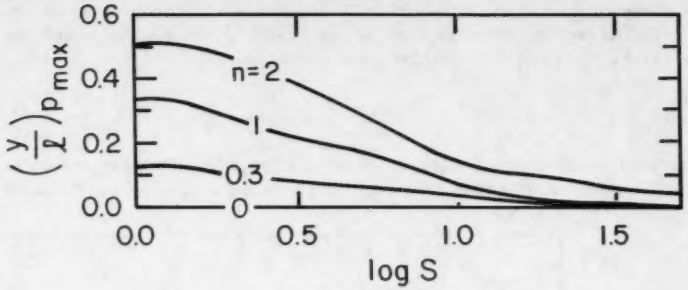

FIG. 13.—$(y/l)_{p_{max}}$-Applied Moment on Free-End Pile

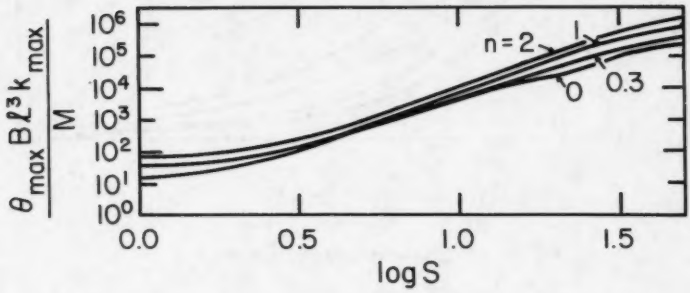

FIG. 14.—θ_{max}-Applied Moment on Free-End Pile

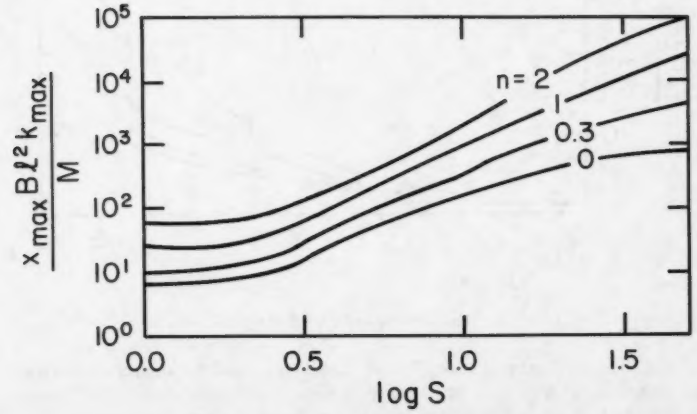

FIG. 15.—x_{max}-Applied Moment on Free-End Pile

3. Develop a structural curve for piles of various cross section having the specific l, E, and σ_a chosen in step 1. This curve is determined by calculating the maximum allowable moment the structure can sustain

$$(M_{max})_a = \frac{\sigma_a I}{z} \quad \ldots \ldots \ldots

4. Determine the approximate location of M_{max} for the applicable value of log S.

5. Determine the values of V_{max}, p_{max}, θ_{max}, and x_{max}. Evaluate whether the design assumption that the maximum net soil pressure, p_{max}, is less than 1/3 to 1/2 of the ultimate unit bearing capacity of the soil is verified. If not, the pile width should be increased. Approximate ultimate soil pressures are 5 q_u for cohesive soils and 3 times the passive Rankine pressure for piles in cohesionless soils. The maximum soil pressure on the passive side of the pile will be greater than p_{max} by the amount of the pressure existing on the active side of the pile.

6. Determine the approximate locations of V_{max} and p_{max} determined in step 5. The location of θ_{max} and x_{max} is always at the top of the pile.

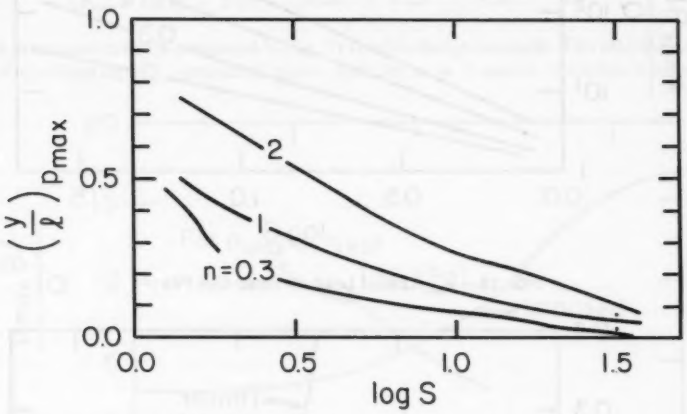

FIG. 18.—$(y/l)_{p_{max}}$-Lateral Load on Fixed-End Pile

Design Example.—The design procedure will be applied to the design of a pile embedded in a medium dense sand and subject to an applied 4 k(17.8 kN) lateral load.

1. A round timber pile will be chosen; $E = 1.5 \times 10^3$ ksi (10.3 MPa), $\sigma_a = 2$ ksi (13.8 MPa), $l = 20$ ft (6.1 m).
2. For the medium dense sand, $k_{max} = (15 \times 20)/B = 300/B$ kcf, $n = 1$.
3. $(M_{max})_a = \sigma_a I/z$.

B, in inches	6	8	10	12	14
(meters)	(0.152)	(0.203)	(0.254)	(0.305)	(0.356)
I, in inches^4	63.6	201	491	1,020	1,890
(meters$^4 \times 10^{-5}$)	(0.265)	(8.37)	(20.4)	(42.5)	(78.7)
M_{max}, in kip-feet	3.53	8.38	16.4	28.3	44.9
(kilonewton-meters)	(4.80)	(11.4)	(22.3)	(38.5)	(61.1)
$M_{max}/(Ql)$	0.044	0.105	0.205	0.354	0.561

$\log S = \log \sqrt[4]{(B\,k_{max}\,l^4)/(4EI)}$	1.06	0.940	0.843	0.763	0.696

Fig. 20 presents a plot superimposing this data on Fig. 4. The intersection yields an 8-in. section, which is subject to a moment of 8 kip-feet (11 kN-m).

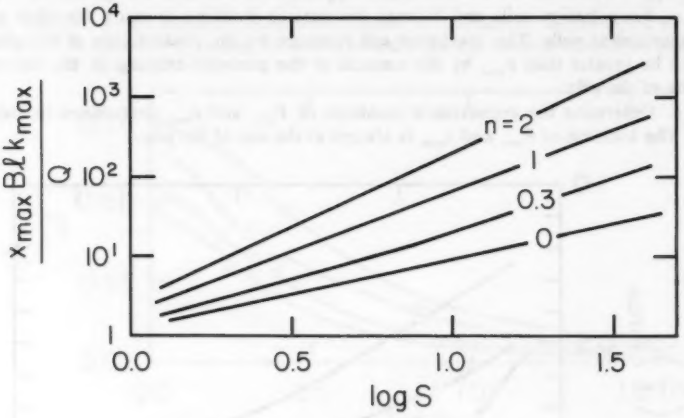

FIG. 19.—x_{max}-Lateral Load on Fixed-End Pile

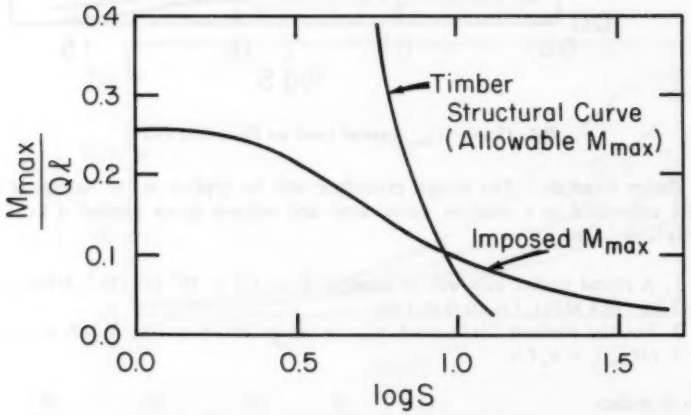

FIG. 20.—M_{max}-Structural and Interaction Curves-Design Example

4. Fig. 5: M_{max} located 3.5 ft (1.1 m) below top of pile.

5. By statics: V_{max} = 4 k (17.8 kN); Fig. 6: p_{max} = 2.1 ksf (100 kPa); Fig. 8: θ_{max} = 0.022 radians; and Fig. 9: x_{max} = 0.088 ft (27 mm).

6. V_{max}, θ_{max}, and x_{max} are located at top of pile; and Fig. 7: p_{max} located 2.5 ft (0.8 m) from top of pile. p_{max} is less than $1/2 \times 3 \times 5 \times .120$ kips/cu ft $\times$ 2.5 ft = 2.25 kips/sq ft (110 kPa).

For the design example presented, if it were desired to limit p_{max} to 1.5 ksf (72 kPa), a "structural curve" giving the maximum soil pressure allowed for each pile width versus the log S provided by that section must be developed as follows:

B, in inches (meters)	6 (0.152)	8 (0.203)	10 (0.254)	12 (0.305)	14 (0.356)
log S	1.06	0.940	0.843	0.763	0.696
$(p_{max} B l)/Q$	3.75	5.00	6.25	7.50	8.75

A structural curve is presented in Fig. 21 for this design example. The intersection of the limiting p_{max} structural curve with the $n = 1$ curve, provides a lower

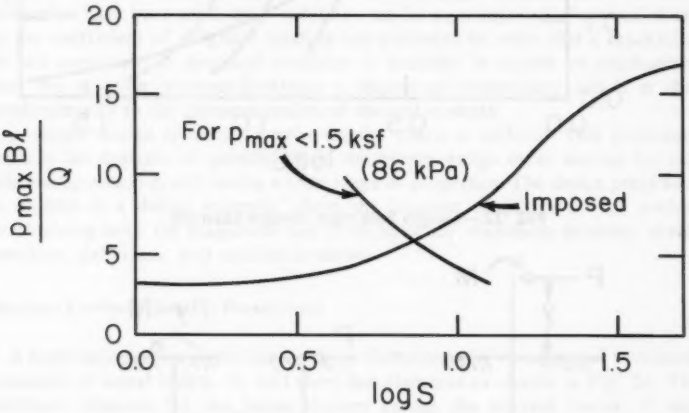

FIG. 21.—Limiting p_{max}: Design Example

bound on the required pile width. Thus for the design example a 10-in. (0.254-m) wide pile section or greater is required. A similar procedure could be used to limit S_{max} in this design example.

In the design procedure, a structural curve can be developed for shear in a similar manner to that for moment using instead $(V_{max})_a = \sigma_a A$. The structural curve for shear, applicable for the case of an applied moment at the top of the pile, is presented in Fig. 10.

Alternatively, a design approach which incorporates the pile length, l, as a variable follows by developing a set of structural curves for piles of different lengths in step 3 of the design procedure. For the design problem, using additional pile lengths of 10 ft and 40 ft (3.0 m and 12.2 m), the following structural curve results:

B, in inches (meters)	6 (0.152)	8 (0.203)	10 (0.254)	12 (0.305)	14 (0.356)
$M_{max}/(Ql)$ l = 10 ft (3.0 m)	0.088	0.210	0.410	0.708	1.12
$M_{max}/(Ql)$ l = 40 ft (12.2 m)	0.022	0.052	0.103	0.177	0.281

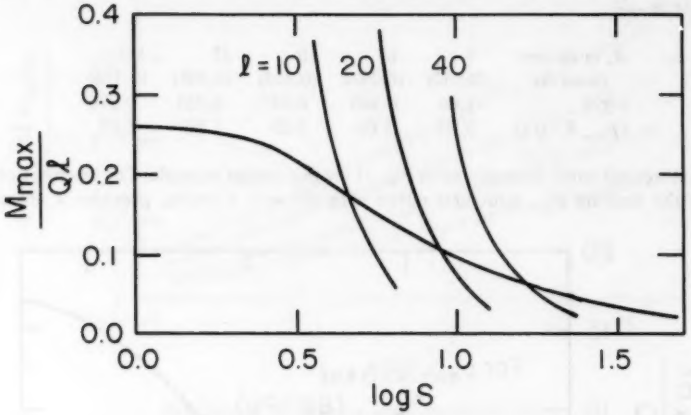

FIG. 22.—Length Selection: Design Example

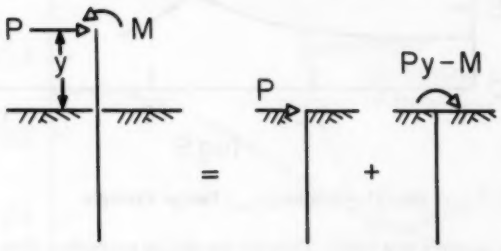

FIG. 23.—Superposition of Loadings

log S, l = 10 ft (3.0 m)	0.763	0.639	0.542	0.462	0.395
log S, l = 40 ft (12.2 m)	1.37	1.24	1.14	1.06	0.997

Fig. 22 shows such curves. The intersections of the structural curves with the imposed M_{max}/Ql curve yield the design section which must be used for each particular pile length.

For piles having a ground surface and top which do not coincide, the loading can be broken into the two cases shown in Fig. 23. Since a linear k has been

assumed, the solutions given in Figs. 4–9 for a lateral load and Figs. 10–15 for an applied moment at the ground surface can be superimposed. In the superposition, it must be remembered that maximums occurring at different points along the pile cannot be added directly.

Summary and Conclusions

This study has developed the solution to a laterally loaded pile by a formulation in terms of soil-structure interaction procedures. These procedures can be implemented by any beam or beam-bar finite element program.

The finite element method, incorporating a linear subgrade reaction soil characterization, has been used to develop curves defining the maximum moment, shear, pressure, deflection, and rotation in a laterally loaded pile versus the soil-structure stiffness ratio. Companion curves which prescribe the location of these maximum values are developed as well. The three tip-end conditions of: (1) Lateral load applied to free end; (2) moment applied to free end; and (3) lateral load with fixed-end rotation have been analyzed. Since linear material properties have been used, these solutions can be superimposed. Four variations of the coefficient of subgrade reaction are evaluated in order that a bracketing of soil conditions in practical problems is possible. It should be emphasized that the solution obtained contains a degree of uncertainty which is due predominantly to the characterization of the soil strength.

A simple design procedure employing the charts is outlined. This procedure enables the designer to quickly obtain the proper design cross section for any pile configuration in soil having a wide range of properties. The design procedure is applied in a design example where the inherent simplicity of the method in obtaining both the magnitude and location of the maximum moment, shear, pressure, deflection, and rotation is shown.

Appendix I.—Finite Element Formulation

A formulation is developed for the finite element model consisting of two-beam elements of equal length, L, and three-bar elements as shown in Fig. 24. The stiffness relations for one beam element having the internal forces, F, and deformations, x, shown in Fig. 25 are

$$\begin{Bmatrix} F_1 \\ F_2 \\ F_3 \\ F_4 \end{Bmatrix} = \begin{bmatrix} \frac{12\,EI}{L^3} & -\frac{6\,EI}{L^2} & -\frac{12\,EI}{L^3} & -\frac{6\,EI}{L^2} \\ & \frac{4\,EI}{L} & \frac{6\,EI}{L^2} & \frac{2\,EI}{L} \\ & \text{Sym} & \frac{12\,EI}{L^3} & \frac{6\,EI}{L^2} \\ & & & \frac{4\,EI}{L} \end{bmatrix} \begin{Bmatrix} x_1 \\ x_2 \\ x_3 \\ x_4 \end{Bmatrix} \quad \ldots\ldots\ldots \quad (16)$$

The stiffness relation for an individual bar element (Fig. 25) has been given

by Eq. 5. The internal deformations for the beam and bar elements are identical to the deformation occurring at the nodes of the system and thus both are denoted by x.

The system stiffness array for the 5-element model is formed by adding the element stiffnesses representing the internal bar and beam element forces at

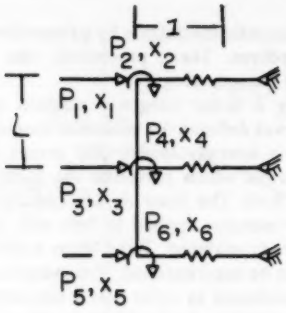

FIG. 24.—Finite Element Model Formulation

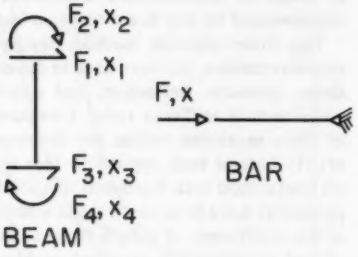

FIG. 25.—Internal Force Deformation Notations

each node. The result is the following explicit form of Eq. 6 for the 5-element model:

$$\begin{Bmatrix} P_1 \\ P_2 \\ P_3 \\ P_4 \\ P_5 \\ P_6 \end{Bmatrix} = \begin{bmatrix} \left(\frac{12\,EI}{L^3} + \frac{LBk}{2}\right) & -\frac{6\,EI}{L^2} & -\frac{12\,EI}{L^3} & -\frac{6\,EI}{L^2} & 0 & 0 \\ & \frac{4\,EI}{L} & \frac{6\,EI}{L^2} & \frac{2\,EI}{L} & 0 & 0 \\ & & \left(\frac{24\,EI}{L^3} + LBk\right) & 0 & -\frac{12\,EI}{L^3} & -\frac{6\,EI}{L^2} \\ & \text{Sym} & & \frac{8\,EI}{L} & \frac{6\,EI}{L^2} & \frac{2\,EI}{L} \\ & & & & \left(\frac{12\,EI}{L^3} + \frac{LBk}{2}\right) & \frac{6\,EI}{L^2} \\ & & & & & \frac{4\,EI}{L} \end{bmatrix} \begin{Bmatrix} x_1 \\ x_2 \\ x_3 \\ x_4 \\ x_5 \\ x_6 \end{Bmatrix} \quad (17)$$

Any given loading condition at the ground surface is specified by assigning values to the lateral load, P_1, applied moment, P_2, or rotational displacement, x_2, or both, at the top of the pile. Solution of the simultaneous equations for the loading condition specified yields the nodal displacements. The internal forces in the pile can then be obtained by using Eq. 16, representing the beam element stiffness. The soil stress is obtained by using the nodal deformations in Eq. 4 for each bar element.

Appendix II.—Rigid Pile Relations

For a rigid pile embedded in a soil having a stiffness relation $k = k_{max}(y/l)^n$ subjected to a lateral load of magnitude Q at the ground surface, the following nondimensional relations exist:

$$\frac{M_{max}}{Ql} = \left(\frac{y}{l}\right)_{M_{max}} - (n+2)\left(\frac{y}{l}\right)^{n+2}_{M_{max}} + (n+1)\left(\frac{y}{l}\right)^{n+3}_{M_{max}} \quad \ldots\ldots\ldots (18)$$

in which $(y/l)_{M_{max}}$ is obtained from the solution to

$$(n+1)(n+3)\left(\frac{y}{l}\right)^{n+2} - (n+2)^2\left(\frac{y}{l}\right)^{n+1} + 1 = 0 \quad \ldots\ldots\ldots\ldots (19)$$

$$\frac{V_{max}}{Q} = 1 \quad \text{(at top)} \quad \ldots\ldots\ldots\ldots\ldots\ldots\ldots\ldots (20)$$

$$\frac{p_{max}Bl}{Q} = (n+2)^2\left[\frac{n(n+2)}{(n+1)(n+3)}\right]^n \quad \ldots\ldots\ldots\ldots\ldots\ldots (21)$$

$$\left(\frac{y}{l}\right)_{p_{max}} = \frac{n(n+2)}{(n+1)(n+3)} \quad \ldots\ldots\ldots\ldots\ldots\ldots\ldots (22)$$

$$\frac{\theta_{max}Bl^2k_{max}}{Q} = (n+1)(n+2)(n+3) \quad \text{(at top)} \quad \ldots\ldots\ldots\ldots (23)$$

$$\frac{x_{max}Blk_{max}}{Q} = (n+1)(n+2)^2 \quad \text{(at top)} \quad \ldots\ldots\ldots\ldots\ldots (24)$$

For this case p_{max} shifts from near the top to the bottom as the rigidity becomes more pronounced. The value given is its magnitude near the top.

For a rigid pile embedded in a soil having a stiffness expressed by $k = k_{max}(y/l)^n$ and subject to an applied moment M at ground surface the following nondimensional relations exist:

$$\frac{M_{max}}{Ql} = 1 \quad \text{(at top)} \quad \ldots\ldots\ldots\ldots\ldots\ldots\ldots\ldots (25)$$

$$\frac{V_{max}l}{M} = (n+3)\left(\frac{n+1}{n+2}\right)^{n+1} \quad \ldots\ldots\ldots\ldots\ldots\ldots\ldots (26)$$

$$\left(\frac{y}{l}\right)_{V_{max}} = \frac{n+1}{n+2} \quad \ldots\ldots\ldots\ldots\ldots\ldots\ldots\ldots (27)$$

$$\frac{p_{max}Bl^2}{M} = (n+2)(n+3)\left(\frac{n}{n+2}\right)^n \quad \ldots\ldots\ldots\ldots\ldots\ldots (28)$$

$$\left(\frac{y}{l}\right)_{p_{max}} = \frac{n}{n+2} \quad \ldots\ldots\ldots\ldots\ldots\ldots\ldots\ldots (29)$$

$$\frac{\theta B l^3 k_{max}}{M} = (n+2)^2(n+3) \quad \text{(at top)} \quad \ldots\ldots\ldots\ldots\ldots\ldots \quad (30)$$

$$\frac{x_{max} B l^2 k_{max}}{M} = (n+1)(n+2)(n+3) \quad \text{(at top)} \quad \ldots\ldots\ldots\ldots\ldots \quad (31)$$

The following nondimensional relations exist for a rigid pile embedded in a soil having a stiffness relation $k = k_{max}(y/l)^n$ with the top of the pile being fixed at the ground surface and subject to a lateral load, Q, at this level:

$$\frac{M_{max}}{Ql} = \frac{n+1}{n+2} \quad \text{(at top)} \quad \ldots\ldots\ldots\ldots\ldots\ldots\ldots\ldots \quad (32)$$

$$\frac{V_{max}}{Q} = 1 \quad \text{(at top)} \quad \ldots\ldots\ldots\ldots\ldots\ldots\ldots\ldots\ldots \quad (33)$$

$$\frac{p_{max} Bl}{Q} = n+1 \quad \text{(at bottom)} \quad \ldots\ldots\ldots\ldots\ldots\ldots \quad (34)$$

$$\frac{x_{max} B l k_{max}}{Q} = n+1 \quad \text{(constant with depth)} \quad \ldots\ldots\ldots\ldots \quad (35)$$

Appendix III.—References

1. Desai, C. S., and Appel, G. C., Jr., "3-D Analysis of Laterally Loaded Structures," *Proceedings of the 2nd International Conference on Numerical Methods in Geomechanics*, Vol. I, Blacksburg, Va., June, 1976, pp. 405–418.
2. Desai, C. S. and Kuppusamy, T., "Procedure for a Soil-Structure Interaction Problem: Analysis and Evaluation," *Proceedings*, ASCE, Computing in Civil Engineering, Atlanta, Ga., June, 1978, pp. 200–218.
3. Hetenyi, M., *Beams on Elastic Foundation*, University of Michigan Press, Ann Arbor, Mich., 1946, 255 pp.
4. Matlock, H., and Reese, L. C., "Generalized Solutions for Laterally Loaded Piles," *Journal of the Soil Mechanics and Foundations Division*, ASCE, Vol. 86, No. SM5, Proc. Paper 2626, Oct., 1969, pp. 63–91.
5. Poulos, H. G., "Behavior of Laterally Loaded Piles: I-Single Piles," *Journal of the Soil Mechanics and Foundations Division*, ASCE, Vol. 97, No. SM5, Proc. Paper 8092, May, 1971, pp. 711–731.
6. Przemieniecki, J. S., *Theory of Matrix Structural Analysis*, McGraw-Hill Book Co., Inc., New York, N.Y., 1968, 468 pp.
7. Rowe, P. W., "Anchored Sheet Pile Walls," *Proceedings*, Institution of Civil Engineers, London, England, Vol. I, Part I, Paper No. 5788, Jan., 1952, pp. 27–70.
8. Spillers, W. R., and Stoll, R. D., "Lateral Response of Piles," *Journal of the Soil Mechanics and Foundations Division*, ASCE, Vol. 90, No. SM6, Proc. Paper 4121, Nov., 1964, pp. 1–9.
9. Terzaghi, K., "Evaluation of Coefficients of Subgrade Reaction," *Geotechnique*, London, England, Vol. 5, No. 4, Dec., 1955, pp. 297–326.

Appendix IV.—Notation

The following symbols are used in this paper:

A = cross-sectional area of bar element;
B = pile width or diameter;

E = elastic modulus;
F = internal element force;
I = moment of inertia;
K = array of stiffness coefficients;
k = coefficient of subgrade reaction;
k_1 = constant of horizontal subgrade reaction;
L = element length;
l = pile length;
M = bending moment;
n = shape exponent;
P = nodal loads;
p = net pressure (stress) in soil;
Q = lateral pile load;
q_u = undrained compressive strength;
S = nondimensional soil-structure stiffness ratio = $\sqrt[4]{(B\,k_{max}\,l^4)/(4EI)}$;
V = shear;
x = lateral displacement;
y = vertical distance along pile measured from ground surface;
z = distance from centroid of section to extreme outer fiber;
ϵ = strain;
θ = rotation angle in radians; and
σ = stress.

Subscripts

a = allowable; and
max = maximum.

Nonlinear Seismic Response of Soft Clay Sites

By Ram D. Singh,[1] A. M. ASCE, Ricardo Dobry,[2] Earl H. Doyle,[3] Members, ASCE and Izzat M. Idriss,[4] F. ASCE

Introduction

The behavior of soils under cyclic loading is basically nonlinear and hysteretic. The soil stress-strain model most widely used in analytical procedures for site response analysis is the equivalent linear technique incorporating strain-dependent stiffness and damping. The development of this equivalent linear approach has included a number of comparisons between analytical results and recorded ground motions. Nonlinear analyses are especially appropriate for soft clay sites where nonlinear and modulus degradation effects are more significant than at sites consisting of stiffer soils. However, the use of the nonlinear response analysis is a relatively new development, and there is a need for comparisons between motions computed by nonlinear methods and calibration with available records. This paper summarizes the results of such an effort.

Analytical Models

There are three basic issues in the development of realistic analytical procedures for site response analyses: (1) Characterization of the input motion; (2) modeling of the soil profile; and (3) stress-strain relation for the soil. Most developments and applications assume that the input motions are vertically propagating plane shear waves. For horizontally layered sites, response calculation reduces to the one-dimensional analysis of a shear beam of soil. The computer program SHAKE developed by Schnabel, et al. (22) incorporates the equivalent linear model. A number of case histories have presented comparisons between analytical results using this model and recorded ground motions (7,20). Also, some analytical studies have been performed comparing results of equivalent linear and nonlinear calculations (2,8,13,25).

During the past few years, a number of nonlinear models of stress-strain

[1]Sr. Project Engr., Woodward-Clyde Consultants, 5120 Butler Pike, Plymouth Meeting, Pa. 19462.

[2]Assoc. Prof., Dept. of Civ. Engrg., Rensselaer Polytechnic Inst., Troy, N.Y. 12181.

[3]Sr. Research Engr., Shell Development Co., Houston, Tex. 77025.

[4]Principal, Woodward-Clyde Consultants, San Francisco, Calif. 94111.

Note.—Discussion open until February 1, 1982. To extend the closing date one month, a written request must be filed with the Manager of Technical and Professional Publications, ASCE. Manuscript was submitted for review for possible publication on January 9, 1980. This paper is part of the Journal of the Geotechnical Engineering Division, Proceedings of the American Society of Civil Engineers, ©ASCE, Vol. 107, No. GT9, September, 1981. ISSN 0093-6405/81/0009-1201/$01.00.

behavior have been used, including the bilinear (8,17) and multilinear (11) representations for the backbone curve. Hyperbolic (18) and Ramberg-Osgood (2,9,24) idealizations have also been utilized. A number of nonlinear site response analyses using these models have been presented in the literature (3,4,9,11,12,18). Recently, the computer code DCHARM (9) was developed, which is specifically designed for the seismic response analysis of profiles containing soft clay layers. The code DCHARM was obtained by modifying the existing program CHARSOIL developed by Streeter, et al. (24), which is based on the use of the method of characteristics to solve the one-dimensional wave equation and uses the Ramberg-Osgood model for the backbone curve. The main modification consisted of adding the capability for degrading the backbone curve of the soil during cyclic loadings thus incorporating the modulus degradation model for soft clay developed by Idriss, et al. (10).

Selection of Sites for Analysis

For the present study, two sites were selected where strong motion earthquake records were available on soft clay deposits. These sites are: (1) Southern Pacific Building Site, San Francisco, California (March 22, 1957 earthquake); and (2) Station No. 119 Site, Tokyo, Japan (July 1, 1968 earthquake). Horizontal accelerograms obtained at the two sites, having peak accelerations of about 0.05 *g* and total record lengths of 10 sec–20 sec, were used to calibrate the nonlinear response method allowing for modulus degradation (DCHARM). The intensity of shaking in both cases was high enough for the stress-strain behavior of the soil to become nonlinear, but not high or long enough to cause significant modulus degradation of the soft clay.

At the two selected sites, information on subsurface conditions and properties of the soils was available. Nonlinear and degradation parameters for the San Francisco Bay Mud, which constitutes the soft layer at one of the sites, were available from an earlier cyclic testing program (10). Finally, accelerograms recorded simultaneously at neighboring rock or stiff sites were available in both

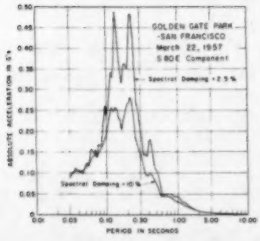

FIG. 1.—Recorded Acceleration Spectra on Rock, San Francisco

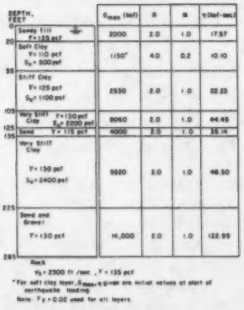

FIG. 2.—Soil Profile and Parameters for Response Analyses, Southern Pacific Building Site

cases, and were used to provide the input excitation. In San Francisco, a record on rock was obtained at Golden Gate Park about five miles from the soft Southern Pacific Building site. In Tokyo, a record on a stiff site at Station No. 118 was obtained about 20 miles from the soft site.

Southern Pacific Building Site, San Francisco

An earthquake of magnitude 5.3 along the San Andreas Fault was recorded on soil in the basement of the 11-story Southern Pacific Building, San Francisco (10.5 miles from the fault) on March 22, 1957. The earthquake was simultaneously recorded on rock at the Golden Gate Park USGS (United States Geological Survey) station. The Golden Gate Station is 7.0 miles from the epicenter and 5.0 miles from the Southern Pacific site (7). The acceleration response spectra of the S80E horizontal component recorded at Golden Gate for 2.5% and 10.0% spectral damping ratios are shown in Fig. 1.

Soil Profile and Soil Parameters

The soil conditions at the Southern Pacific building site were obtained from a previous study (7) and supplemented by appropriate values of unit weight and of shear wave velocity for the Franciscan shale rock underlying the site, as shown in Fig. 2. A sandy fill about 20 ft thick covers the site. Below the fill is a 35-ft layer of soft clay followed by stiff clay down to a depth of 225 ft; the stiff clay is interbedded with a 10-ft layer of dense sand at a depth of 125 ft. The stiff clay is underlain by a layer of dense sand and gravel, which extends to bedrock at a depth of 285 ft. The basic cyclic shear stress-strain behavior of the soil layers was specified by the Ramberg-Osgood equation of the backbone curve in the first cycle of loading (10):

$$\gamma = \gamma_y \left(\frac{\tau}{G_{\max} \gamma_y} \right) + \alpha \left(\frac{\tau}{G_{\max} \gamma_y} \right)^R \quad \ldots \ldots \ldots \ldots \ldots \ldots \ldots \ldots \ldots \ldots \quad (1)$$

in which: τ = shear stress; γ = shear strain; $G_{\max}$ = shear modulus at very small strains (10^{-4}%); and α, R, γ_y = soil parameters. The experience of the writers with modulus reduction curves of granular soils and stiff to very stiff clays indicates that, in the absence of test data, the use of the average curve for sands proposed by Seed and Idriss (19), is more appropriate than other proposed curves. Therefore, Ramberg-Osgood parameters, $R = 2$, $\alpha = 1.0$, and $\gamma_y = 0.02$%, selected to fit the average curve for sands, were used for all layers except the 30-ft soft San Francisco Bay Mud layer. For all SHAKE runs in this study the modulus reduction and damping curves by Seed and Idriss (19) were used. Cyclic triaxial tests were conducted on this soil and the results are available elsewhere (9,10). Fig. 3 shows stress-strain data for the first cycle of loading, together with the Ramberg-Osgood curve fitted to these results ($R = 4$, $\alpha = 0.2$, $\gamma_y = 0.02$ percent), and used in the present study. These Ramberg-Osgood parameters are slightly different from those presented in Ref. 10 for the same soil. The parameters in Ref. 10 represent a further refinement in the interpretation of the original test results. However, such small variations in these parameters have only minor effects on the results.

The damping provided by the Ramberg-Osgood parameters is very small at strains less than about 10^{-3}%. To provide a damping ratio of three percent at small strains, estimated on the basis of other laboratory tests on soft clays reported in the literature (19), a shear viscosity, η, was selected for each layer, using the equation:

$$\eta = \frac{\lambda T}{\pi} G_{max} \quad \ldots \ldots \ldots

input rock motions were used in both programs DCHARM and SHAKE. The input motion used was the S80E component recorded at the Golden Gate rock site, with the recorded accelerations multiplied by a factor of 0.65 to account for the different distances of the two sites to the source (7). Following the current state-of-the-art, the motion was input at a rock outcrop for the SHAKE analysis. For the DCHARM analysis, the input rock motion was assumed to act at the base of the soil profile.

Comparisons between recorded and computed acceleration and velocity response spectra near the ground surface using the SHAKE and DCHARM analyses are included in Figs. 4 and 5, respectively, for a spectral damping ratio of 2.5%. For this low damping, the differences between different models are accentuated. Examination of Figs. 4 and 5 indicates that a significantly better

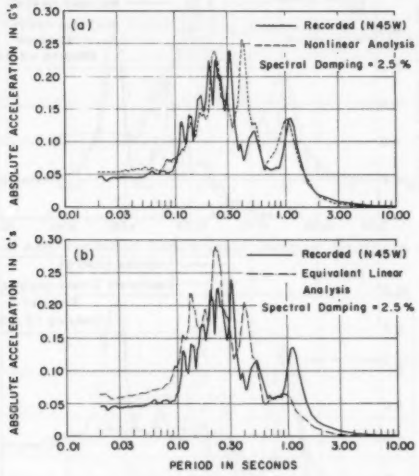

FIG. 4.—Computed and Recorded Acceleration Spectra, Southern Pacific Building

agreement with recorded motions was obtained with the nonlinear as compared to the equivalent linear method. The equivalent linear analysis somewhat overestimates the response in the low period range, and significantly underestimates the recorded peak at a period of about 1.1 sec. However, both the analyses predict a spurious peak at about 0.4 sec.

For the Southern Pacific Building site, the nonlinear analysis simulates the recorded motions better than the equivalent linear method. The improved agreement at about 1.1 sec is especially significant, because a comparison between recorded rock (Fig. 1) and soil (Fig. 4) spectra reveals that the peak at this period represents the main difference attributable to the presence of the soil. The small strain fundamental period of the soil profile at the Southern Pacific Building site is 0.95 sec, which increased in the SHAKE runs to 1.05 sec due to nonlinear effects; therefore, this peak in the spectrum can be associated

with the vibration of the first mode of the soil profile. It must be noted that the fundamental period of the building is also about 1.1 sec–1.2 sec and the building suffered substantial partition damage, presumably due to this peak in the soil spectrum (23). Due to the practical importance of this peak, it has been considered repeatedly in the literature (7,23), and the improved prediction by the nonlinear analysis is an important result of this study.

The calculated degradation index, δ, in the soft layer at the end of the shaking was 0.99, indicating a degradation of about 1% in modulus values of the soil during this earthquake. Therefore, the improved agreement between computed and recorded motions, previously mentioned, is due to the use of nonlinear modeling and not to the effect of degradation.

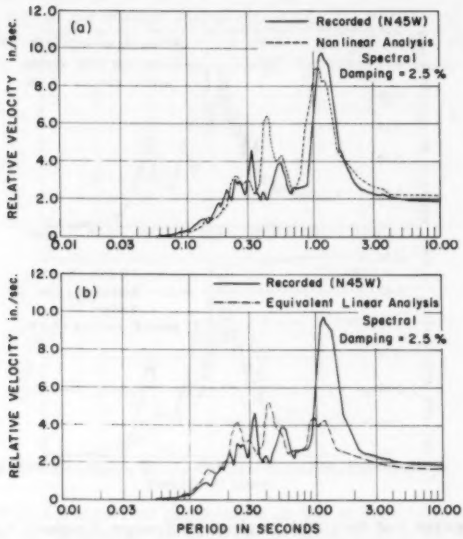

FIG. 5.—Computed and Recorded Velocity Spectra, Southern Pacific Building

For the nonlinear analyses previously considered, the recorded rock motion used for the input was measured along the S80E direction, and the computed motion was compared with an accelerogram recorded on soil along the N45W direction. These are 35° apart. Therefore, it was decided to include the other recorded horizontal soil component at the Southern Pacific Building (N45E) in the comparisons. Figs. 6 and 7 show comparisons between the computed acceleration and velocity response spectra, respectively, and the ranges defined by the two components of the recorded soil motions, for a spectral damping of 2.5%. Examination of Figs. 6 and 7 suggests that the good agreement provided by the nonlinear analysis is still valid if the two recorded components of the soil motion are considered.

The variation of level of shaking with time t is quantified by $\int_0^t a^2(t) \cdot dt$ where $a(t)$ is the acceleration time history. This integral is a measure of the energy of the accelerogram. Husid (6) plotted the buildup of this energy with time to study the evolution of the level of shaking.

In addition to the comparisons considered earlier between computed and recorded response spectra (frequency domain), comparisons in the time domain were performed. These included comparing the recorded N45W accelerogram at the Southern Pacific Building site, together with its corresponding Husid plot with the corresponding accelerograms and Husid plots calculated by the

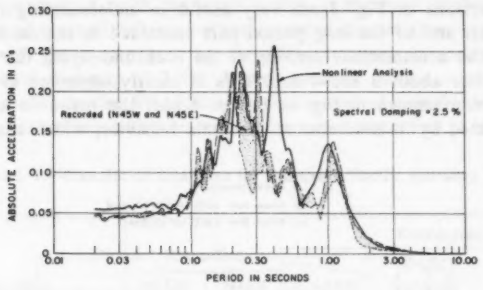

FIG. 6.—Computed and Recorded Acceleration Spectra, Southern Pacific Building

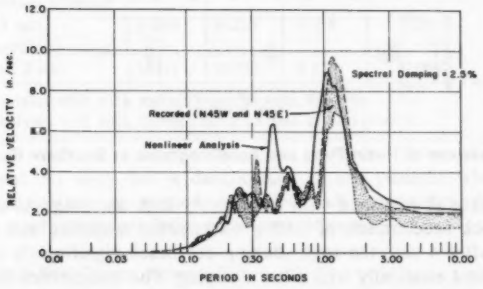

FIG. 7.—Computed and Recorded Velocity Spectra, Southern Pacific Building

nonlinear and equivalent linear analyses. These comparisons are presented in Fig. 8. The general appearance of the calculated and recorded motions are very similar, including the existence in both of a strong, high frequency part which ends at 4 sec–5 sec, followed by a long period part having smaller accelerations and a predominant period of the oscillations of about 1 sec–1.2 sec. The build-up of energy of the two records, as shown by the Husid plots in the upper part of Figs. 8(*a*) and 8(*b*), are also very similar. There is an almost straight-line steep increase of energy in both records until about 4 sec–6 sec, where there is a break in both plots that coincides with the end of the

strong part of the record; after this break, the plots are much flatter, due to the smaller accelerations of the long period part. The total energy at the end of both records is very similar, about $18\ g^2 - s \times 10^{-4}$–$19\ g^2 - s \times 10^{-4}$. Finally, the peak acceleration predicted by the nonlinear analysis is very similar to the recorded value (about 0.05 g). The long period part after 4 sec–6 sec which is present in both the recorded motion and the nonlinear simulation, is totally absent in the equivalent linear simulation [Fig. 8(*c*)]. The Husid plot from the SHAKE analysis in Fig. 8(*c*) is completely flat after about 4 sec with a total energy at the end of the record of about $12\ g^2 - s \times 10^{-4}$, significantly smaller than that for the recorded motion in Fig. 8(*a*).

The comparisons of Fig. 8 are very useful in understanding the origin of the strong part and of the long period part contained in the motion recorded at the site. The accelerations arriving at the rock underlying the site became very small after about 3 sec–4 sec. This is clearly observed in the Golden Gate rock record shown in Fig. 8. Before 4 sec, the response of the soil is strongly affected by its nonlinear stress-strain behavior, which caused the soil

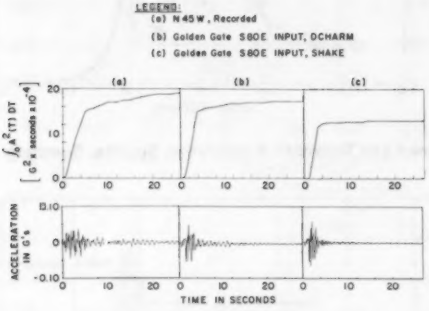
LEGEND:
(a) N 45 W, Recorded
(b) Golden Gate S 80 E INPUT, DCHARM
(c) Golden Gate S 80 E INPUT, SHAKE
(a)
(b)
(c)
20
10
0
10
20
0
10
20
0
10
20

It may be noted that this apparent deficiency in the equivalent-linear procedure can be overcome also by conducting a progressive analysis, similar to that previously used at the Union Bay site (20). Strain compatible modulus and damping values are applicable for only a part of the input and are changed and updated as the input motion is progressively applied to the analysis profile. In this way, it is possible, for example, to use higher modulus and lower damping values during the latter part of the input motion.

In the equivalent-linear analysis the rock motion was input at an outcrop, but in the nonlinear analysis the rock motion was input at the base of the soil profile. To quantify the importance of this effect, an additional SHAKE analysis was performed, with the input motion at the base of the soil profile. A comparison of spectral ordinates of the recorded accelerations at the Southern Pacific site with those computed by the different analyses is shown in Table 1, for a spectral damping of 2.5%. When the rock motions are input at the base of the profile in the SHAKE analysis instead of being input on a rock outcrop, the agreement with the recorded spectra improves at the period of

TABLE 1.—Results of Analyses for Southern Pacific Building Site

Parameter (1)	Recorded		Computed		
	N45W (2)	N45E (3)	DCHARM (4)	SHAKE outcrop[a] (5)	SHAKE interface[b] (6)
Peak acceleration	0.046 *g*	0.047 *g*	0.054 *g*	0.063 *g*	0.083 *g*
Peak of spectrum in range 0.2 sec–0.3 sec	0.226	0.223	0.238	0.291	0.351
Peak of spectrum in range of 0.9 sec–1.2 sec	0.137	0.089	0.136	0.065	0.127

[a]SHAKE analysis with rock motion input at rock outcrop.
[b]SHAKE analysis with rock motion input at base of soil profile.

the soil (about 1.1 sec), but it deteriorates at low periods. Therefore, only the nonlinear analysis performed using DCHARM provides, for this case, consistently good agreement for a wide range of periods.

Station No. 119 Site, Tokyo, Japan

The city of Tokyo, Japan, was shaken by the Higashi-Matsugama earthquake on July 1, 1968. The magnitude of the earthquake was about 6.4, its epicenter was located about 50 km to the northwest of Tokyo, and it had a focal depth of about 50 km. The earthquake was widely recorded by the strong motion network of the Tokyo region (15,16). Information on the recorded motions, including digitized printouts of the accelerograms, response spectra and soil information from borings at some of the stations has been published by the Association for Science Documents Information, Tokyo (1). The record for soft clay selected for this study is the NS component at Station No. 119, obtained at the basement of a two-story building. The record selected as control motion is the NS component at Station No. 118, obtained at the basement of a five-story

building on dense Tokyo gravel. Both stations were at similar distances from the epicenter (40 km–50 km), and the distance between the sites is about 30 km.

Unlike the case of the Southern Pacific site studies described earlier, Station No. 118 was not on rock but on shallow stiff soil, and it was also at some distance from the soft site at Station No. 119. Therefore, a somewhat different approach was utilized for the analyses at the Station No. 119 site. To estimate the peak bedrock acceleration at the site, available correlations were used for a magnitude 6.4 event at a hypocentral distance of approx 70 km. A value of 0.06 *g* was estimated and was used for the analyses (0.04 *g* had been recorded at the stiff site by Station No. 118). A value of about 0.35 sec was estimated for the predominant period of the rock motions.

Two input rock motions were used in the analyses. One of the input rock motions used was based on the NS component recorded at Station No. 118; the record was deconvolved using the program SHAKE to the Lower Tokyo Formation, and the deconvolved accelerogram was then adjusted to give a peak acceleration of 0.06 *g* and a predominant period of 0.35 sec. Acceleration spectra

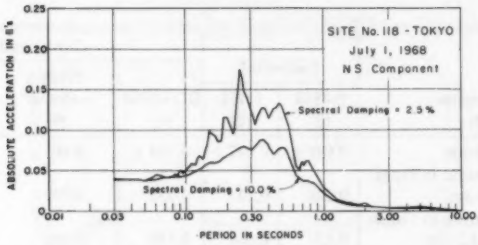

FIG. 9.—Recorded Acceleration Spectra at Stiff Site, Tokyo

of the recorded motion at Station No. 118 are shown in Fig. 9 for spectral damping values of 2.5% and 10%. The other accelerogram used as input rock motions was the N21E component of the Castaic strong-motion record obtained on rock during the 1971 San Fernando earthquake, which had a magnitude about equal to that of the Higashi-Matsugama event. This record was adjusted to give a peak acceleration of 0.06 *g*, while the original predominant period (0.32 sec) was left unchanged.

The use of two input rock motions, together with the variation in soil properties examined in the following, was designed to account for some of the uncertainties involved in the calculations. In this way, a limited parametric study was performed at site No. 119.

Soil Profile and Soil Properties

The soil profile at Tokyo Station No. 119 is shown in Fig. 10. The profile down to a depth of 140 ft was based on boring information given in Ref. 1. The profile below a depth of about 140 ft was based on data presented in Refs. 14 and 21. Bedrock was assumed at a depth of 500 ft. The site is overlain

by about 25 ft of silty sand and silty clay, followed by a 75-ft layer of soft silty clay. Below the soft clay there is medium stiff clay to a depth of 140 ft, followed by a 30-ft layer of Tokyo gravel. Between 170 ft and the tertiary bedrock there is a geologic unit known as Lower Tokyo Formation.

The soil and rock properties used in the analyses at Station No. 119 are listed in Fig. 10. The values of unit weight, γ_t, and of maximum shear modulus, G_{max}, were estimated based on a literature survey of Tokyo subsoil data and on correlations established by Ohsaki (14). The Ramberg-Osgood parameters were arrived at in a similar way to that described for the Southern Pacific Building site profile. For granular and stiff to very stiff materials, Ramberg-Osgood

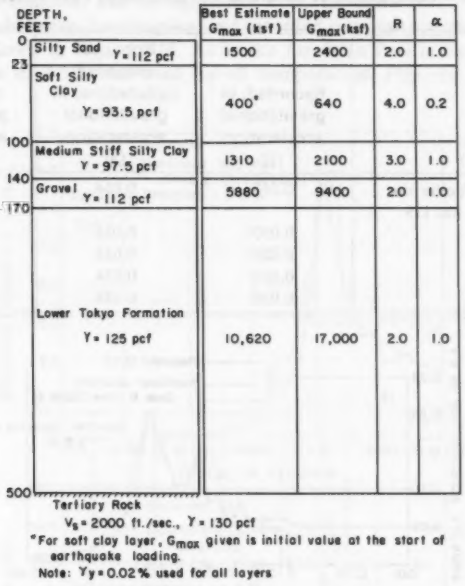

FIG. 10.—Soil Profile and Parameters for Response Analyses, Tokyo Site No. 119

parameters $R = 2$, $\alpha = 1.0$, and $\gamma_y = 0.02\%$ were selected. For the medium stiff clay, $R = 3$, $\alpha = 1$, and $\gamma_y = 0.02\%$ were used. The parameters used for the soft silty clay were the same as for San Francisco Bay Mud in the Southern Pacific Building site analyses. Only the soft silty clay was allowed to degrade. The modulus degradation parameter "t" for the soft layer was assumed to be the same as that used for the San Francisco Bay Mud. A shear viscosity was selected for all layers to provide a damping ratio of 3%. Due to the uncertainties involved in the selection of soil parameters for the analyses, two sets of values of G_{max} were used to define "Best Estimate" and "Upper Bound" stiffnesses, and these are shown in Fig. 10. For SHAKE

TABLE 2.—Station No. 119 Site, Tokyo Cases Studied

Case (1)	Soil stiffness[a] (2)	Input rock motion (3)
A	Best estimate	Site no. 118 (deconvolved)
B	Upper bound	Site no. 118 (deconvolved)
C	Best estimate	Castaic
D	Upper bound	Castaic

[a]See Fig. 10.

TABLE 3.—Comparison of Recorded and Calculated Peak Accelerations

Site (1)	Recorded, in gravitational acceleration (2)	Nonlinear response calculations, in gravitational acceleration (3)	Equivalent linear method, in gravitational acceleration (4)
Southern Pacific site	0.047	0.054	0.062
Tokyo site no. 119			
case A	0.050	0.035	0.050
B	0.050	0.038	0.064
C	0.050	0.024	0.036
D	0.050	0.034	0.050

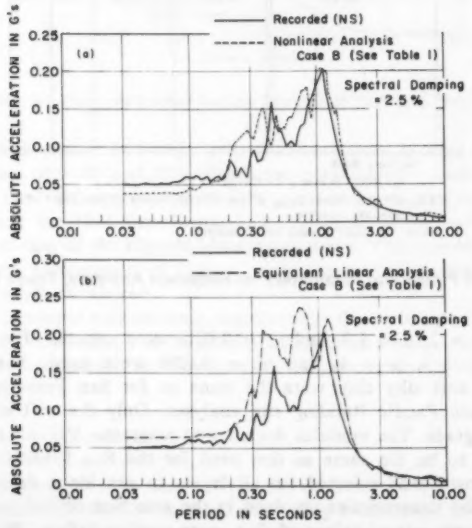

FIG. 11.—Computed and Recorded Acceleration Spectra, Tokyo Site No. 119

runs only the best estimate G_{max} with the modulus and damping curves by Seed and Idriss (19) were used.

Site Response Analyses

The response of the Tokyo Station No. 119 site was calculated using the nonlinear and equivalent linear methods of analysis (programs DCHARM and SHAKE, respectively). Identical profiles and soil properties were used in both sets of calculations. Two input rock motions were assumed to act at the base of the soil profile, and two soil stiffnesses were used for the analyses, as previously described. Therefore, the four cases A–D, described in Table 2, were analyzed using both the nonlinear and the equivalent linear methods.

Comparison between the computed and recorded response spectra near ground surface are shown in Figs. 11–16. As in the Southern Pacific case, a spectral damping value of 2.5% was used for all comparisons. Figs. 11 and 12 show

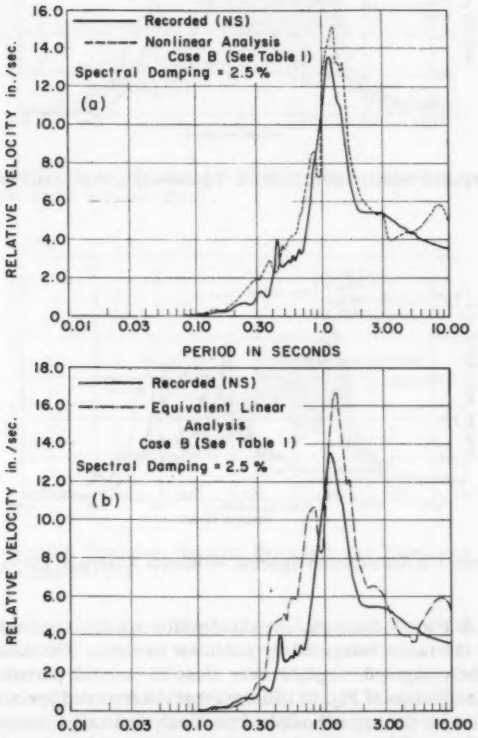

FIG. 12.—Computed and Recorded Velocity Spectra, Tokyo Site No. 119

comparisons between the recorded and computed acceleration and velocity response spectra for Case B. Examination of these spectra indicates again that the nonlinear analysis provides improved agreement with the recorded values. This is true especially for periods less than 0.8 sec, where the equivalent linear method overestimates the response.

Figs. 13 and 14 present the acceleration response spectra for Cases A–D using the equivalent linear and nonlinear analyses, respectively. Fig. 15 compares the ranges of results corresponding to the two analytical models obtained from

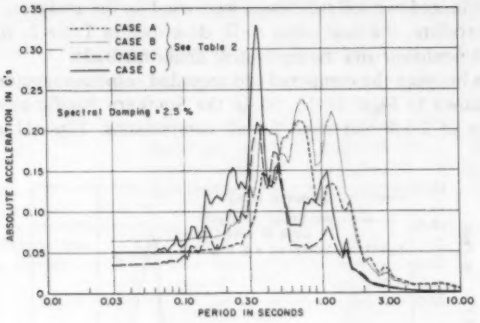

FIG. 13.—Computed Acceleration Spectra, Equivalent Linear Analyses, Tokyo Site No. 119

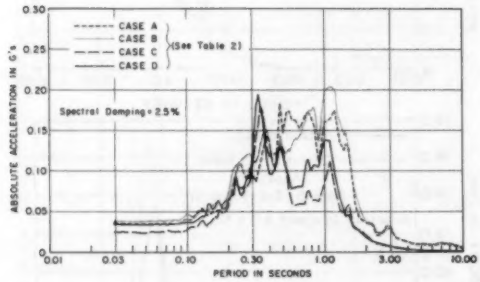

FIG. 14.—Computed Acceleration Spectra, Nonlinear Analyses, Tokyo Site No. 119

Figs. 13 and 14. Fig. 16 compares the acceleration spectrum recorded at Station No. 119 with the range computed by nonlinear analysis. The recorded motion plots inside the computed range or very close to it at all periods longer than 0.2 sec. An examination of Fig. 16 indicates that the recorded spectrum coincides approximately with the upper bound of the analytical range for periods longer than about 0.8 sec. This upper bound is defined by the two analyses using as rock input the deconvolved Station No. 118 motion, while the computed

spectra using Castaic as rock input are significantly lower in that period range (see Fig. 14).

These results indicate that response analyses should preferably be used within the framework of a parametric study. If only one analysis is performed or one rock motion assumed, the calculated results may be unrealistic.

A comparison between recorded spectra at the Station No. 118 stiff site (Fig. 9) and the soft Station No. 119 site (Fig. 16) suggests that the main differences in response attributable to the presence of the soil are in the period range

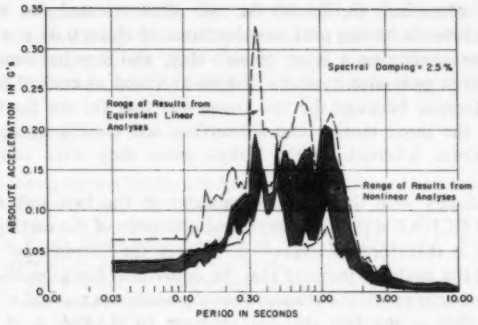

FIG. 15.—Comparison of Acceleration Spectra Computed by Nonlinear and Equivalent Linear Analyses, Tokyo Site No. 119

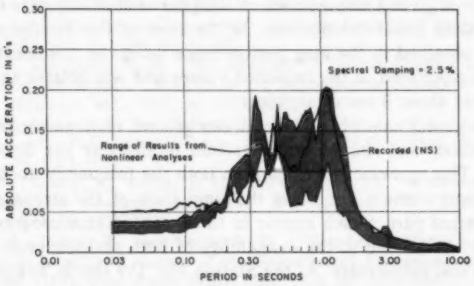

FIG. 16.—Acceleration Response Spectra Recorded and Computed by Nonlinear Analyses, Tokyo Site No. 119

between approx 1 sec and 2 sec. The fundamental period of the soft site, obtained by the four SHAKE runs and including nonlinear effects, was computed to be in the range of 1.2 sec–1.8 sec, with higher values for Cases A and C (Best Estimate stiffness) than for Cases B and D (Upper Bound stiffness). Therefore, as in the Southern Pacific example, the ground motions of the soft site in the 1 sec–2 sec period range seem to have been amplified by the characteristics of the soil profile. It is interesting, however, that the computed

response in this period range seems to be more sensitive to changes in the input motion than to variations in the soil properties. For all four nonlinear analyses, the calculated value of the degradation index in the soft layer at the end of shaking was $\delta \simeq 0.99$, indicating a negligible degradation in modulus values of the soil during this earthquake.

Review and Conclusions

The main purpose of this study was to calibrate a recently developed nonlinear soil response procedure (9,10). At the two sites selected for this purpose, strong-motion records having peak accelerations of about 0.05 *g* were available on soil profiles containing a layer of soft clay, and simultaneous records on rock or stiff sites were also available, which are used as control motions. One important difference between the two cases was that for the Southern Pacific Building site, the input motion and subsurface soil conditions and properties were well known, whereas, at the Tokyo sites, they were estimated using correlations.

The comparisons with the recorded motions at the two soft sites suggest that the use of DCHARM provides improved estimates of the earthquake ground response, and is therefore an improvement over the current use of SHAKE. The results of the analyses indicate that the equivalent linear method computes systematically higher spectral ordinates than the nonlinear method at low periods. This may be due to the fact that, in program DCHARM, $\lambda = 0.03$ for all layers. The shear viscosity may be responsible for overdamping the high frequency response. The analyses conducted as a part of this study show it to be a reasonable value to assume for overall response results. For the long period range, the nonlinear method gives a response which is higher or about equal to that computed by the equivalent linear calculations. In the case of the Southern Pacific site, the response obtained in the long period range using the nonlinear method was reasonable as compared to the recorded values and was related to the response of the soil after about 4 sec of shaking.

A good agreement was obtained between ground response computed by the nonlinear method, and the recorded ground motions at the Southern Pacific Building site. This agreement was good in both the frequency domain (response spectra) and time domain, including the simulation of the strong part followed by the long period part, which appear in the recorded accelerogram. This good agreement may be related to the availability of both realistic rock motion input and measured soil parameters. At the Station No. 119 site in Tokyo, reasonably good agreement was also obtained between computed and recorded ground motions in some of the nonlinear analyses. However, a parametric study, including possible variations in assumed rock motions and soil properties, showed that the quality of the agreement was not as good as for the Southern Pacific Building site. This emphasizes the need for parametric studies when using response calculations in engineering applications.

In all nonlinear analyses performed in this study, there was practically no modulus degradation of the soft clay layer for the level of acceleration and duration of earthquakes studied. This suggests that substantially higher accelerations and durations are needed to cause significant degradation of soft clay deposits. Additional studies are needed to evaluate the levels of earthquake

shaking intensities at which degradation becomes an important factor in the behavior of soft clay sites. It is believed that nonlinear analyses in such cases will yield results closer to reality than the equivalent linear methods.

Acknowledgment

This study, conducted by Woodward-Clyde Consultants (WCC) for the participants—Gulf of Alaska Response Studies Group and monitored by Shell Oil Company, was supported partially from funds provided by the Professional Development Program of WCC. Special thanks are due to Bob Bea for his helpful suggestions during this study; and to R. Murarka and E. Ng for help with computer computations. The writers thank their colleagues at WCC: Y. Moriwaki, M. S. Power, and K. Sadigh for many stimulating talks.

Appendix.—References

1. "Digitized Strong Motion Earthquake Accelerograms in Japan," Association for Science Documents Information, Tokyo, Japan, 1972.
2. Constantopoulos, I. V., Roesset, J. M., and Christian, J. T., "A Comparison of Linear and Exact Non-Linear Analysis of Soil Amplification," *Proceedings, Fifth World Conference on Earthquake Engineering*, 1973.
3. Faccioli, E., and Ramirez, J., "Earthquake Response of Non-Linear Hysteretic Soil," *Journal of Earthquake Engineering and Structural Dynamics*, Vol. 4, 1976, pp. 261–276.
4. Finn, W. D. L., Martin, G. R., and Lee, M. K. W., "Comparison of Dynamic Analyses for Saturated Sands," *Earthquake Engineering and Soil Dynamics*, ASCE, Vol. I, 1978, pp. 472–491.
5. Hudson, D. E., and Housner, G. W., "An Analysis of Strong-Motion Accelerometer Data from the San Francisco Earthquake of March 22, 1957," Bulletin of the Seismological Society of America, Vol. 48, 1958, pp. 253–268.
6. Husid, R. L., "Analysis de Terremotos: Analysis General," *Revista del IDIEM*, Santiago, Chile, Vol. 8, 1969, pp. 21–42.
7. Idriss, I. M., and Seed, H. B., "An Analysis of Ground Motions During the 1957 San Francisco Earthquake," Bulletin of the Seismological Society of America, Vol. 58, No. 6, Baltimore, Md., 1968, pp. 2013–2032.
8. Idriss, I. M., and Seed, H. B., "Seismic Response of Horizontal Soil Layers," *Journal of Soil Mechanics Foundation Division*, ASCE, Vol. 94, No. SM4, Proc. Paper 6043, July, 1968, pp. 1003–1031.
9. Idriss, I. M., Dobry, R., Doyle, E. H., and Singh, R. D., "Behavior of Soft Clays Under Earthquake Loading Conditions," *Proceedings, 1976 Offshore Technology Conference*, Vol. III, OTC 2671, 1976.
10. Idriss, I. M., Dobry, R., and Singh, R. D., "Non-Linear Behavior of Soft Clays During Cyclic Loading," *Journal of the Geotechnical Engineering Division*, ASCE, Vol. 104, No. GT12, Proc. Paper 14265, Dec., 1978, pp. 1427–1447.
11. Joyner, W. B., and Chen, A. T. F., "Calculation of Non-Linear Ground Response in Earthquakes," Bulletin of the Seismological Society of America, Vol. 65, No. 5, Baltimore, Md., 1975, pp. 1315–1336.
12. Lam, I., Tsai Chan-Feng, and Martin, G. R., "Determination of Site Dependent Spectra Using Non-Linear Analysis," *Proceedings of the Second International Conference on Microzonation for Safer Construction—Research and Application*, Vol. II, Nov., 1978.
13. Martin, P. P., "Non-Linear Methods for Dynamic Analysis of Ground Responses," Thesis presented to the University of California, at Berkeley, Calif., in 1975, in partial fulfillment of the requirements of the degree of Doctor of Philosophy.
14. Ohsaki, Y., "Geotechnical Properties of Tokyo Subsoils," *Soil and Foundation*, 1962, Vol. 2, No. 2, Tokyo, Japan, pp. 17–34.
15. Ohsaki, Y., "Effects of Local Soil Conditions Upon Earthquake Damage," *Proceedings*,

Soil Dynamics Specialty Session, Seventh International Conference on Soil Mechanics and Foundation Engineering, 1969, pp. 3–32.
16. Ohsaki, Y., and Hagiwara, T., "On Effects of Soils and Foundations Upon Earthquake Inputs to Buildings," Building Research Institute, *Paper No. 41*, 1970, Tokyo, Japan.
17. Penzien, J., Scheffey, C. F., and Parmelee, R. A., "Seismic Analysis of Bridges on Long Piles," *Journal of the Engineering Mechanics Division*, ASCE, Vol. 90, No. EM3, Proc. Paper 3953, June, 1964, pp. 223–254.
18. Richart, F. E., "Some Effects of Dynamic Soil Properties on Soil-Structure Interaction," *Journal of the Geotechnical Division*, ASCE, Vol. 101, No. GT12, Proc. Paper 11764, Dec., 1975, pp. 1197–1240.
19. Seed, H. B., and Idriss, I. M., "Soil Moduli and Damping Factors for Dynamic Response Analyses," *Report No. EERC 70-10*, Earthquake Engineering Research Center, University of California, Berkeley, Calif., 1970.
20. Seed, H. B., and Idriss, I. M., "Analyses of Ground Motions at Union Bay, Seattle, During Earthquakes and Distant Nuclear Blasts," Bulletin of the Seismological Society of America, Vol. 60, No. 1, Feb., 1970, pp. 125–136.
21. Shima, E., Ohta, Y., Yanagisawa, M., and Kudo, K., "S-Wave Velocities of Subsoil Layers in Tokyo," Bulletin Earthquake Research Institute, Vol. 47, 1979, pp. 819–829.
22. Schnabel, P. B., Lysmer, J., and Seed, H. B., "SHAKE—A Computer Program for Earthqaake Response Analysis of Horizontally Layered Sites," *Report No. EERC 72-12*, Earthquake Engineering Research Center, University of California, Berkeley, Calif., 1972.
23. Steinbrugge, K. V., Bush, V. R., and Zacher, E. G., "Damage to Buildings and Other Structures During the Earthquake of March 22, 1957," San Francisco Earthquakes of March 1957, *Special Report 57*, California Division of Mines, San Francisco, Calif., 1959.
24. Streeter, V. L., Wylie, E. B., and Richart, R. E., "Soil Motion Computations by Characteristic Method," *Journal of the Geotechnical Engineering Division*, ASCE, Vol. 100, No. GT3, Proc. Paper 10410, Mar., 1974, pp. 247–263.
25. Taylor, P. W., and Larkin, T. J., "Seismic Site Response of Non-Linear Soil Media," *Journal of the Geotechnical Engineering Division*, ASCE, Vol. 104, No. GT3, Proc. Paper 13597, Mar., 1978, pp. 369–383.

ANISOTROPIC STRENGTH OF COHESIONLESS SANDS

By Masanobu Oda[1]

INTRODUCTION

Natural in situ soil deposits are neither isotropic nor homogeneous. They often possess layered structures, e.g., alternating layers having quite different particle size distribution, where in each homogeneous layer nonspherical particles have a strong tendency to exist parallel or nearly parallel to the layered structures (3,9,20). The anisotropy and heterogeneity may have considerable influence on the strength and other properties of soils; e.g., on the shear strength of clays (6,22,23), and sands (2,3,11,15,20,21), and on the bearing capacity of sand (12,20,22).

In this paper, the writer reports some results of plane strain tests on samples having layered structures as well as being anisotropic. The results may provide guidance for estimating the internal friction angle of soils with complicated properties.

FABRIC CONCEPT AND TYPES OF ANISOTROPY

Following Brewer (5), by fabric we mean the spatial arrangement of solid particles and the associated voids. Oda (15) suggests that the fabric of sand can be defined by the following two elements: (1) Orientation of nonspherical particles (orientation fabric); and (2) mutual relation of particles (packing).

Orientation Fabric.—This means the parallel alinement of nonspherical particles. The thin section method (11,13,15) and X-ray method (1,2) were proposed in order to obtain quantitative estimates of the orientation fabric.

Packing.—Suppose that a particle G_i has contact with four particles G_1–G_4 at four contacts C_1–C_4. It is reasonable to expect that the relation of G_i with the neighboring particles G_1–G_4 is given by: (1) The four unit vectors, $\mathbf{n}_1$–$\mathbf{n}_4$, which are normal to the contact areas at C_1–C_4; and (2) the number of contacts per particle, m. Since a very large number of particles is involved, we introduce density functions, $E(\mathbf{n})$ and $f(m)$, to define the statistical distribution of $\mathbf{n}$ and m in the considered soil mass. The probability density function, $E(n)$, showing

[1]Visiting Scholar, Dept. of Civ. Engrg., Northwestern Univ., Evanston, Ill. 60201. (Permanent address: Dept. of Foundation Engrg., Saitama Univ., Urawa, Saitama, Japan).

Note.—Discussion open until February 1, 1982. To extend the closing date one month, a written request must be filed with the Manager of Technical and Professional Publications, ASCE. Manuscript was submitted for review for possible publication on November 19, 1980. This paper is part of the Journal of the Geotechnical Engineering Division, Proceedings of the American Society of Civil Engineers, ©ASCE, Vol. 107, No. GT9, September, 1981. ISSN 0093-6405/81/0009-1219/$01.00.

the distribution of the unit normals has been considered by Field (7), Oda (15,16,17), Oda and Konishi (18), and Mulilis, et al. (13). The probability distribution of the number of contacts per particle, $f(m)$, has been used by Smith, et al. (25), Bernal and Mason (4), Field (7), Oda (17), O'Conner, et al. (14), and Grivas (8).

From the detailed observation on the fabric of sand, Oda (15) showed that two types of anisotropy can be distinguished in a uniform sand which is deposited under the action of gravitational force; these are: (1) Anisotropy by the preferential alinement of nonspherical particles parallel to the horizontal; and (2) anisotropy by the concentration of the unit vectors, $\underline{n}$, in the vertical direction. Both types of anisotropy are possible in a naturally deposited sand of nonspherical particles, while in the mass of spheres only anisotropy due to the concentration of $\underline{n}$'s is only possible.

If we include a heterogeneous mass in our consideration, one more type of anisotropy must be added; i.e., (3) anisotropy by the layer structure (3) which is formed by the alternative deposition of different materials such as sand, silt, and clay. Since the three types of anisotropy are usually interrelated in a complicated manner, it is of great importance to consider separately the effect of each anisotropy on the overall mechanical anisotropy of soils.

Test Materials and Preparation of Specimens

Test Materials.—Test materials are Toyoura sand, Tochigi sand, and glass beads, the physical properties of which are summarized in Table 1. [An axial

TABLE 1.—Index Properties of Test Materials

Test materials (1)	Void Ratios		Axial Ratio	Roundness (5)	Grain size, in millimeters (6)
	Maximum (2)	Minimum (3)	R (4)		
Toyoura sand	0.99	0.63	0.61	0.25	0.42 ~ 0.105
Tochigi sand	1.13	0.72	0.71	0.28	0.42 ~ 0.25
Glass beads	0.71	0.55	1.00	1.00	0.42 ~ 0.105

ratio, R, in Table 1 is introduced to identify the average shape of particles (15)]. A sand which is characterized by a high R value, close to unity, consists of particles close to spheres. According to the previous study on natural sands (21), the corresponding R-values range from 0.5–0.7.

Toyoura sand is a uniform sand with a high content of feldspar mineral. This consists of rod-like particles with subangular surfaces. Tochigi sand is also a uniform sand, but consists of quartz grains with subangular surfaces. This is selected as a testing material in order to compare its results with those of Toyoura sand, because both have similar physical properties, but different anisotropy. The sample of glass beads consists of uniform glass balls. This artificial material is used to study the contribution of $\underline{n}$-concentration on the strength anisotropy.

Description of Samples.—Samples used are classified on the basis of their uniformity and anisotropy, as follows.

Uniform-Anisotropic Samples.—Oven dried sands are poured into a sample former through a funnel which is set at 900 mm above the sample former. This pouring method yields a uniform-dense sample with a relative density of 90%. It is clear from the published data (15,21) that the resulting fabric of Toyoura sand, with the void ratio of 0.66–0.67, is highly anisotropic not only by the preferred alinement of rod-like particles parallel to the horizontal but also by the high concentration of $\underline{n}$ to the vertical. The sample of Tochigi sand, with the void ratio of 0.74–0.77, does not show an appreciable parallel

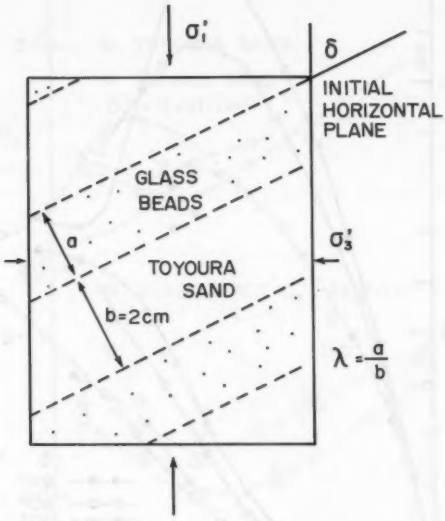

FIG. 1.—Ratio, λ, between Thickness of Toyoura Sand Layer and that of Glass Beads in Layered Samples, and Inclination Angle, δ, of Initial Horizontal Plane to Maximum Principal Axis

alinement of nonspherical particles, but shows the same concentration of $\underline{n}$'s to the vertical as that of Toyoura sand. Kallstenius and Bergau (10) first reported the anisotropic fabric in a random mass of complete spheres, stating that "the mass (of complete spheres) is anisotropic to the extent that the height of each tetrahedron is less than required for isotropy." This finding corresponds to the fabric anisotropy by the concentration of $\underline{n}$'s in a mass of spheres.

In summary, samples made by the pouring procedure are characterized by the uniform-anisotropic fabric irrespective of the shape of particles.

Uniform-pseudoisotropic samples: Oven-dried Toyoura sand is poured to make a sand layer of 10 mm thickness. After each pouring, a hand plunger with 8 mm diam is plunged directly into the sand to destroy the initial anisotropic

arrangement of particles. Each penetration is carefully controlled to be less than 10 mm in depth, and a total of 100 penetrations–200 penetrations is made per each layer. The side wall of the sample former is tapped in order to obtain the same void ratio, ranging from 0.65–0.69, as that of the sample made by the pouring method. This procedure is repeated until the sample formation is completed. We can say, on the basis of the fabric analysis by Oda (15), that it is very difficult to make ideally isotropic samples by destroying the pre-existing

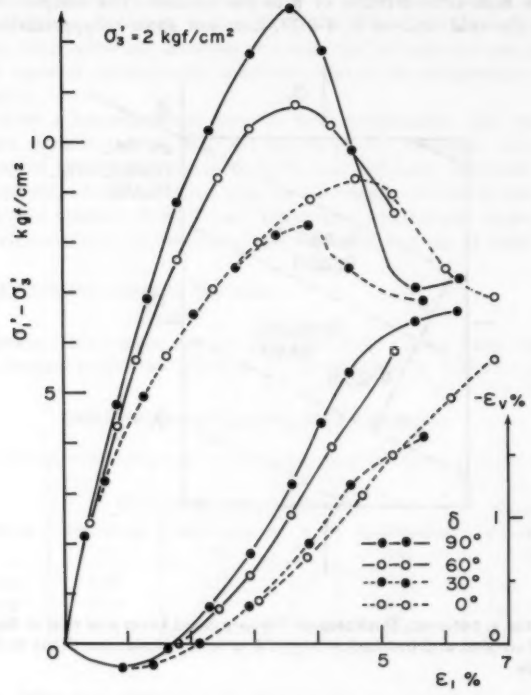

FIG. 2.—Stress-Strain Relations of Uniform-Anisotropic Toyoura Sand (1 kgf/cm² = 98 kN/m²)

anisotropic fabric. The samples, however, are much closer to being isotropic, especially with respect to the distribution of $\underline{n}$'s, than the samples which are prepared by the pouring method.

Layered-Anisotropic Samples.—Toyoura sand and the glass beads are deposited alternately by using the pouring method. Accordingly, the samples in this series consist of successive layers of uniform-anisotropic Toyoura sand and glass beads (Fig. 1). The thickness ratio, λ, defined by

$$\lambda = \frac{\text{thickness of the glass beads}}{\text{thickness of Toyoura sand}}$$

is controlled to be 0.1 or 1.0 by changing the thickness of the glass-bead layers. The thickness of Toyoura sand is kept constant at 20 mm.

Layered-Pseudoisotropic Samples.—These samples consist of successive layers of uniform-pseudoisotropic Toyoura sand and glass beads. Each successive layer is pseudoisotropic because its initial anisotropy is destroyed by the plunging-tapping method. All samples had $\lambda = 1.0$ for this series.

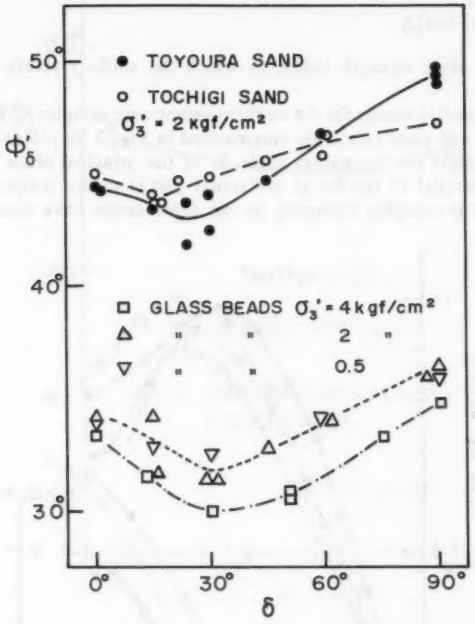

FIG. 3.—Anisotropic Strength Response in Homogeneous-Anisotropic Samples

Plane Strain Test.—Drained plane strain tests are performed on 80 mm × 40.4 mm × 60 mm samples previously mentioned. The direction of the maximum principal stress, σ'_1, is inclined to the principal plane of anisotropy (parallel to the initial horizontal plane) at an angle, δ, in order to determine the effect of the anisotropic fabric and the layer structure on the anisotropic shear strength (Fig. 1). The detailed description for making the samples with different inclination angles, δ, and for experimental procedure has been given by Oda, Koishikawa and Higuchi (21).

The inclination angle, δ, is selected to be 0°, 15°, 22°, 30°, 45°, 60°, 75°,

and 90°, and the minimum principal stress, σ_3', kept constant during each test, is 0.5, 2.0, and 4.0 kgf/cm^2 (1 kgf/cm^2 = 98 kN/m^2).

Experimental Results

Uniform-Anisotropic Samples.—Fig. 2 shows typical stress-strain relations of the uniform-anisotropic Toyoura sand (void ratio being 0.659–0.663).

It is rather difficult to choose a unique coefficient by which the shear strength of anisotropic sand can be fully defined. A friction angle, ϕ_δ', defined by

$$\phi_\delta' = \sin^{-1} \frac{(\sigma_1' - \sigma_3')_f}{(\sigma_1' + \sigma_3')_f}$$

is used as a shear strength index, in which the suffix f refers to the stress at failure.

The experimental results for the uniform-anisotropic samples of Toyoura sand, Tochigi sand and glass beads are summarized in Fig. 3 by plotting the friction angle, ϕ_δ', against the inclination angle, δ, of the principal plane of the fabric anisotropy (parallel to the initial horizontal plane) to the maximum principal stress axis. The samples belonging to the same series have almost the same

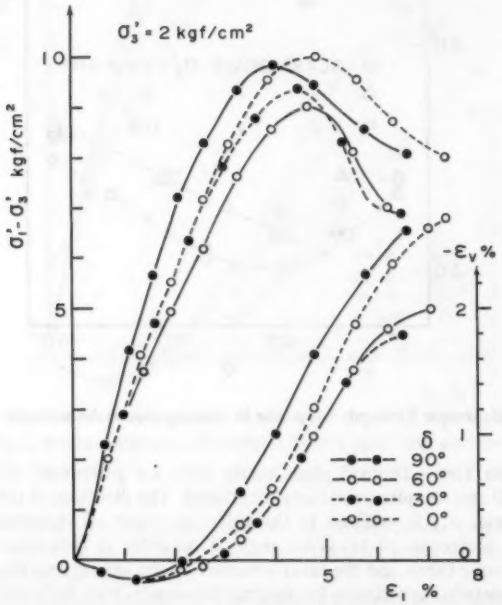

FIG. 4.—Stress-Strain Relations of Uniform-Pseudoisotropic Toyoura Sand (1 kgf/cm^2 = 98 kN/m^2)

void ratio; Toyoura sand = 0.66 ~ 0.67, Tochigi sand = 0.74 ~ 0.77, glass beads = 0.58 ~ 0.61. We can say, therefore, that the corresponding change of ϕ'_δ with respect to the angle δ shows the effect of the anisotropic fabric.

The most important observation in Fig. 3 is the remarkable anisotropic response in the series of the glass beads, consisting of almost complete spheres. The change of ϕ'_δ due to the anisotropy is as much as that of Toyoura sand which consists of rod-like particles with their strong alinement parallel to the initial horizontal plane. Based on the analysis of experimental results from conventional triaxial tests, Oda (15) concluded that the anisotropic distribution of $\underline{n}$ is crucial

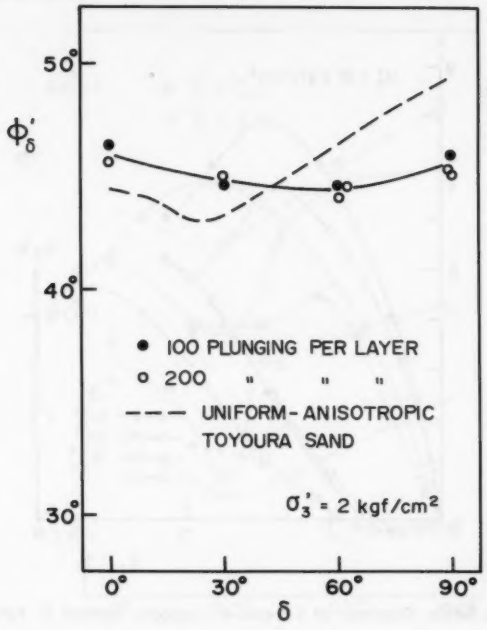

FIG. 5.—Pseudoisotropic Strength Response in Homogeneous-Pseudoisotropic Samples

in the determination of the anisotropic response. This idea seems to be supported by the fact that glass beads with no orientation fabric show an anisotropic shear strength similar to that of Toyoura sand with a strong orientation fabric. At the same time, we can also point out that Toyoura sand with $R = 0.61$ is more anisotropic in its strength behavior than Tochigi sand with $R = 0.71$. To explain the difference from a microscopic point of view, we cannot neglect the effect of the orientation fabric on the anisotropic response. Although the orientation fabric is only one of the influential factors controlling the function $E(\underline{n})$, we can expect a more anisotropic distribution of $E(\underline{n})$ in a mass of

nonspherical particles than in a mass of spherical particles.

Another important observation in Fig. 3 is that each series has a minimum of ϕ_b' at an angle ranging from 15°–30°, depending on the material property. It should be noted that no such minimum was observed with conventional triaxial compression tests (2,3,15). Particles can move easily without any strain confinement in the triaxial compression tests, while movement of particles is restricted in the plane strain tests, because zero strain must be maintained in the direction of the intermediate principal stress, σ_2'. This is also responsible for the fact that the anisotropic response is more pronounced in the plane strain condition. Because of the easy mobility of particles in the triaxial compression test, the

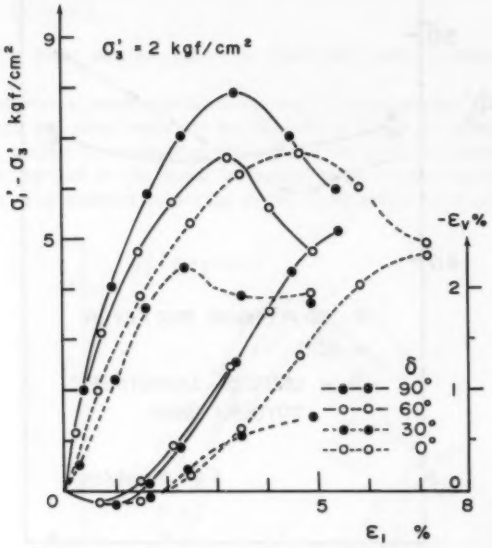

FIG. 6.—Stress-Strain Relations of Layered-Anisotropic Sample (1 kgf/cm² = 98 kN/m²)

initial anisotropy is lost during the course of deformation and a final fabric at failure is attained irrespective of the initial fabric. On the other hand, the initial anisotropic fabric is well preserved at failure in the plane strain tests. This means that the principal plane of the initial anisotropy is a weakness plane so that the sample with $\delta = 15° \sim 30°$ more easily fails along this plane.

Uniform-Pseudoisotropic Samples.—Fig. 4 shows typical stress-strain relations of the pseudoisotropic Toyoura sand, which is plunged 200 times per layer to destroy anisotropic fabric. Samples quoted in Fig. 4 have void ratios ranging from 0.660–0.681, which almost correspond to the void ratio of the uniform-anisotropic Toyoura sand (Fig. 2). It is clear, as Fig. 5 is compared with Fig. 2, that the strength anisotropy is completely destroyed by the plunging procedure.

Results in this series are summarized in Fig. 5. The open circles are obtained from the samples which are plunged 200 times per layer, while the closed circles are obtained from the samples which are plunged 100 times per layer. A broken line in Fig. 4 shows the experimental result of the uniform-anisotropic Toyoura sand.

Since the angle ϕ'_δ depends on the angle δ, with a minimum value at $\delta = 60°$, we cannot say that the sample is ideally isotropic. The plunging-tapping method does not yield an ideally isotropic sample. However, it is clear that the dependence of ϕ'_δ on δ is much less in the uniform-pseudoisotropic sample than in the uniform-anisotropic sample. Note that the mean value of ϕ'_δ of

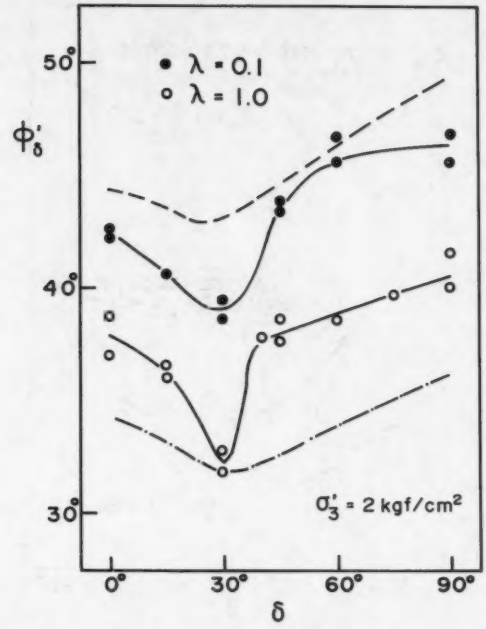

FIG. 7.—Anisotropic Strength Response in Layered-Anisotropic Samples

the uniform-anisotropic Toyoura sand is almost equal to the angle of the uniform-pseudoisotropic Toyoura sand with $\delta = 90°$. This result is suggestive for the determination of the mean value of ϕ'_δ, applicable to an anisotropic sand.

Layered-Anisotropic Samples.—Fig. 6 shows typical stress-strain relations of the layered-anisotropic samples with $\lambda = 1.0$. Fig. 7 also shows the results for the layered-anisotropic samples with $\lambda = 0.1$ and $\lambda = 1.0$, by plotting ϕ'_δ against δ. These data in Fig. 7 are located within the zone bounded by two curves. The upper broken curve corresponds to the result of the uniform-aniso-

tropic Toyoura sand, while the lower broken curve corresponds to the result of the uniform-anisotropic glass beads.

The strength of the layered-anisotropic samples decreases with the increase of the content of glass beads. The decrease, however, seems not to depend linearly on the ratio λ (3). Note that the drastic decrease of ϕ'_δ is clearly observed in the sample with $\delta = 15° \sim 30°$.

Layered-Pseudoisotropic Samples.—Tests are performed only on samples with $\lambda = 1.0$, as shown in Fig. 8. A dotted line in the same figure is the result of the layered-anisotropic samples. The observed anisotropy in the layered-pseudoisotropic samples corresponds to the layer structure, while that in the layered-

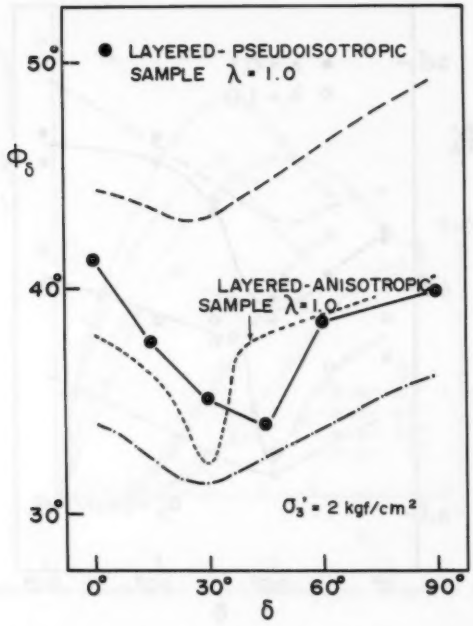

FIG. 8.—Anisotropic Strength Response in Layered-Pseudoisotropic Samples

anisotropic samples corresponds to the combined effect of the fabric anisotropy in each layer and the layer structure. Both results, however, are similar, except each corresponding minimum is at a different value of δ. The similarity of the results seems to support the idea that the layer structure is a predominant factor for controlling the strength anisotropy.

Conclusions

Natural sand deposits are generally anisotropic as well as heterogeneous.

In order to provide insight regarding fundamental factors affecting the strength behavior of such complex soils, we have performed plane strain tests on uniform-anisotropic, uniform-pseudoisotropic, layered-anisotropic and layered-pseudoisotropic samples. The experimental results support the following conclusions:

1. We can distinguish three forms of fabric anisotropy; e.g., orientation, packing, and layering. Fabric anisotropy due to packing is crucial in the determination of strength anisotropy of homogeneous sand. Fabric anisotropy due to parallel alinement of particles is only one of the influential factors controlling the packing. Layering can be another predominant factor in the determination of strength anisotropy.
2. We should expect anisotropic strength response even in a uniform mass composed of spheres. This is caused by the anisotropic distribution of contact normals which can take place even in a random mass of spheres.
3. It is rather difficult to form an isotropic sample of sand. It is therefore necessary to always think that an assembly of particles is generally anisotropic.
4. Tests on pseudoisotropic samples whose anisotropic fabric is destroyed by applying a plunger give reasonable estimates of the mean strength for anisotropic sands. If we want to calculate the bearing capacity of uniform-anisotropic foundations in the conventional way (26), e.g., testing on the pseudoisotropic sample may be advisable for obtaining a reasonable estimate of the internal friction angle.

Acknowledgments

This work has been supported by United States Air Force Office of Scientific Research, Grant No. AFOSR-80-0017 to Northwestern University. The writer wishes to express his sincere gratitude to S. Nemat-Nasser of Northwestern University for his kind advice and his critical reading of this manuscript.

Appendix I.—References

1. Arthur, J. R. F., and Dunstan, T., "Radiography Measurement of Particle Packing," *Nature*, Vol. 223, London, England, 1964, pp. 464–468.
2. Arthur, J. R. F., and Menzies, B. K., "Inherent Anisotropy in a Sand," *Géotechnique*, Vol. 22, No. 1, London, England, 1972, pp. 115–128.
3. Arthur, J. R. F., and Phillips, A. B., "Homogeneous and Layered Sand in Triaxial Compression," *Géotechnique*, Vol. 25, No. 4, London, England, 1975, pp. 799–815.
4. Bernal, J. D., and Mason, J., "Co-ordination of Randomly Packed Spheres," *Nature*, Vol. 188, London, England, 1960, pp. 910–911.
5. Brewer, R., "Fabric and Mineral Analysis of Soils," John Wiley and Sons, Inc., New York, N.Y., 1964.
6. Duncan, J. M., and Seed, H. B., "Anisotropy and Stress Reorientation in Clay," *Journal of the Soil Mechanics and Foundations Division*, ASCE, Vol. 92, No. SM5, Proc. Paper 14903, 1966, pp. 21–50.
7. Field, W. G., "Towards the Statistical Definition of a Granular Mass," *Proceedings of 4th A. and New Zealand Conference on Soil Mechanics*, 1963, pp. 143–148.
8. Grivas, D. A., and Harr, M. E., "Particle Contacts in Discrete Materials," *Journal of the Geotechnical Engineering Division*, ASCE, Vol. 106, No. GT5, Proc. Paper 15432, 1980, pp. 559–564.
9. Johansson, G., "Structural Studies of Sedimentary Deposits," *Geologiska Föreningens i Stockholm Förhandingar*, Vol. 87, Stockholm, Sweden, 1965, pp. 3–61.

10. Kallstenius, T., and Bergau, W., "Research on the Texture of Granular Massess," *Proceedings of 5th International Conference on Soil Mechanics and Foundation Engineering*, Vol. 1, 1961, pp. 165–170.
11. Mahmood, A., and Mitchell, J. K., "Fabric-Property Relationship in Fine Granular Materials," *Clays and Clay Minerals*, Vol. 22, No. 516, 1974, pp. 397–408.
12. Meyerhof, G. G., "Bearing Capacity of Anisotropic Cohesionless Soils," *Canadian Geotechnical Journal*, Vol. 15, No. 4, Toronto, Canada, 1978, pp. 592–595.
13. Mulilis, J. P., Seed, H. B., Chan, C. K., Mitchell, J. K., and Arulanandan, K., "Effects of Sample Preparation on Sand Liquefaction," *Journal of the Geotechnical Engineering Division*, ASCE, Vol. 103, No. GT2, Proc. Paper 12760, 1977, pp. 91–106.
14. O'Conner, K. M., Krizek, J. R., and Atmatzidis, D. K., "Microcharacteristics of Chemically Stabilized Granular Materials," *Journal of the Geotechnical Engineering Division*, ASCE, Vol. 104, No. GT7, Proc. Paper 13894, 1978, pp. 939–952.
15. Oda, M., "Initial Fabrics and Their Relations to Mechanical Properties of Granular Material," *Soils and Foundations*, JSSMFE, Vol. 12, No. 1, Tokyo, Japan, 1972a, pp. 17–36.
16. Oda, M., "The Mechanism of Fabric Changes during Compressional Deformation of Sand," *Soils and Foundations*, JSSMFE, Vol. 12, No. 2, Tokyo, Japan, 1972b, pp. 1–18.
17. Oda, M., "Deformation Mechanism of Sand in Triaxial Compression Tests," *Soils and Foundations*, JSSMFE, Vol. 12, No. 4, Tokyo, Japan, 1972c, pp. 45–63.
18. Oda, M., and Konishi, J., "Microscopic Deformation Mechanism of Granular Material in Simple Shear," *Soils and Foundations*, JSSMFE, Vol. 14, No. 4, Tokyo, Japan, 1974, pp. 1–14.
19. Oda, M. "Co-Ordination Number and Its Relation to Shear Strength of Granular Material," *Soils and Foundations*, JSSMFE, Vol. 17, No. 2, Tokyo, Japan, 1977, pp. 29–42.
20. Oda, M., and Koishikawa, I., "Anisotropic Fabric of Sands," *Proceedings of International Conference on Soil Mechanics and Foundation Engineering*, Vol. 1, 1977, pp. 235–238.
21. Oda, M., Koishikawa, I., and Higuchi, T., "Experimental Study of Anisotropic Shear Strength of Sand by Plane Strain Test," *Soils and Foundations*, JSSMFE, Vol. 18, No. 1, Tokyo, Japan, 1978, pp. 25–38.
22. Oda, M., and Koishikawa, I., "Effect of Strength Anisotropy on Bearing Capacity of Shallow Footing in a Dense Sand," *Soils and Foundations*, JSSMFE, Vol. 19, No. 3, Tokyo, Japan, 1979, pp. 15–28.
23. Saada, A. S., and Ou, C. D., "Stress-Strain Relations and Failure of Anisotropic Clays," *Journal of the Soil Mechanics and Foundation Division*, ASCE, Vol. 99, No. SM12, Proc. Paper 10225, 1973, pp. 1091–1111.
24. Saada, A. S., and Bianchini, G. F., "Strength of One-Dimensionally Consolidated Clays," *Journal of the Geotechnical Engineering Division*, ASCE, Vol. 101, No. GT11, Proc. Paper 12507, 1975, pp. 1151–1164.
25. Smith, W. O., Foote, P. D., and Busang, P. F., "Packing of Homogeneous Spheres," *Physical Review*, Vol. 34, New York, N.Y., pp. 1271–1274.
26. Terzaghi, K., *Theoretical Soil Mechanics*, John Wiley and Sons, Inc., New York, N.Y., 1943.

Appendix II.—Notation

The following symbols are used in this paper:

e = void ratio;
$E(\underline{n})$ = probability density of contact normal $\underline{n}$;
$\underline{n}$ = unit vector normal to contact;
R = axial ratio showing particle shape;
δ = inclination angle of σ_1' to initial horizontal plane;
ϵ_1 = maximum principal strain;

ϵ_v = volumetric strain;
λ = thickness ratio;
σ_1' = maximum principal stress (in effective);
σ_2' = intermediate principal stress (in effective);
σ_3' = minimum principal stress (in effective); and
σ_δ' = friction angle defined by $\sin^{-1} \sigma_1 - \sigma_3/(\sigma_1 + \sigma_3)$.

GEOTEXTILE-REINFORCED UNPAVED ROAD DESIGN[a]

By Jean-Pierre Giroud,[1] M. ASCE, and Laure Noiray[2]

INTRODUCTION

Geotextiles is the name now universally adopted for fabrics used in geotechnical engineering. They have been used extensively in unpaved roads. Geotextiles are placed between the aggregate layer and the subgrade soil (Fig. 1) to perform several functions: (1) Separation; (2) filtration; (3) drainage; and (4) reinforcement.

By providing reinforcement, geotextiles improve the performance of unpaved roads: for a given thickness of aggregate layer, the traffic can be increased or, in other words, for the same traffic, the thickness of aggregate layer can be reduced (in comparison with the required thickness when no geotextile is used).

This improvement of performance has been recognized by users in the field, but design procedures are lacking. The study presented in this paper addresses this lack by developing a method which enables the engineer to calculate the required thickness of aggregate layer and make the proper selection of the geotextile to be used. The results are presented in the form of charts established using a combination of: (1) Formulas relating aggregate thickness and traffic for unpaved roads without geotextile; and (2) a quasi-static analysis comparing unpaved roads behavior with and without geotextile.

The readers and possible users of these charts must recognize that the present study applies only to purely cohesive subgrade soils and is mostly applicable to roads subjected to light to medium traffic (1–10,000 truck passages over the lifetime of the road).

GENERAL DEFINITIONS

Geometry of Unpaved Road.—The cross section of an unpaved road is defined in Fig. 1, in which: h_0 = thickness of aggregate layer when there is no geotextile

[a]Presented at the April 14–18, 1980, ASCE Convention and Exposition, held at Portland, Oreg. (Preprint 80-177).

[1]Woodward-Clyde Consultant, Geotextiles and Geomembranes Group, 11 East Adams Street, Suite 1500, Chicago, Ill. 60603.

[2]Woodward-Clyde Consultant, Geotextiles and Geomembranes Group, 11 East Adams Street, Suite 1500, Chicago, Ill. 60603.

Note.—Discussion open until February 1, 1982. To extend the closing date one month, a written request must be filed with the Manager of Technical and Professional Publications, ASCE. Manuscript was submitted for review for possible publication on April 3, 1980. This paper is part of the Journal of the Geotechnical Engineering Division, Proceedings of the American Society of Civil Engineers, ©ASCE, Vol. 107, No. GT9, September, 1981. ISSN 0093-6405/81/0009-1233/$01.00.

(in meters); h = thickness of aggregate layer when there is a geotextile (in meters); and $\Delta h = h_0 - h$ = reduction of aggregate thickness resulting from the use of a geotextile (in meters).

The subgrade soil is assumed to be homogeneous, at least over a thickness, H_{min}, sufficient for the development of a plastic zone (see later, Eq. 19).

Definition of Axle Load and Contact Area.—Any vehicle load can be replaced by an equivalent single axle load using the procedure described in Appendix I. Therefore, the analysis presented in this paper refers to a single axle. The geometry of this axle is depicted in Fig. 2(*a*) in which e = distance between the midpoints of the two sets of wheels (in meters). Dual wheels are considered because they are more common than single wheels for trucks using unpaved roads.

The axle load, P, is considered to be evenly distributed between the four wheels:

$$P = 4A_c p_c \quad \ldots \ldots \ldots

The relationship between equivalent contact pressure, p_{ec}, and tire inflation pressure, p_c, is deduced from Eq. 1, 2, and 3:

$$p_{ec} = \frac{p_c}{\sqrt{2}} \quad \ldots \ldots \ldots

Properties of Geotextile.—The geotextile mechanical properties relevant to this study are best described by the geotextile tension-elongation behavior in a biaxial tensile test, where lateral deformation of the geotextile sample is prevented. Tension (in Newtons per meter) is defined as tensile force (in Newtons) per unit width (in meters).

Fig. 3 presents a typical tension-elongation curve and shows the definition of the secant modulus, K. In the following, only the secant modulus in the transverse direction of the road is considered. Typical values of K for elongations between 0% and 20% are: 1 kN/m–5 kN/m for plain rubber or plastic sheets; 20 kN/m–500 kN/m for nonwoven geotextiles; and 50 kNm–5,000 kN/m for woven geotextiles.

The geotextile elongation associated with road deflection must be smaller than the elongation at failure ϵ_F.

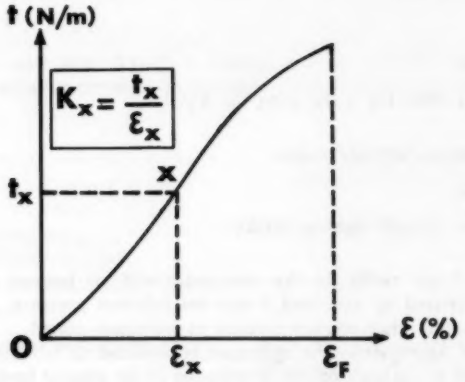

FIG. 3.—Typical Tension-Elongation Curve of Geotextile (ϵ_F = Elongation at Failure; ϵ_x = Elongation at Point x; t_x = Tension at Point x; and K_x = Secant Modulus at Point x)

For a woven geotextile, the tension-elongation curves obtained from a uniaxial test (as it is usually performed in the textile industry) and a biaxial test are not very different. For a nonwoven geotextile, the difference is usually important and the biaxial test is strongly recommended.

In addition to tensile behavior, it is necessary to address the friction characteristics of the geotextile. It is beyond the scope of this paper to elaborate on this subject. This study assumes that the geotextile is rough enough to prevent failure of the aggregate layer by sliding along the geotextile surface.

General Assumptions for Quasi-Static Analysis

Mechanisms of Failure of an Unpaved Road.—The failure of an unpaved road can occur at three different locations: (1) Aggregate layer; (2) foundation soil; and (3) geotextile (if any). The present study does not consider a failure of

the aggregate layer. In other words, it is assumed that: (1) The friction coefficient of the aggregate layer is large enough to ensure the mechanical stability of the layer; and (2) the friction angle of the geotextile in contact with the aggregate layer under the wheels is large enough to prevent sliding of the aggregate layer on the geotextile.

Basically, this study evaluates the risk of failure of the foundation soil and of the geotextile.

Load Distribution by Aggregate Layer.—The aggregate layer is assumed to provide a pyramidal distribution with depth of the pressure, p_{cc}, applied on its surface (Fig. 4).

Therefore:

$$p_{cc}LB = (B + 2h_0 \tan \alpha_0)(L + 2h_0 \tan \alpha_0)(p_0 - \gamma h_0) \quad \text{without geotextile} \quad (11)$$

$$p_{cc}LB = (B + 2h \tan \alpha)(L + 2h \tan \alpha)(p - \gamma h) \quad \text{with geotextile} \quad (12)$$

in which: γ = weight per unit volume of the aggregate (in Newtons per cubic meter); p_0 = pressure at the base of aggregate layer when no geotextile is

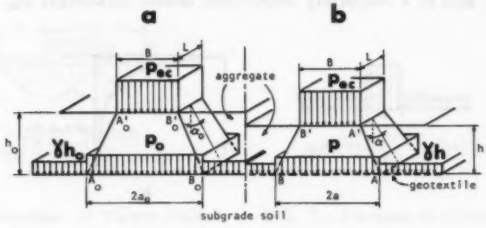

FIG. 4.—Load Distribution by Aggregate Layer: (*a*) Case Without Geotextile; and (*b*) Case with Geotextile

used (in Pascals); p = pressure at the base of aggregate layer when a geotextile is used (in Pascals); and α_0 and α = angles of load distribution pyramid (in degrees) (see Fig. 4).

From Eqs. 3, 11, and 12:

$$p_0 = \frac{P}{2(B + 2h_0 \tan \alpha_0)(L + 2h_0 \tan \alpha_0)} + \gamma h_0 \quad \text{without geotextile} \quad (13)$$

$$p = \frac{P}{2(B + 2h \tan \alpha)(L + 2h \tan \alpha)} + \gamma h \quad \text{with geotextile} \quad (14)$$

There is some uncertainty about the value to be adopted for α_0 and α. However, different approaches lead to similar values: (1) An experimental approach consists of considering the shape of the deformed aggregate layer after tests (2,4); this suggests approximate values of tan α_0 and tan α between 0.5 and 0.7; and (2) a theoretical approach consists of assuming that $\alpha_0 = \alpha = \pi/4 - \phi/2$, classical value for the inclination of the shear planes if the aggregate layer were punched; for ϕ between 25° and 45°, this yields values of tan α_0 and tan α between 0.47 and 0.64.

Preliminary calculations have shown that the value of the calculated aggregate thickness is not significantly influenced by α_0 and α, as long as tan α_0 and tan α are between 0.5 and 0.7. Therefore, tan α_0 = tan α = 0.6 has been assumed in all subsequent calculations.

Bidimensional Approach.—The analysis will be bidimensional in a vertical cross section of the road. This is based upon the following two points: (1) The wheels are assumed to travel always along the road in the same track, so that every cross section of the road receives the same amount of loading and deforms in the same way; thus, there is no residual deformation in the direction of the road and every cross section has the same mechanical behavior; and (2) it is a classical practice in soil mechanics to evaluate the limit equilibrium of a soil using a bidimensional analysis; first, because the tridimensional limit equilibrium of a soil is still not well known; secondly, because according to studies on this subject, the difference between bearing capacities deduced from bidimensional and tridimensional equilibria of a frictionless soil is not important.

Elastic and Plastic Behaviors of Soil under Loading.—Consider a frictionless soil subjected to a uniformly distributed pressure, q, over a limited portion of its surface and to a uniformly distributed lateral surcharge, q_{lat} [Fig. 5(*a*)].

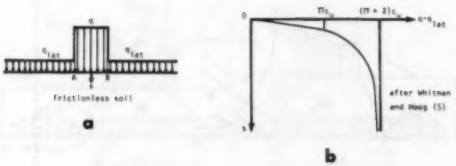

FIG. 5.—Elastic and Plastic Behaviors of Soil under Loading: (*a*) Loading Pattern; and (*b*) Settlement, *s*, of Center of AB Versus Applied Pressure

Classical bidimensional calculations based on theory of elasticity lead to the value q_e of q which induces stresses in the soil corresponding to the elastic limit of the soil:

$$q_e = \pi c_u + q_{lat} \quad \ldots \quad (15)$$

in which: q_e = elastic bearing capacity of the soil (in Pascals); and c_u = undrained cohesion of the frictionless soil (in Pascals).

Similar calculations using theory of plasticity lead to q_{ult}, maximum value of q:

$$q_{ult} = (\pi + 2)c_u + q_{lat} \quad \ldots \quad (16)$$

in which: q_{ult} = ultimate bearing capacity of the soil (in Pascals).

Fig. 5(*b*) shows the settlement, s, occurring at the center of the loaded portion of the soil surface as a function of the difference, $q - q_{lat}$. This settlement is small when the value of q is smaller than q_e and large when the value of q is larger than q_e.

Fig. 6(*a*) shows the development of plastic zones in a frictionless incompressible soil under a load equal to the ultimate bearing capacity of the soil and applied over a width 2(*a*).

The depth of the plastic zones is given by:

$$H_p = a\sqrt{2} \quad \ldots \quad (17)$$

Theory of plasticity will be used later to describe the behavior of the subgrade soil when a geotextile is used. In this case, according to Fig. 4(*b*):

$$2a = B + 2h \tan \alpha \quad \ldots \quad (18)$$

According to Eqs. 17 and 18, the minimum value for the subgrade soil thickness, to ensure the validity of subsequent calculations based upon theory of plasticity, is:

$$H_{min} = \frac{B + 2h \tan \alpha}{\sqrt{2}} \quad \ldots \quad (19)$$

The width of plastic zones, on either sides of the loaded area, is equal to the width of the loaded area. Therefore, if two loads are at a distance smaller than $2a$ [Fig. 6(*b*)], the heave of the soil between the two loads is restricted and more soil moves outwards than inwards. This consideration is important

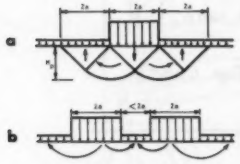

FIG. 6.—Mechanism of Plastic Failure of Frictionless Soil: (*a*) One Load; and (*b*) Two Loads

FIG. 7.—Increase of Lateral Surcharge by Heave of Soil

as it will be shown later. The width of plastic zones also governs the required lateral extent of the geotextile under the road shoulders.

In conclusion, the soil settles under the load (Fig. 5) and heaves laterally (Fig. 6). This phenomenon as a whole is called deflection of the soil surface. A more rigourous analysis would consider that heave of the soil increases the lateral surcharge (Fig. 7). In fact, it has been checked that such an increase does not have a significant effect on the results of the subsequent analyses. Therefore, it will be neglected.

Unpaved Roads without Geotextile

Quasi-Static Analysis.—The aforementioned results concerning theories of elasticity and plasticity can be used in the case of a loaded aggregate layer. When there is no geotextile [Fig. (4*a*)], the load applied on the subgrade soil by a dual wheel and by the weight of aggregate layer is equivalent to a uniform pressure, p_0, over a width ($B + 2h_0 \tan \alpha_0$), and to a uniform lateral surcharge, γh_0, elsewhere (with γ = weight per unit volume of aggregate, in Newtons per cubic meters).

If p_0 exceeds the elastic bearing capacity of the subgrade soil, the deflection will be large and complete failure of the road will occur after a few passages of the dual wheel. Consequently, the design of an unpaved road without geotextile must consider a maximum pressure on the subgrade soil equal to the elastic bearing capacity. Therefore, according to Eq. 15:

$$p_0 = \pi c_u + \gamma h_0 \quad \ldots \ldots \ldots \ldots \ldots \ldots \ldots \ldots \ldots \ldots \ldots \ldots \ldots \quad (20)$$

It will be seen later that, in the case of a geotextile-reinforced, unpaved road, because of a different kinematics, the maximum pressure on the subgrade soil can be practically equal to the ultimate bearing capacity.

From Eqs. 13 and 20:

$$\frac{P}{2(B + 2h_0 \tan \alpha_0)(L + 2h_0 \tan \alpha_0)} = \pi c_u \quad \ldots \ldots \ldots \ldots \ldots \ldots \quad (21)$$

Therefore, for on-highway trucks, according to Eqs. 5 and 7:

$$c_u = \frac{P}{2\pi \left(\sqrt{\frac{P}{p_c}} + 2h_0 \tan \alpha_0 \right) \left(\sqrt{\frac{P}{2p_c}} + 2h_0 \tan \alpha_0 \right)} \quad \ldots \ldots \ldots \quad (22)$$

Similarly, for off-highway trucks, according to Eqs. 6 and 8:

$$c_u = \frac{P}{2\pi \left(\sqrt{P \frac{\sqrt{2}}{p_c}} + 2h_0 \tan \alpha_0 \right) \left(\sqrt{\frac{P}{2p_c\sqrt{2}}} + 2h_0 \tan \alpha_0 \right)} \quad \ldots \ldots \quad (23)$$

in which: c_u = cohesion of subgrade soil (in Pascals); P = axle load (in Newtons); p_c = tire inflation pressure (in Pascals); h_0 = thickness of aggregate layer (in meters); and α_0 = angle of load distribution pyramide (in degrees) (Note: tan $\alpha_0 = 0.6$, as previously stated).

The chart presented in Fig. 8 has been established using Eqs. 22 and 23. This chart allows determination of aggregate thickness, h_0 when subgrade soil cohesion, c_u, and axle load P are known. Design engineers should bear in mind that the use of this chart is restricted to very light traffic (say 1–20 passages) because it has been established using a quasi-static analysis. A procedure to take heavier traffic into account is presented in the next section.

Influence of Traffic.—An extensive test program on unpaved roads (without geotextile) has been conducted by the Corps of Engineers (1). Failure criterion was a rut depth of 0.075 m. From the test results, Webster and Alford established a chart (3) giving the thickness of aggregate layer as a function of number of passages and CBR of subgrade soil, for a standard axle load, P_s, of 80 kN. The following formula has been found in good agreement with Webster and Alford's chart:

$$h_0' = \frac{0.19 \log N_s}{(\text{CBR})^{0.63}} \quad \ldots \ldots \ldots \ldots \ldots \ldots \ldots \ldots \ldots \ldots \ldots \ldots \quad (24)$$

in which: h_0' = thickness of aggregate layer (in meters); N_s = number of passages

of standard axle (load P_s = 80 kN); and CBR = California Bearing Ratio of subgrade soil. The use of Eq. 24 is restricted to standard axle load and 0.075 m rut depth. Eq. 24 appears to be in better agreement with Webster and Alford's chart than other proposed formulas giving h_0' as a function of log (CBR).

To extend Eq. 24 to other axle loads, the following equation is proposed:

$$\frac{N_s}{N_i} = \left(\frac{P_i}{P_s}\right)^{3.95} \quad \ldots\ldots\ldots\

has been established by extrapolation and should not be used when the number of passages exceeds 10,000.

Fig. 9 presents values obtained from Eq. 26 in the case of standard axle load and 0.3 m rut depth. Similar charts have been established for several values of axle load P and rut depth, r.

Fig. 9 shows that the curves h_0 versus c_u obtained from quasi-static analysis (Eq. 22) correspond to a number of passages on the order of magnitude of 100. With an allowable rut depth of 0.075 m, the curves h_0 versus c_u would correspond to a number of passages on the order of magnitude of 10. This

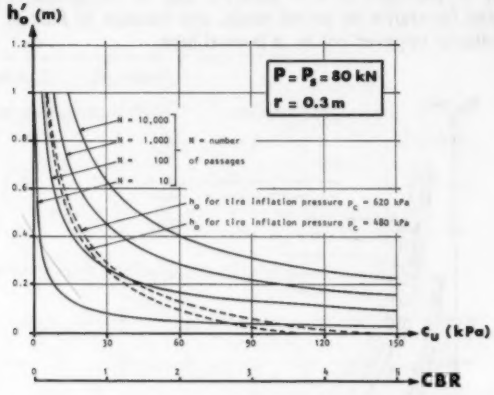

FIG. 9.—Aggregate Thickness h'_0 Versus Subgrade Soil Cohesion (Case without Geotextile when Traffic is Taken into Account) (Curves h_0 Versus c_u are Extracted from Fig. 8)

comparison shows that a quasi-static analysis is well suited to a light traffic, which seems reasonable.

Quasi-Static Analysis of Unpaved Roads with Geotextile

Kinematics.—As previously mentioned, the subgrade soil is incompressible and settlement under the wheels causes heave between and beyond the wheels (Fig. 10). Therefore, the geotextile exhibits a wavy shape; consequently, it is stretched.

When a stretched flexible material has a curved shape, pressure against its concave face is higher than pressure against its convex face. This is known as "membrane effect." Therefore: (1) Between the wheels (BB in Fig. 10) and also beyond the wheels (AC in Fig. 10), although to a lesser extent, the pressure applied by the geotextile on the subgrade soil is higher than the pressure applied by the aggregate layer on the geotextile; and (2) under the wheels (AB in Fig. 10), the pressure applied by the geotextile on the subgrade soil is smaller than the pressure applied by the wheels plus the aggregate layer on the geotextile.

As a conclusion, the geotextile provides two beneficial effects: (1) Confinement

of the subgrade soil between and beyond the wheels; and (2) reduction of the pressure applied by the wheels on the subgrade soil. These two effects will be evaluated in the following sections.

Subgrade Soil Equilibrium.—As shown in Fig. 4(*b*), the pressure applied by the wheels and aggregate layer on the portion AB of the geotextile is p, given by Eq. 14. The pressure applied on the subgrade soil by the portion AB of the geotextile is:

$$p^* = p - p_g \quad \ldots \quad (27)$$

in which: p_g = reduction of pressure resulting from the use of a geotextile (as explained previously) in Pascals; p_g will be evaluated in the next sections.

Because the subgrade soil confinement provided by the geotextile helps keep the deflection small for all applied pressures less than the ultimate bearing capacity, the pressure p^* can be as large as the ultimate bearing capacity of the subgrade soil, given by Eq. 16, in which q_{lat} is replaced by γh:

$$p^* = (\pi + 2)c_u + \gamma h \quad \ldots \quad (28)$$

A comparison between Eqs. 20 and 28 outlines the benefit resulting from subgrade soil confinement by a geotextile; the term πc_u in Eq. 20 referring

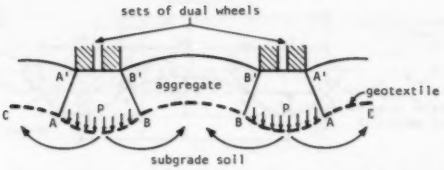

FIG. 10.—Kinematics of Unpaved Road with Geotextile

to elastic behavior is replaced in Eq. 28 by the term $(\pi + 2)c_u$ referring to plastic behavior.

Eqs. 27 and 28 yield:

$$p - p_g = (\pi + 2)c_u + \gamma h \quad \ldots \quad (29)$$

As previously stated, p_g is a function of the tension of the geotextile, which depends on its elongation, the elongation itself depending on its shape. Therefore, prior to the determination of p_g, the shape and the resulting elongation of the geotextile must be assessed; this is done in the following two sections.

Shape of Deformed Geotextile.—The wavy shape of the deformed geotextile results from the incompressibility of the subgrade soil. Therefore, the volume of subgrade soil displaced downwards by settlement must be equal to the volume of soil displaced upwards by heave. The shape of the deformed geotextile is assumed to consist of portions of parabolas connected at A and B, points located on the initial plane of the geotextile (Fig. 11). It is also assumed that the thickness of aggregate layer is not significantly affected by subgrade soil deflection. This assumption is based on observations from full scale tests (4). Therefore: (1)

the total deflection of the geotextile is equal to rut depth; and (2) comparison of Figs. 2, 4, and 11 gives:

$$2a = B + 2h \tan \alpha \quad \ldots \quad (30)$$

$$2a' = e - B - 2h \tan \alpha \quad \ldots \quad (31)$$

Two cases must be considered, depending upon which parabola is the wider.

The first case arises when the central parabola is the wider ($a' > a$, thus, according to Eqs. 30 and 31: $4h \tan \alpha < e - 2B$). One half of the soil displaced downwards by settlement contributes to heave between the wheels, while the other half contributes to heave beyond the wheels [Fig. 12(*a*)]. The relationship between settlement, s, and rut depth, r, which characterizes the shape of the geotextile is determined by writing that areas A and A' are equal [Fig. 12(*a*)]:

$$A = \frac{2as}{3} = 2a' \frac{(r - s)}{3} = A' \quad \ldots \quad (32)$$

$$\text{Therefore:} \quad s = \frac{ra'}{a + a'} \quad \ldots \quad (33)$$

The second case arises when the parabolas under the wheels are the wider ($a > a'$). Less than one half of the soil displaced downwards by settlement

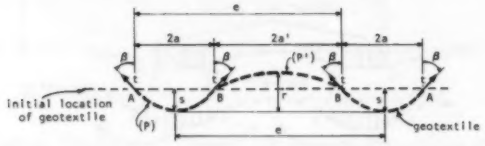

FIG. 11.—Shape of Deformed Geotextile

contributes to heave between the wheels [Fig. 12(*b*)]. The width of area A'' is assumed to be equal to half the width of (P') and the relationship between s and r is determined by writing that areas A' and A'' are equal [Fig. 12(*b*)]. After calculations:

$$s = \frac{2ra^2}{2a^2 + 3a\,a' - a'^2} \quad \ldots \quad (34)$$

Note that Eqs. 33 and 34 lead to the same value, $s = r/2$, when $a = a'$.

In both Eqs. 33 and 34, a and a' could be replaced by their expressions from Eqs. 30 and 31 in order to obtain the relationship between s and r as a function of B, e, h, and α.

Elongation of Geotextile.—The reduction of pressure, p_g, is due to the tension of geotextile in parabola (P) (Fig. 12). Since tension is a function of elongation, it is necessary to determine first the elongation, ϵ, of the geotextile in (P). Again, the same two cases must be considered.

If $a' > a$ [Fig. 12(*a*)], Eq. 33 leads to $s/a > (r - s)/a'$. Therefore, the elongation, and the tension of the geotextile tend to be larger in (P) than in

(P'). As a result, the geotextile in (P') is pulled towards (P). In most cases, the overburden over the portion (P') of the geotextile is too small to generate sufficient friction to prevent movement, and the geotextile actually moves from (P') to (P). Therefore, it is reasonable to assume that elongation is uniform along the entire length of the geotextile:

$$\epsilon = \frac{b + b'}{a + a'} - 1 \quad \ldots \ldots \ldots \ldots \ldots \ldots \ldots \ldots \ldots \ldots \ldots \ldots \ldots \ldots \ldots \ldots \quad (35)$$

in which: ϵ = elongation of the geotextile; a, a' = half length of the chord subtended respectively by (P) and (P') (m); and b, b' = half length of (P) and (P'), respectively (in meters).

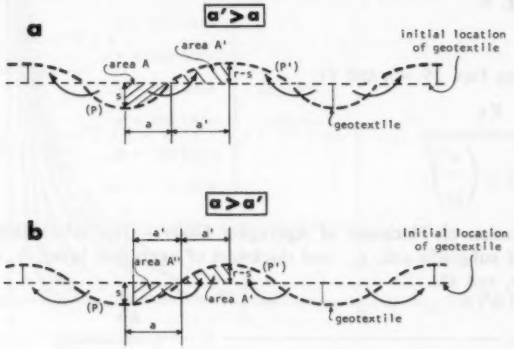

FIG. 12.—Determination of Settlement Versus Rut Depth Relationship

The elongation ϵ can be calculated using Eq. 35 and the following relationship between an arc of parabola and subtended chord:

$$\frac{b}{a} - 1 = \frac{1}{2}\left[\sqrt{1 + \left(\frac{2s}{a}\right)^2} + \frac{a}{2s}\ln\left(\frac{2s}{a} + \sqrt{1 + \left(\frac{2s}{a}\right)^2}\right) - 2\right] \quad \ldots \ldots \quad (36)$$

$$\frac{b'}{a'} - 1 = \frac{1}{2}\left[\sqrt{1 + \left(\frac{2(r-s)}{a'}\right)^2} + \frac{a'}{2(r-s)}\ln\left(\frac{2(r-s)}{a'} + \sqrt{1 + \left(\frac{2(r-s)}{a'}\right)^2}\right) - 2\right] \quad \ldots \ldots \quad (37)$$

If $a > a'$ [Fig. 12(b)], Eq. 34 leads to $(r - s)/a' > s/a$. Therefore, the elongation (consequently the tension) of the geotextile is larger in (P') than in (P). However, the geotextile does not move because the high normal stress transmitted to (P) by the wheel load generates an important friction. So, in this case, the elongation is different in (P) and in (P'). The elongation of the geotextile in (P) is given directly by Eq. 36 because:

$$\epsilon = \frac{b}{a} - 1 \quad \ldots \quad (38)$$

Determination of Reduction of Pressure p_g on Subgrade Soil.—In fact, p_g is a uniform pressure applied on AB (Fig. 11) and is equivalent to the vertical projection of the tension t of the geotextile at points A and B:

$$ap_g = t \cos \beta \quad \ldots \quad (39)$$

According to a property of parabolas:

$$\tan \beta = \frac{a}{2s} \quad \ldots \quad (40)$$

From Fig. 3:

$$t = K\epsilon \quad \ldots \quad (41)$$

Combining Eqs. 39, 40, and 41:

$$p_g = \frac{K\epsilon}{a\sqrt{1 + \left(\frac{a}{2s}\right)^2}} \quad \ldots \quad (42)$$

Determination of Thickness of Aggregate Layer.—The relationship between cohesion of subgrade soil, c_u, and thickness of aggregate layer, h, stems from Eqs. 14, 29, and 42:

$$(\pi + 2)c_u = \frac{P}{2(B + 2h \tan \alpha)(L + 2h \tan \alpha)} + \frac{K\epsilon}{a\sqrt{1 + \left(\frac{a}{2s}\right)^2}} \quad \ldots \quad (43)$$

in which: s is given by Eq. 33 and ϵ by Eqs. 35, 36, and 37 (when $a' > a$); s is given by Eq. 34 and ϵ by Eqs. 36 and 38 (when $a > a'$); L and B are given respectively by Eqs. 5 and 7 (on-highway trucks) and Eqs. 6 and 8 (off-highway trucks); and a and a' are given respectively by Eqs. 30 and 31 in all cases.

Fig. 13 presents values obtained from Eq. 43 in the case of the 80 kN standard axle load and 0.3 m rut depth. Similar charts have been established for several values of axle load P and rut depth r. Design engineers should bear in mind that the use of these charts is restricted to very light traffic (1 passage–20 passages, approx) since it has been established using a quasi-static analysis. In fact, it is better to consider these charts as a step towards the more general method presented hereafter.

Proposed Practical Method

Principle of Method.—To this point, unpaved roads without and with geotextile have been considered. For unpaved roads without geotextile, two approaches have been presented: (1) A quasi-static analysis leading to a thickness h_0 of

aggregate layer; and (2) an empirical method taking traffic into account, giving a thickness h'_0 of aggregate layer. For unpaved roads with geotextile, only a quasi-static analysis has been presented, leading to a thickness h of aggregate layer.

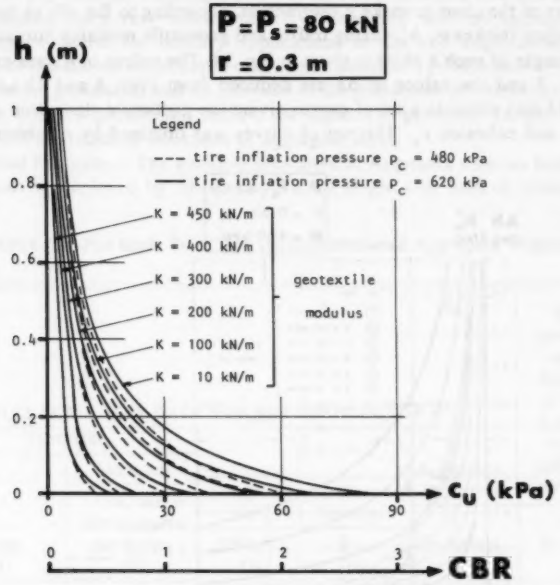

FIG. 13.—Aggregate Thickness h Versus Subgrade Soil Cohesion (Quasi-Static Analysis for Case with Geotextile)

The thickness h' of aggregate layer when traffic is taken into account remains to be determined in the case of unpaved roads with geotextile. The following procedure is proposed:

1. The reduction of aggregate thickness, Δh, resulting from the use of a geotextile, is deduced from the quasi-static analyses by:

$$\Delta h = h_0 - h \quad \ldots \quad (44)$$

2. The thickness, h', of aggregate layer in the case of a geotextile-reinforced, unpaved road when traffic is taken into account, is determined by:

$$h' = h'_0 - \Delta h \quad \ldots \quad (45)$$

This procedure assumes that the value of Δh does not depend on the traffic. Extensive full scale tests should be performed in order to verify this assumption.

Practical Charts.—The establishment of charts giving the thickness, h', as

a function of all the parameters would be too cumbersome. A way of minimizing the number of charts is to take advantage of the fact that h'_0 does not depend on the geotextile while Δh does not depend on the traffic. Therefore, two sets of curves are presented in each chart, one giving h'_0 as a function of the traffic, the other giving Δh as a function of the geotextile modulus. Then, it is up to the user of the chart to make a subtraction, according to Eq. 45, to determine the aggregate thickness, h', taking traffic and geotextile modulus into account.

An example of such a chart is given in Fig. 14. The values of h'_0 are extracted from Fig. 9 and the values of Δh are deduced from Figs. 8 and 13 using Eq. 44. Fig. 14 also presents a set of curves giving the geotextile elongation ϵ versus subgrade soil cohesion c_u. This set of curves was obtained by combining Eqs.

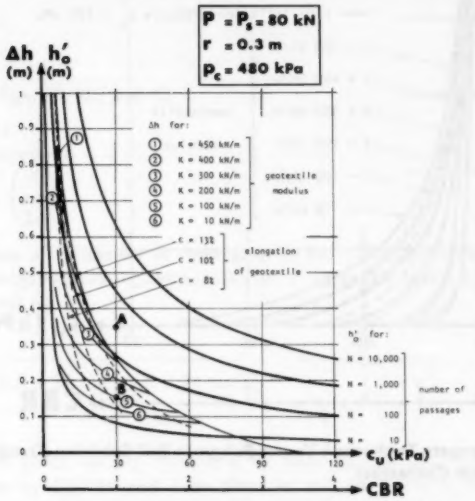

FIG. 14.—Aggregate Thickness h'_0 (Case without Geotextile when Traffic is Taken into Account) and Possible Reduction of Aggregate Thickness Δh Resulting from use of Geotextile Versus Subgrade Soil Cohesion (Chart Related to On-Highway Truck with Standard Axle Load)

30–38 and Eq. 22 (for on-highway trucks) or Eq. 23 (for off-highway trucks). It allows the user of the chart to check that, in the considered case, the geotextile is not subjected to excessive elongation.

Two features of the chart are noteworthy: (1) according to Eq. 44, Δh can never be higher than h_0, this is the reason why all the Δh versus c_u curves end at the h_0 versus c_u extracted from Fig. 8; and (2) no aggregate is needed on top of the geotextile when the Δh versus c_u curve is above the h'_0 versus c_u curve.

Analysis of Results.—Fig. 14 is only one among the charts developed for various axle loads and rut depths. Considering the whole set of charts leads to the following comments: (1) In the considered range of tire inflation pressures,

the tire inflation pressure has no influence on h'_0 and almost none on Δh; (2) for typical geotextiles, the reduction of aggregate thickness resulting from the use of a geotextile generally ranges between 20% and 60% for a subgrade soil CBR of one and a number of passages between 1,000 and 10,000; however, the use of a geotextile with high modulus makes it possible to build an access road designed for a very small number of passages, with no aggregate at all (this may be useful for military applications or for soil exploration); (3) an increase of the allowable rut depth causes a decrease of h'_0 (thickness of aggregate layer without geotextile) and an increase of Δh (reduction of thickness resulting from the use of a geotextile); and (4) the higher the geotextile tensile modulus, the thinner the required thickness of aggregate layer.

Practical Example.—The example presented in Appendix I shows how a given traffic can be replaced by 340 passages of a single axle load of about 80 kN.

TABLE 1.—Full Scale Test Data Versus Calculated Aggregate Thickness

FULL SCALE TEST DATA (FOR RUT DEPTH OF 0.28 m)					Aggregate Thickness (for Rut Depth of 0.30 m) Calculated from K, CBR, and N, using Fig. 14
Geotextile		Subgrade Soil	Number of Passages	Aggregate Thickness	
Type (1)	Modulus K, in kilonewtons per meter (2)	CBR (–) (3)	N(–) (4)	h', in meters (5)	h', in meters (6)
Without geotextile	0	0.9	200	0.36	0.34
Bidim U44/C38	70	1.1	2,500	0.36	0.38
Reeves T16	200	1.0	37,000	0.36	0.5–0.6[a]

[a]Extrapolated values because number of passages is larger than 10,000.

What is the required thickness of aggregate layer, if the CBR of the subgrade soil is one, the modulus of the geotextile is 90 kN/m and the allowable rut depth is 0.3 m?

In Fig. 14, related to an 80 kN axle load and a 0.3 m rut depth: (1) Point A, corresponding to CBR = 1 and N = 340, shows that the required thickness of aggregate layer when there is no geotextile would be 0.35 m; and (2) point B, corresponding to CBR = 1 and K = 90 kN/m, shows that the reduction of thickness can be 0.15 m. Consequently, the recommended thickness of aggregate is 0.20 m.

Also, point B in Fig. 14 shows that the elongation of the geotextile is approx 10%. It should be checked that the elongation at failure of the geotextile is larger than this value.

Comparison with Full Scale Tests.—The United States Army Corps of Engineers

has conducted full scale tests on unpaved roads with and without geotextile (3,4). The results of these tests were expressed as a number of passages of an equivalent standard axle (P_s = 80 kN). So, a comparison is easy with the theoretical results presented in Fig. 14. Test results corresponding to a rut depth of 0.28 m are given in Table 1. Also tabulated is the aggregate thickness calculated from test data using Fig. 14.

Comparison of calculated and actual thicknesses shows a good agreement when traffic is light. The theoretical results appear conservative when traffic is heavy. This confirms that the use of Fig. 14 and similar charts is not recommended for numbers of passages larger than 10,000.

Conclusions

Summary of Main Features of this Study.—The development of a method for the design of geotextile-reinforced, unpaved roads involves three steps:

1. An empirical formula deduced from full scale test results is related to unpaved roads without geotextile; it gives the thickness of aggregate layer as a function of traffic and soil properties.
2. A theoretical analysis compares unpaved roads with and without geotextile; it determines the reduction of aggregate thickness resulting from the use of a geotextile; this theoretical analysis does not take traffic into account.
3. By combining the empirical formula and the theoretical analysis, charts are established; these charts allow the determination of aggregate thickness for an unpaved road with geotextile, when traffic is taken into account.

The method presented in this paper is devoted to the reinforcement role of geotextiles and therefore, does not consider other beneficial effects of geotextiles, such as separation, filtration, and drainage.

Validity of Assumptions.—Many assumptions were made in this study. All are precisely defined in the text. However, a short review is necessary to remind the potential users of the charts of their limitations:

1. Assumptions related to bearing capacity calculations are classical in soil mechanics (bidimensional calculations, use of the theories of elasticity and plasticity); therefore, from the viewpoint of bearing capacity, there are no more limitations than, say, in classical methods for foundation design.
2. Assumptions related to the role of the geotextile are based upon limited experimental evidence; these assumptions may be improved in the future; but all assumptions, made in this study, concerning the mechanical roles of soil and geotextile are consistent with each other.
3. Assumptions related to traffic are the most imprecise; the fact that Eq. 25 (established for paved roads) is used for unpaved roads can be questioned, but, at present, there is no similar equation for unpaved roads; to be safe, it is recommended not to use Fig. 14 and similar charts for numbers of passages larger than 10,000.

Practical Consequences of the Results.—The present charts are intended to assist engineers in designing geotextile-reinforced, unpaved roads and in particu-

lar, in evaluating the reduction of aggregate thickness resulting from the use of a geotextile. This reduction appears to be on the order of magnitude of 20%–60% in some typical cases considered in this paper. Such a significant reduction can have important economic consequences, that justify the use of the charts.

These charts, related to frictionless subgrade soils, have already proved to be useful in several projects. It is hoped that further research will lead to similar charts for other types of subgrade soils.

Acknowledgments

The research work presented in this paper is a part of the program of development of the Geotextiles and Geomembranes Group of Woodward-Clyde Consultants, conducted under the responsibility of Yves Lacroix. The writers are indebted to H. Nicot for numerical calculations and J-Y. Perez and R. J. Woodward III for valuable comments.

Appendix I.—Equivalent Single Axle

A traffic is defined by the load, P_i, and the number of passages, N_i, of each axle. In order to use the charts presented in this paper, a traffic must be expressed in the simplest manner which consists of the number of passages, N_{eq}, of an equivalent single axle load, P_{eq}. This can be achieved by using Eq. 25 and assuming that all axles have the same width and are driven in the same ruts (in other words, the trucks are assumed not to wander over the road).

General Case.—There are many possibilities to define the equivalent single axle corresponding to a given traffic. Two of these possibilities seem the most adequate.

A first possibility is to consider that the load of the equivalent axle is equal to the largest P_i:

$$P_{eq} = (P_i)_{max} \quad \ldots \quad (46)$$

Hence, from Eq. 25:

$$N_{eq} = \sum N_i \left[\frac{P_i}{(P_i)_{max}} \right]^{3.95} \quad \ldots \quad (47)$$

A second possibility is to consider that the number of passages of the equivalent single axle is equal to the largest N_i:

$$N'_{eq} = (N_i)_{max} \quad \ldots \quad (48)$$

Thus, from Eq. 25:

$$(P'_{eq})^{3.95} = \sum P_i^{3.95} \left[\frac{N_i}{(N_i)_{max}} \right] \quad \ldots \quad (49)$$

These two approaches are logical because damage to the road can be caused either by excessive loading or by excessive number of passages.

Then, charts are used with both (P_{eq}, N_{eq}) and (P'_{eq}, N'_{eq}) and the more conservative result is selected as the design thickness of aggregate layer.

Case of Identical Trucks with Rear Single Axle.—Consider N_0 passages of identical trucks with a rear single axle. Because the rear axle load is larger than the front axle load, Eqs. 47 and 49 become:

$$N_{eq} = N_0 \left[1 + \left(\frac{P_f}{P_r} \right)^{3.95} \right] \quad \ldots \quad (50)$$

$$P'_{eq} = P_r \left[1 + \left(\frac{P_f}{P_r} \right)^{3.95} \right]^{1/3.95} \quad \ldots \quad (51)$$

in which: P_f = front axle load (N); and P_r = rear axle load (N). Usually, P_r is at least two times larger than P_f. Consequently:

$$N_{eq} \simeq N'_{eq} = N_0 \quad \ldots \quad (52)$$

$$P'_{eq} \simeq P_{eq} = P_r \quad \ldots \quad (53)$$

So, practically only the rear axle needs to be considered when the traffic is made up of identical trucks with rear single axle.

Case of Identical Trucks with Rear Tandem Axle.—According to the previous comment, the front axle load, smaller than the rear axle load, can be neglected. Therefore, only the two axles of the tandem need to be considered. Each of these two axles passing N_0 times on the road:

$$N_{eq} = 2\,N_0 \quad \ldots \quad (54)$$

The equivalent single axle load should be $Q/2$ (in which Q = tandem axle load). However, it is recommended to take:

$$P_{eq} = 0.6\,Q \quad \ldots \quad (55)$$

This increase of 20% of the actual equivalent single axle load is intended to take into account the additional stresses induced in the subgrade soil because of the interaction between the two axles of the tandem.

Example of Determination of Equivalent Single Axle.—Consider 70 passages of trucks with a rear tandem axle load of 160,000 N and 340 passages of trucks with a rear single axle load of 50,000 N. What is the equivalent single axle to be used in the design of the road?

First, according to Eqs. 54 and 55, the tandem axle is equivalent to a single axle defined by:

$$N_{eq\ tandem} = 2\,N_0 = 140; \quad P_{eq\ tandem} = 0.6 \times 160{,}000 = 96{,}000\ N \quad \ldots \quad (56)$$

Then, there are two alternatives to determine the single axle equivalent to the total traffic. The first alternative is, according to Eqs. 46 and 47:

$$P_{eq} = 96{,}000\ N; \quad N_{eq} = 140 + 340 \left(\frac{50{,}000}{96{,}000} \right)^{3.95} = 166 \quad \ldots \quad (57)$$

The second alternative is, according to Eqs. 48 and 49:

$$N'_{eq} = 340; \quad P'_{eq} = \left[(96{,}000)^{3.95} \left(\frac{140}{340} \right) + (50{,}000)^{3.95} \right]^{1/3.95}$$

$$= 80{,}047\,N \quad \ldots \quad (58)$$

Then, the aggregate thickness is calculated using the charts for: (1) 166 passages of a single axle of 96,000 N; and (2) 340 passages of a single axle of 80,047 N. The more conservative result must be selected.

Appendix II.—References

1. Hammit, G., "Thickness Requirements for Unsurfaced Roads and Airfield Bare Base Support," *Technical Report S-70-5*, United States Army Engineer Waterways Experiment Station, Vicksburg, Miss., July, 1970.
2. Kinney, T. C., "Fabrics Induced Changes in High Deformation Soil-Fabric-Aggregate Systems," thesis presented to the University of Illinois, at Urbana, Illinois, in 1979, in partial fulfillment of the requirements for the degree of Doctor of Philosophy.
3. Webster, S. L., and Alford, S. J., "Investigation of Construction Concepts for Pavements Across Soft Ground," *Technical Report S-78-6*, United States Army Engineer Waterways Experiment Station, Vicksburg, Miss., July, 1978.
4. Webster, S. L., and Watkins, J. E., "Investigation of Construction Techniques for Tactical Bridge Approach Roads Across Soft Ground," Technical Report S-77-1, United States Army Engineer Waterways Experiment Station, Vicksburg, Miss., Feb., 1977.
5. Whitman, R. V., and Hoeg, K., "Development of Plastic Zone Beneath a Footing," Report By M.I.T. Department of Civil Engineering, United States Army Engineer Waterways Experiment Station, 1966.

Appendix III.—Notation

The following symbols are used in this paper:

A = area shown in Fig. 12, in square meters;
A' = area shown in Fig. 12, in square meters;
A'' = area shown in Fig. 12, in square meters;
A_c = contact area of tire, in square meters;
a = half length of chord subtended by portion of parabola (P), as shown on Fig. 11, in meters;
a' = half length of chord subtended by portion of parabola (P'), as shown on Fig. 11, in meters;
B = width of equivalent contact area, in meters;
b = half length of portion of parabola (P), in meters;
b' = half length of portion of parabola (P'), in meters;
CBR = California Bearing Ratio (dimensionless);
c_u = undrained cohesion of subgrade soil (in pascals or kilopascals);
e = distance between midpoints of two sets of wheels, in meters;
H = thickness of subgrade soil, in meters;
H_{min} = minimum value of H to ensure validity of analysis, in meters;
H_p = depth of plastic zone, in meters;
h = aggregate thickness (quasi-static analysis in case with geotextile), in meters;
h' = aggregate thickness (case with geotextile, when traffic is taken into account), in meters;
h_0 = aggregate thickness (quasi-static analysis in case without geotextile), in meters;

h_0' = aggregate thickness (case without geotextile, when traffic is taken into account), in meters;
Δh = reduction of aggregate thickness from use of geotextile, in meters;
K = secant modulus of geotextile (in Newtons per meter and kilonewton per meter);
N = number of passages of axle load P;
N_{eq}, N'_{eq} = equivalent number of passages (Appendix I);
N_s = number of passages of standard axle load P_s;
P = axle load (in Newtons and kilonewtons);
P_{eq}, P'_{eq} = equivalent single axle load (Appendix I), in pascals or kilopascals;
P_f = front axle load (in Newtons and kilonewtons);
P_r = rear single axle load (in Newtons and kilonewtons);
P_s = standard axle load (in Newtons and kilonewtons);
p = pressure at base of aggregate layer in case with geotextile in pascals or kilopascals;
p_0 = pressure at base of aggregate layer in case without geotextile in pascals or kilopascals;
p^* = pressure applied on subgrade soil by portion AB of geotextile in pascals or kilopascals;
p_c = tire inflation pressure in pascals or kilopascals;
p_{ec} = equivalent contact pressure in pascals or kilopascals;
p_g = reduction of pressure resulting from use of geotextile in pascals or kilopascals;
Q = tandem axle load (in Newtons and kilonewtons);
q_c = cone resistance in pascals or kilopascals;
q_e = elastic bearing capacity of soil in pascals or kilopascals;
q_{lat} = lateral surcharge in pascals or kilopascals;
q_{ult} = ultimate bearing capacity of soil in pascals or kilopascals;
r = rut depth, in meters;
s = settlement under wheels, in meters;
t = tension on portion AB of geotextile, as shown on Fig. 11 (in Newtons per meter or kilonewtons per meter);
α = angle of load distribution pyramide in case with geotextile, in degrees;
α_0 = angle of load distribution pyramide in case without geotextile, in degrees;
β = angle between tension and vertical line, as shown on Fig. 11, in degrees;
γ = weight per unit volume of aggregate (in Newtons per cubic meters or kilonewtons per cubic meters);
ϵ = elongation of geotextile in parabola (P) (dimensionless, as a percentage); and
ϵ_F = elongation of geotextile at failure (dimensionless, as a percentage).

(Note: in this paper, elongation is synonymous of strain)

Technical Papers

Original papers should be submitted in triplicate to the Manager of Technical and Professional Publications, ASCE, 345 East 47th Street, New York, N.Y. 10017. Authors must indicate the Technical Division or Council, Technical Committee, Subcommittee, and Task Committee (if any) to which the paper should be referred. Those who are planning to submit material will expedite the review and publication procedures by complying with the following basic requirements:

1. Titles must have a length not exceeding 50 characters and spaces.

2. The manuscript (an original ribbon copy and two duplicate copies) should be double-spaced on one side of 8-1/2-in. (220-mm) by 11-in. (280-mm) paper. Three copies of all figures and tables must be included.

3. Generally, the maximum length of a paper is 10,000 word-equivalents. As an *approximation*, each full manuscript page of text, tables or figures is the equivalent of 300 words. If a particular subject cannot be adequately presented within the 10,000-word limit, the paper should be accompanied by a rationale for the overlength. This will permit rapid review and approval by the Division or Council Publications and Executive Committees and the Society's Committee on Publications. Valuable contributions to the Society's publications are not intended to be discouraged by this procedure.

4. The author's full name, Society membership grade, and a footnote stating present employment must appear on the first page of the paper. Authors need not be Society members.

5. All mathematics must be typewritten and special symbols must be identified properly. The letter symbols used should be defined where they first appear, in figures, tables, or text, and arranged alphabetically in an appendix at the end of the paper titled Appendix.—Notation.

6. Standard definitions and symbols should be used. Reference should be made to the lists published by the American National Standards Institute and to the *Authors' Guide to the Publications of ASCE*.

7. Figures should be drawn in black ink, at a size that, with a 50% reduction, would have a published width in the *Journals* of from 3 in. (76 mm) to 4-1/2 in. (110 mm). The lettering must be legible at the reduced size. Photographs should be submitted as glossy prints. Explanations and descriptions must be placed in text rather than within the figure.

8. Tables should be typed (an original ribbon copy and two duplicates) on one side of 8-1/2-in. (220-mm) by 11-in. (280-mm) paper. An explanation of each table must appear in the text.

9. References cited in text should be arranged in alphabetical order in an appendix at the end of the paper, or preceding the Appendix.—Notation, as an Appendix.—References.

10. A list of key words and an information retrieval abstract of 175 words should be provided with each paper.

11. A summary of approximately 40 words must accompany the paper.

12. A set of conclusions must end the paper.

13. Dual units, i.e., U.S. Customary followed by SI (International System) units in parentheses, should be used throughout the paper.

14. A practical applications section should be included also, if appropriate.